15. SITE 850[1]

Shipboard Scientific Party[2]

HOLE 850A

Date occupied: 12 June 1991

Date departed: 13 June 1991

Time on hole: 14 hr, 56 min

Position: 1°17.837′N, 110°31.283′W

Bottom felt (rig floor; m, drill-pipe measurement): 3797.8

Distance between rig floor and sea level (m): 11.7

Water depth (drill-pipe measurement from sea level, m): 3786.1

Total depth (rig floor; m): 3872.0

Penetration (m): 74.2

Number of cores (including cores with no recovery): 8

Total length of cored section (m): 74.2

Total core recovered (m): 77.12

Core recovery (%): 103.9

Oldest sediment cored:
Depth (mbsf): 74.2
Nature: diatom foraminifer nannofossil ooze
Earliest age: early Pliocene

HOLE 850B

Date occupied: 13 June 1991

Date departed: 16 June 1991

Time on hole: 2 days, 17 hr, 16 min

Position: 1°17.827′N, 110°31.286′W

Bottom felt (rig floor; m, drill-pipe measurement): 3797.8

Distance between rig floor and sea level (m): 11.7

Water depth (drill-pipe measurement from sea level, m): 3786.1

Total depth (rig floor; m): 4197.6

Penetration (m): 399.8

Number of cores (including cores with no recovery): 42

Total length of cored section (m): 396.8

Total core recovered (m): 393.58

Core recovery (%): 99.2

Oldest sediment cored:
Depth (mbsf): 399.8
Nature: radiolarian diatom nannofossil ooze
Earliest age: middle Miocene

Principal results: The combination of good fortune and the combined skills of the SEDCO and ODP crews placed us in the enviable position of being able to consider drilling an additional site beyond those outlined in our original scientific program. After careful consideration we selected Site 850 at 1°17′N to increase the spatial resolution along our western (110°W) transect. Oceanographic and biologic studies in this region have shown that the equatorial divergence zone exhibits very strong and narrow (±1° of latitude) gradients, especially in surface production. We were prompted to attempt such a study because of the great success we had in making intersite correlations with near-continuous data sets (such as the GRAPE sediment density record) and our belief that these records will provide a means of establishing a correlatable, extremely high-resolution stratigraphic framework.

The selection of Site 850 was based on seismic data collected during the site-survey cruise, Venture 1, of the *Thomas Washington*. Because of limited time, only two holes were drilled. Hole 850A was APC-cored to a depth of 74 mbsf. Hole 850B was APC-cored to 98 mbsf when excessive pullout required our switching to the XCB-coring system. The hole was then continued to basement at a total depth of 399.8 mbsf. While double APC-coring, in conjunction with real-time monitoring of GRAPE density, susceptibility, and color reflectance profiles, has assured complete coverage of the upper 75 m, our experience has shown us that a section that contains only one APC and XCB core will inevitably have gaps. We hoped to determine the extent of these gaps by correlating the continuous GRAPE record to nearby sites.

The sedimentary section at Site 850 spans the upper middle Miocene to the Pleistocene and can be represented as a single lithologic unit of nannofossil ooze with varying proportions of other microfossil constituents. The uppermost 76 m (0–3.4 Ma) is richer in foraminifers and radiolarians than the average for the rest of the section. Between 76 and 255 mbsf (3.4–6.8 Ma), the section is dominated by diatom nannofossil ooze with interbeds of nannofossil diatom ooze and between 255 and 395 mbsf (6.8–10.5 Ma), the sediments are radiolarian and diatom nannofossil oozes. In this lower interval can be seen several distinctive layers of laminated nannofossil diatom ooze and very thinly bedded chert. The 5 m above basement (10.6 Ma) is iron-oxide-rich metalliferous sediment.

Based on results at other near-equatorial sites, we expected little paleomagnetic signal in the sediments of Site 850. We were pleasantly surprised when an interval from 55 to 69 mbsf (2.9–3.4 Ma) showed a strong and coherent pattern with five reversals that spanned the Kaena subchron to the Gauss/Gilbert boundary. The origin of this strong magnetic signal in this interval at present is still not understood. The interval exhibits neither anomalous sedimentation rates, nor a change in redox conditions. Whatever its cause, the presence of an equatorial high sedimentation rate interval having good magnetostratigraphy is unique and an important addition to the stratigraphic framework being developed for the Leg 138 sites.

Biostratigraphic age control was provided by all four of the chief groups of planktonic microfossils, although their abundances and state of preservation differ. Preservation of the calcareous nannofossils, radiolarians, and diatoms is generally moderate to good, with the exception of the lowermost 10 m (10.6 Ma), which has no diatoms. Preservation of foraminifers is moderate down to about 65 mbsf (3 Ma) and poor through the rest of the sequence.

Sedimentation rates at Site 850 exhibit a pattern similar to those at Site 849, with the highest rates found in the late Miocene and early Pliocene. However, important differences reflect the steep gradients within the equatorial region. Rates are lower during the Pliocene and Pleistocene in Site 850, compared with Site 849. Based on backtracked paths of these sites, the gradient in sedimentation rates switched only during the brief period when Site 850 passed under the equatorial divergence zone. Thus,

[1] Mayer, L., Pisias, N., Janecek, T., et al., 1992. *Proc. ODP, Init. Repts.*, 138: College Station, TX (Ocean Drilling Program).
[2] Shipboard Scientific Party is as given in the list of participants preceding the contents.

even over long time scales, the gradients observed in surface ocean processes of the equatorial Pacific Ocean are recorded in the sediment record.

Because of the thickness of the section and our lack of time for collecting complete double APC and XCB cored sections, a high priority was placed on logging this site. Three logging runs were completed that included the geophysical and geochemical strings as well as the formation microscanner (FMS). The logs are of excellent quality and can be matched to continuous laboratory measurements, such as the GRAPE; initial correlations suggest that the logs can be used to help determine the extent of coring gaps in the single XCB-cored section. The FMS clearly delineated the three thin chert layers (at about 350 mbsf, 9.9 Ma) recovered (a credit to both the FMS and the XCB) and indicated a fourth that was not recovered in place.

As at the nearby Site 849, the presence of the chert layers appears to divide the section into two distinct zones with respect to interstitial water chemistry. Above the cherts microbial degradation of organic matter consumes sulfate, generating concave-downward and concave-upward profiles of sulfate and alkalinity, respectively. Below the chert both sulfate and alkalinity return to seawater values. Ammonia decreases 22-fold across this boundary while potassium is invariant. Magnesium and calcium decrease downhole and silica increases with depth, consistent with reaction with biogenic silica.

Site 850 was a gift given to us by the fair-weather gods and the competence and hard work of the SEDCO and ODP crews. We chose to push our high-resolution capabilities to the limit at this extra site, and the wildcat well hit paleoceanographic pay-dirt. From our shipboard analyses it is already clear that we can delineate the effects of the narrow equatorial productivity gradient. As our high-resolution studies continue we hope to trace the behavior of this feature back through the late Neogene and produce a detailed record of the response of equatorial upwelling to climatic forcing. At the conclusion of Site 850, Leg 138 completed 8.81 log(m^2kt).

BACKGROUND AND SCIENTIFIC OBJECTIVES

The combination of good fortune and the skill of the SEDCO crew put us in the enviable position of having time in excess of that required to complete our basic scientific program. After careful consideration of a number of alternatives, Site 850 was chosen as an additional site. The selection of the Site 850 was based on our ability at previous sites, particularly Sites 846 and 847, to collect very high quality GRAPE density, color reflectance, and magnetic susceptibility data that demonstrated that a high-resolution chronostratigraphic framework could be established for sites drilled in the equatorial Pacific (Fig. 1). Given this ability to produce high-resolution stratigraphies, it became possible to examine an additional element of the equatorial Pacific circulation system.

Physical and biological oceanographic studies of the equatorial Pacific divergence zone have demonstrated that this region exhibits very strong gradients, especially in surface production, within a very narrow zone (±1° of latitude) across the equator (Chavez and Barber, 1987; JGOFS, 1991). This strong gradient in surface productivity is also reflected in the sedimentation rates across the equator as measured in closely spaced standard piston cores taken along transects at 133°W (Isern, 1991) and during the site-survey cruise for Leg 138 (see "Site Survey" chapter, this volume). In addition, the backtracked path of this site (Fig. 2) suggests that Site 850 crossed the Equator at a time that is not represented in any of the other Leg 138 drill sites.

Site 850 was selected midway between Sites 849 and 851 to provide a very high spatial (as well as temporal) resolution of this steep equatorial divergence gradient. Like other sites along the 110°W transect, the site was formed at the East Pacific Rise and the backtrack path is constrained by the Pacific plate pole rotation (Fig. 2). The location of the site is about 9 km north of a seamount at approximately 1°12.5′N (Fig. 3) and in a sediment sequence beyond the influence of this topographic feature (Fig. 4). The sediment section here is significantly thickened as compared to Sites 849 and 851; the total sediment section is the order of 400 m thick.

OPERATIONS

Transit to Site 850

The transit from Site 849 to Site 850 traversed 54 nmi at an average speed of 12.6 kt. Upon reaching the general area of the new site, the vessel slowed to 6 kt, and seismic equipment was deployed. The vessel began the site survey at 2100L (All times are local time, L, or Universal Time Coordinated, UTC minus 7 hr. All times in Table 1 are UTC.) 12 June and by 2248L, a beacon had been deployed. The survey continued for 10 min past the site. The ship then returned to the site, and hydrophones and thrusters were lowered by 2330L 12 June. The depth to the seafloor, based upon the precision depth recorder (PDR), was 3803.4 mbrf.

Hole 850A

Core 138-850A-1H was taken at a depth of 3796 mbrf at 0640L 13 June, and 7.68 m of sediment was recovered, establishing the mud line at 3803.0 mbrf. Piston coring advanced to 74.0 mbsf (Core 138-850A-8H; see Table 1) with multishot orientation beginning with the fourth core. After Core 138-850A-8H had been recovered, the time allotted for this hole expired. The pipe was then pulled out of the hole, and the bit cleared the mud line at 1344L 13 June, terminating drilling at Hole 850A. Core recovery for this hole was 103.9%.

Hole 850B

The vessel was offset 20 m south from Hole 850A. The bit was washed down 3 mbsf and Cores 138-850B-1H through -10H were taken over the interval from 3.0 to 98.0 mbsf, with orientation beginning with the fourth core. An overpull of 75,000 lb was needed to pull Core 138-850B-10H free, which forced the termination of the APC-coring program at this point. Recovery in the APC-cored section of the hole was 104.9%.

Coring resumed with the XCB-coring system at Core 138-850B-11X and continued to a depth of 399.8 mbsf (Core 42X), where basement was reached. As the depth objective for the hole had been reached, the coring program was terminated and preparations for logging began. Recovery in the XCB-cored section was 97.4%.

Logging of Hole 850B

In preparation for logging, mud was pumped into the hole, and the pipe was pulled to 65.3 mbsf. All three standard ODP tool strings were run and had only a few operational problems (Table 2). The heave compensator did not function properly; thus, logging was conducted without it. However, wave swells remained below 2 to 3 feet.

Hole 850B was logged first with the geophysical tool string. To save time and to fit FMS logging into our limited schedule, the downgoing log and repeat section were not run. The main logging run was from 400.2 to 79.2 mbsf. The LDGO temperature tool failed during this logging pass because of a short circuit in the tool that had drained the battery.

Next, the hole was logged with the geochemical tool string from 399.3 mbsf to the mud line. To minimize activation of the borehole, the GST calibration procedure was changed. The tool string was lowered to total depth (400.2 mbsf), and several meters of extra cable were lowered out. The GST then was calibrated as the slack was pulled out of the cable. The calibration was finished before the tool had been moved more than 1 m in the borehole. There should be no spikes in the record from hole activation during calibration, although one section of bad GST data does occur between 255 and 262 mbsf, where the high voltage to the tool was unstable.

The first FMS pass was run from total depth (399.9 mbsf) to 304.8 mbsf. The tool string then was lowered back down to total depth; the main logging pass covered the interval from 399.9 to 88.4 mbsf. The log was stopped at 88.4 mbsf because the hole had washed

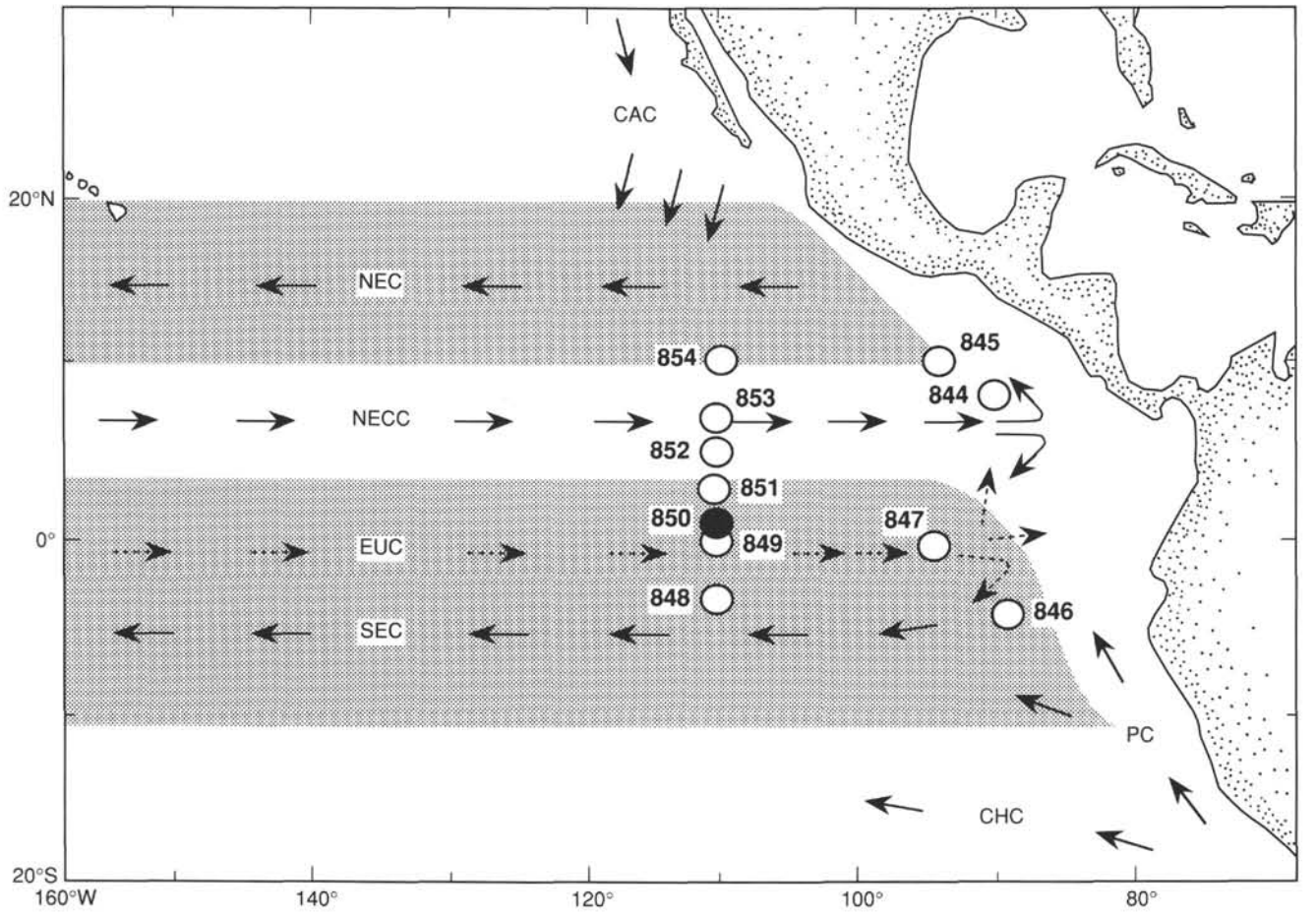

Figure 1. Location of Site 850 and generalized circulation system of the eastern equatorial Pacific Ocean. Other Leg 138 sites are shown for reference. Surface current shown as solid arrows, subsurface current as dashed arrows; CAC = California Current; NEC = North Equatorial Current; NECC = North Equatorial Countercurrent; EUC = Equatorial Undercurrent; SEC = South Equatorial Current; PC = Peru Current; and CHC = Chile Current. Shaded area illustrates general latitudinal extent of the SEC and NEC.

out above this depth. A problem occurred when getting the top of the tool string and then the base of the tool string into the pipe because the FMS caliper did not fully close at the end of the run. Eventually, the tool was worked back into the pipe, however, with minor damage to one of the FMS pad assemblies.

At the conclusion of the logging program, the drill string was pulled out of the hole. The bit cleared the mud line at 1304L 16 June, which ended drilling at Hole 850B. The rig floor was quickly secured, the thrusters and hydrophones retracted, and the ship was under way toward Site 851 by 0700L 16 June.

LITHOSTRATIGRAPHY

Introduction

A 399.8 m sedimentary sequence of middle Miocene to Pleistocene nannofossil ooze with minor amounts of diatom ooze was recovered at Site 850 (Fig. 5). Two holes, one cored with the APC to 74.2 mbsf and one cored with the APC and XCB to 399.8 mbsf, provided continuous recovery of the upper 79.8 m (Fig. 6) and nearly continuous recovery of the remaining sedimentary column (see "Sedimentation Rates" section, this chapter). The sedimentary sequence terminates at hard rock inferred to be basalt basement at 399.8 mbsf in Hole 850B.

Lithostratigraphy of the sediments at Site 850 was based on visual core descriptions and smear slide estimates of sediment composition, as well as continuous measurements of parameters dependent upon lithology (GRAPE density, magnetic susceptibility, color reflectance spectroscopy; Fig. 6). We also considered the results of physical and chemical logs, physical properties data, sediment chemistry, and smear slide analyses (Fig. 7).

Description of Units

Lithologic Unit I

Intervals:
Cores 138-850A-1H through -8H
Cores 138-850B-1H through -10H and -11X through -42X
Age: Pleistocene to middle Miocene
Depth: 0.0–74.2 mbsf, Hole 850A; 0.0–399.8 mbsf, Hole 850B

The upper 76 m of sediment consist of (1) Pleistocene to lower Pliocene diatom nannofossil ooze, (2) foraminifer nannofossil ooze, and (3) radiolarian nannofossil ooze. Although diatom nannofossil ooze is more common than the other two lithologies, this interval contains significantly more foraminifers (10%–25%) and radiolarians (7%–20%) than sediments deeper in the section (Fig. 7).

Below the brown/green color transition at 80 cm (marking the boundary between oxidizing and reducing conditions in the sediments), the sediments are very pale gray to very pale yellowish-gray (N8 to 5Y 6/3) and have moderate reflectance (45%–70%; Fig. 8). Content of both foraminifers and diatoms is about 15%, while radiolarian content is 10% to 20%. Below the brown/green color transition,

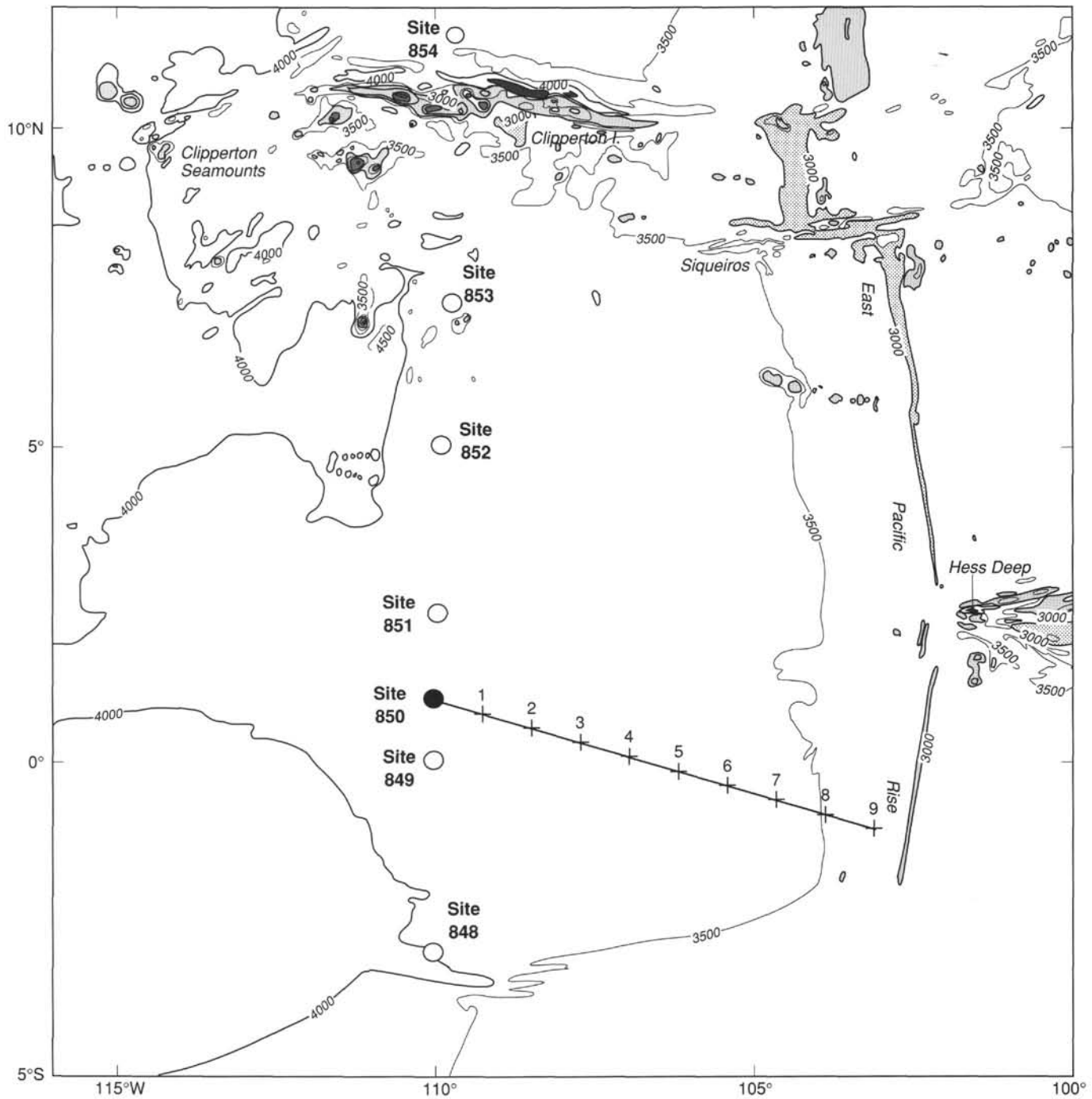

Figure 2. Generalized bathymetric map (in meters) showing location of Site 850 and other Leg 138 sites drilled along the 110°W transect (from Mammerickx, 1989). Backtrack path shows location of Site 850 at 1-m.y. intervals for the last 9 m.y.

the sediment contains thin dark gray bands of pyrite-rich sediment. A zone of nodular pyritized burrows occurs in Cores 138-850A-3H and -4H, and 2138-850B-3H (17.2–36.7 mbsf).

The interval between 76 and 86 mbsf is a transition from foraminifer and radiolarian-rich sediments (above) to diatom nannofossil ooze (below). Abundances of foraminifers and radiolarians decrease abruptly at 76 mbsf. Below this, the sediments are much lighter in color (pale gray to pale yellowish-gray, N8 to 5Y 8/1) and have substantially higher reflectance (60%–80%). The average density of the sediments increases below 76 mbsf, but remains variable (Fig. 6). Average content of calcium carbonate is also higher (see "Organic Geochemistry" section, this chapter).

The interval from 85 to 288 mbsf is dominated by diatom nannofossil ooze (lower Pliocene to upper Miocene) that contains many interbeds of nannofossil diatom ooze and a few beds of nearly pure diatom ooze. From 76 to 97.5 mbsf, nannofossils predominate (60%–80%) over diatoms (20%–40%), and a few intervals contain up to 15% foraminifers. The first interbed of nannofossil diatom ooze occurs as a minor lithology in Core 138-850B-10H-1 (0–7 cm; 88.5 mbsf). The light olive gray (5Y 6/2) diatom-rich beds in Section

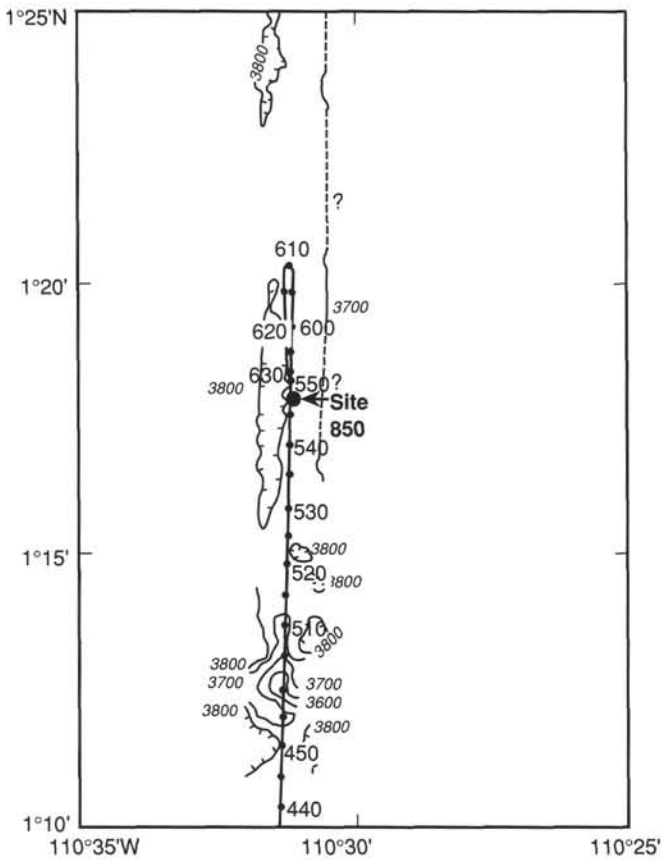

Figure 3. Hand-contoured map from *JOIDES Resolution* survey of Site 850 and from single SeaBeam profile collected on board the *Thomas Washington* during the Venture 1 cruise, September 1989. Bathymetry in meters.

138-850B-10H-7 contain thin (1–2 cm) banding and submillimeter laminations or partings. The compositional color banding in this interval (Fig. 9) suggests that bioturbation was minimal. Below this level, nannofossil diatom ooze appears scattered as thin (10–50 cm) interbeds that may be laminated in Cores 138-850B-12X through -17X, -19X, and -20X.

Nannofossil diatom ooze is the major lithology between Sections 138-850B-20X-6 and -22X-3 (191.5–212.8 mbsf), but this lithology is interbedded with diatom nannofossil ooze. In this depth interval, diatoms (especially *Thallassiothrix longissima*) represent up to 80% of the sediment in some samples. These diatom-rich beds are generally light olive gray, but in some cases, are very pale gray (N7). These diatom-rich sediments have low reflectance (about 50%; Fig. 8) and the lowest density values at the site (Fig. 6). The nannofossil content of sediments from Cores 138-850B-21X and -22X (199–211 mbsf) is low (15%–40%); one sample contained 20% clay. A small piece of chert was recovered in Core 138-850B-22X-6 (105–107 cm; 211.86 mbsf).

In Cores 138-850B-23X through -27X (213–255 mbsf), diatom nannofossil ooze (70%–90% nannofossils, 5%–30% diatoms) again dominates. This sediment is very pale gray (N8) with color reflectance values ranging from 60% to 100% (Fig. 8). Nannofossil diatom ooze appears only as scattered thin interbeds in these cores.

From 255 to 288 mbsf (Cores 850B-27X to -30X) the lithology varies from light gray (N7) to light yellowish-gray (5Y 7/1 to 8/1) diatom nannofossil ooze. Through this interval, the concentration of radiolarians increases although diatoms are still the primary microfossil group that dilutes the nannofossils. The density and reflectance of the sediments are high, but variable.

The middle Miocene sediments between 288 and 397 mbsf have relatively high concentrations of radiolarians and alternate between radiolarian nannofossil ooze and diatom nannofossil ooze. Radiolarians average 10% of the sediment, but may make up to 40% of the total sediments (Fig. 7). Darker bands, ranging from bluish-gray (5B 6/1) to greenish-gray (5BG 6/1), are richer in radiolarians. Within the nannofossil ooze, more diatom-rich sediments occur as burrow fill. Thin beds (20–50 cm) of nannofossil diatom ooze are present in Cores 138-850B-33X to -38X (309–367 mbsf).

Core 138-850B-33X contains a distinctive interval of greenish-gray to dark greenish-gray (5GY 5/1 to 5Y 4/1) nannofossil diatom ooze with radiolarians (Sections 4 and 5; 313.1–315.9 mbsf). Nannofossil diatom ooze is intermittently laminated and contains subtle color bands in Cores 138-850B-36X and -38X (~338–366 mbsf). These laminations are highly variable in color, but fine dark laminae are generally interspersed between somewhat thicker (2–3 mm) light laminae (Fig. 10). A zone containing up to 20% clay is present from Sections 138-850B-36X-5 to -38X-2 (344–360 mbsf).

A small laminated chert fragment was recovered in Core 850B-36X-4 at 70 cm (342 mbsf) within a 30-cm-thick bed of nannofossil diatom ooze that may have been very disturbed by drilling (Fig. 11). The diatom ooze above and below this disturbed zone is laminated. The depth of the chert corresponds to a bright reflector (high resistivity) at 344 mbsf in the FMS log.

Two additional layers of chert were recovered in Core 138-850B-38X (-38X-2, 65–66 cm, and 133–135 cm; 359.15 and 359.83 mbsf, respectively). The chert was dark olive and contained thin (millimeter-scale) layers of yellow (Fig. 12). The depths of the chert layers correspond to the upper two of a series of four bright, high-resistivity reflectors in the FMS log at 360.2, 360.4, 361.3, and 363.7 mbsf. The laminated diatom ooze surrounding the chert had not been disturbed by drilling. Although only 3.75 m was recovered in Cores 138-850B-38X and no sediment was recovered in Core 138-850B-39X, the correspondence in depths of the cherts to the depths of the FMS reflectors suggests that the upper two chert layers were recovered intact with little or no sediment disturbance or loss. Chert fragments also were found in Sections 138-850B-40X-4 and -40X-5 (381–383 mbsf), and -41X-1 (386 mbsf).

The pore-water chemistry of sediments below the chert layers is substantially different from that above the cherts, and little or no diffusive exchange appears across the chert interval. We found no evidence of major differences in the dominant lithology, abundance of microfossil groups, or other lithologic parameters above and below these cherts.

Although basalt was not recovered at Site 850, sediment rich in iron oxides was recovered in the deepest core (138-850B-42X), suggesting that the hard rock encountered by XCB drilling at 399.8 mbsf is basalt basement. This would be consistent with seismic records that suggest the presence of basement at 0.51 s of two-way traveltime (see "Seismic Stratigraphy" section, this chapter). The sediments below 120 cm in Core 138-850B-42X-1 (397–399.8 mbsf) are pale yellow (5Y 8/3) radiolarian diatom nannofossil ooze that contains manganese dendrites and small (1–2 cm) flat clasts of hematite. The hematite is generally surrounded by a thin (2–4 mm) layer of yellowish-olive crystalline material that may be hematite or nontronite.

Relationship of Lithology to Continuously Measured Parameters

GRAPE Density

GRAPE density data were available at the time that the core was being described. A relationship between calcium carbonate content and GRAPE density data has been observed in other areas of pelagic sedimentation where the calcium carbonate content of the sediment varies significantly and the principal dilutant of the calcareous sediment is biogenic silica (Mayer, 1991).

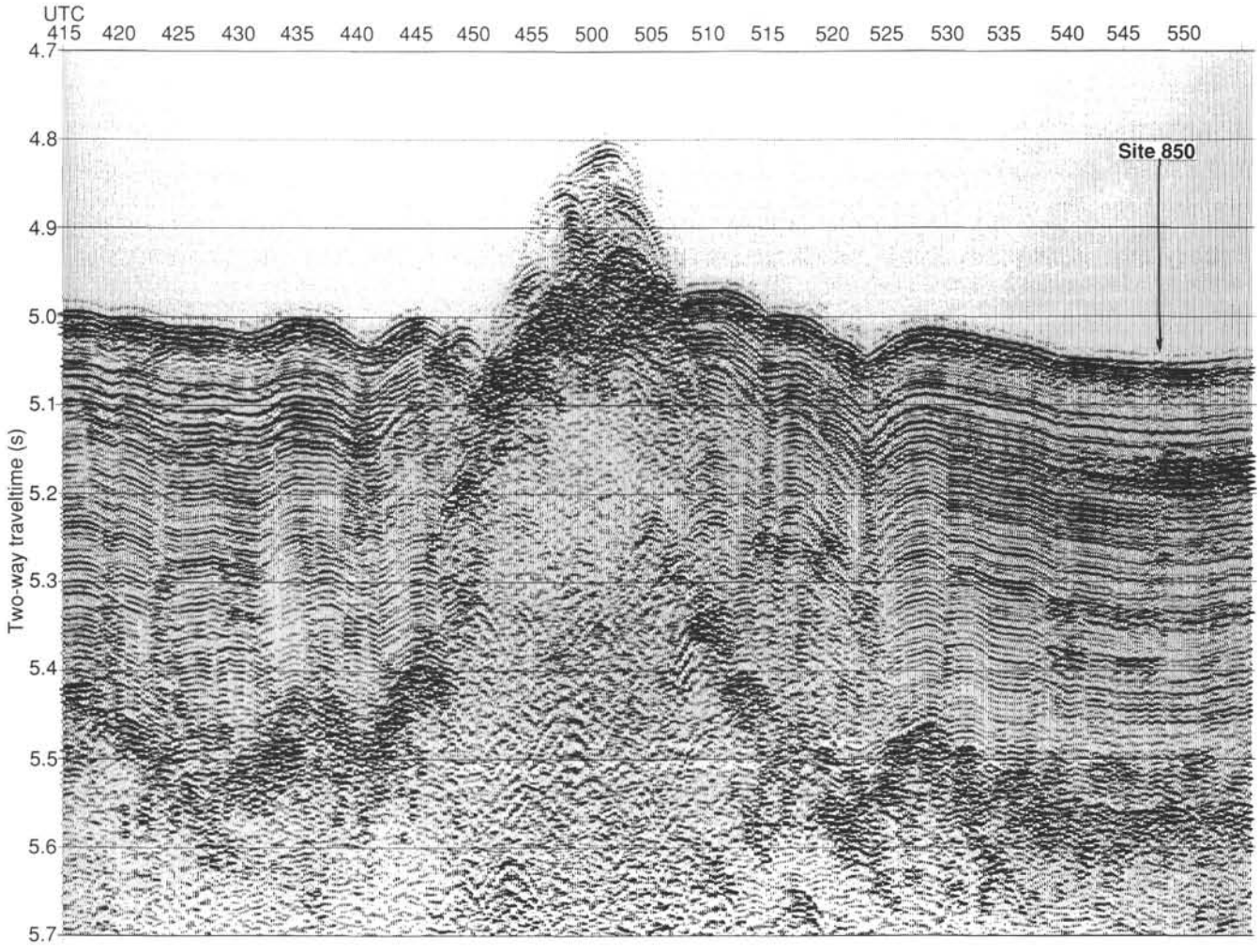

Figure 4. Digital seismic line collected by the *Resolution* during our approach to the site. Final position of Site 850 is shown.

The GRAPE density data suggest several scales of variability in carbonate content of the sediment, ranging from tens of meters to decimeters (Figs. 13 and 14). Although the calcium carbonate content of the sediment was not measured in samples at sufficient resolution to relate to variability at the decimeter scale, the sediments clearly showed variation in color (Fig. 13) and in smear slide microfossil composition that could be related to the GRAPE variation at this scale. On the large scale, low GRAPE values in the upper 75 m record dilution of nannofossil ooze by diatoms and radiolarians, the minima at 90 to 98 mbsf, 175 to 215 mbsf, and at 250 to 260 mbsf record dilution by diatoms, and the minimum between 290 and 340 mbsf is related to dilution by radiolarians.

Color Reflectance Spectroscopy

Lithology exerts a strong control on percent reflectance (Fig. 8). Although the first-order variations in average percentage of reflectance are related to carbonate content, sediments rich in diatoms generally have lower reflectance in the blue band (450–500 nm), and higher reflectance in the near-infrared bands (>700 nm). An example spectrum from a sample having 80% diatoms (based on smear slide analyses) is from Section 138-850B-21X-1 at 142 cm (Fig. 8). The nannofossil-rich sediments tend to have higher reflectance in the blue and green bands than in the near-infrared bands, and lowest reflectance in the red band. An extreme example of this in Site 850 is clayey radiolarian diatom nannofossil ooze (Section 138-850B-38X-2, 14 cm) that has highest reflectance in the blue and green bands (<550 nm) and lowest in the red and near-infrared bands (>650 nm).

The yellow and reddish-brown metalliferous sediments at the base of the site clearly have much higher red and near-infrared reflectance than the pale green and gray sediments above them. A secondary reflectance peak in the yellow band (550–600 nm; Fig. 8) is unique to this interval.

Magnetic Susceptibility

Large-scale magnetic susceptibility variations (Fig. 6) could not be attributed to specific sediment fractions observed in smear slides. The sediments between 53 and 70 mbsf have high magnetic susceptibility that follows the Al and Fe concentrations indicated on chemical logs (see "Downhole Measurements" section, this chapter). These elements are generally associated with the terrigenous sediment fraction. No difference can be discerned between clay content (estimated from smear slides) of the 53 to 70 mbsf interval and sediments above and below the interval.

The highest radiolarian concentrations in the upper 76 m occur in sediments between 53 and 67 mbsf, but they are marginally different from the concentrations in sediments above this depth interval. The association of high susceptibility, high terrigenous element concentrations and high radiolarian concentrations might imply lower biogenic sediment fluxes, but shipboard estimates of sedimentation rates (see "Sedimentation Rates" section, this chapter) and biogenic accu-

Table 1. Summary of coring operations at Site 850.

Core	Date (June 1991)	Time (UTC)	Depth (mbsf)	Length cored (m)	Length recovered (m)	Recovery (%)
138-850A-1H	13	1340	0.0–7.7	7.7	7.68	99.7
2H	13	1435	7.7–17.2	9.5	9.04	95.1
3H	13	1525	17.2–26.7	9.5	10.07	106.0
4H	13	1620	26.7–36.2	9.5	10.13	106.6
5H	13	1715	36.2–45.7	9.5	10.01	105.3
6H	13	1815	45.7–55.2	9.5	10.11	106.4
7H	13	1910	55.2–64.7	9.5	10.02	105.5
8H	13	2010	64.7–74.2	9.5	10.06	105.9
Coring totals				74.2	77.12	103.9
138-850B-1H	13	2150	3.0–12.5	9.5	9.78	103.0
2H	13	2245	12.5–22.0	9.5	9.65	101.0
3H	13	2335	22.0–31.5	9.5	9.74	102.0
4H	14	0035	31.5–41.0	9.5	10.07	106.0
5H	14	0140	41.0–50.5	9.5	10.08	106.1
6H	14	0240	50.5–60.0	9.5	10.10	106.3
7H	14	0345	60.0–69.5	9.5	10.11	106.4
8H	14	0445	69.5–79.0	9.5	10.09	106.2
9H	14	0540	79.0–88.5	9.5	10.08	106.1
10H	14	0655	88.5–98.0	9.5	9.99	105.0
11X	14	0750	98.0–107.5	9.5	8.90	93.7
12X	14	0840	107.5–117.1	9.6	9.50	98.9
13X	14	0940	117.1–126.8	9.7	9.64	99.4
14X	14	0104	126.8–136.4	9.6	9.58	99.8
15X	14	1130	136.4–146.1	9.7	9.65	99.5
16X	14	1230	146.1–155.7	9.6	9.50	98.9
17X	14	1325	155.7–165.0	9.3	9.20	98.9
18X	14	1415	165.0–174.2	9.2	9.65	105.0
19X	14	1505	174.2–183.8	9.6	9.75	101.0
20X	14	1600	183.8–193.5	9.7	9.73	100.0
21X	14	1650	193.5–203.1	9.6	9.65	100.0
22X	14	1750	203.1–212.8	9.7	9.73	100.0
23X	14	1840	212.8–222.5	9.7	9.59	98.8
24X	14	1930	222.5–232.1	9.6	9.45	98.4
25X	14	2030	232.1–241.8	9.7	9.63	99.3
26X	14	2125	241.8–251.0	9.2	9.69	105.0
27X	14	2220	251.0–260.7	9.7	9.79	101.0
28X	14	2310	260.7–270.3	9.6	9.56	99.6
29X	15	0000	270.3–279.9	9.6	9.63	100.0
30X	15	0055	279.9–289.6	9.7	9.67	99.7
31X	15	0150	289.6–299.2	9.6	9.74	101.0
32X	15	0250	299.2–308.9	9.7	9.02	93.0
33X	15	0345	308.9–318.6	9.7	9.85	101.0
34X	15	0440	318.6–328.2	9.6	9.90	103.0
35X	15	0530	328.2–337.8	9.6	9.96	104.0
36X	15	0625	337.8–347.5	9.7	6.87	70.8
37X	15	0720	347.5–357.1	9.6	9.78	102.0
38X	15	0825	357.1–366.8	9.7	3.67	37.8
39X	15	0930	366.8–376.4	9.6	9.86	103.0
40X	15	1035	376.4–386.1	9.7	9.78	101.0
41X	15	1140	386.1–395.8	9.7	9.85	101.0
42X	15	1315	395.8–399.8	4.0	4.12	103.0
Coring totals				396.8	393.58	99.2

mulation rates (see "Organic Geochemistry" section, this chapter) for this interval, however, are as large as those that precede or follow it. Therefore, it may be that the susceptibility maximum may result from a subtle change in the amount of terrigenous material that was not detected with smear slide data.

Meter-scale variability in susceptibility was sometimes clearly related to lithologic variation. For example, we found some intervals in which susceptibility co-varies with GRAPE data, while in other intervals, no clear relationship could be seen (Fig. 15).

Spikes in susceptibility, especially obvious between 105 and 165 mbsf, are associated with distinctive thin (1–3 cm) greenish-gray layers. The microfossil composition of these layers was similar to that of adjacent sediments, but these contained an unidentified sulfide mineral other than pyrite.

Trace Fossils

A wide range in bioturbation intensity, preservation, and ichnofacies is present in the sediments of Site 850. Burrowing varies from slight to intense in all lithologies except the laminated diatom oozes. Solid burrows and *Planolites* are the most common trace fossils in all lithologies. The observed intensity was generally greater, however, in interbeds of darker, more diatom- or radiolarian-rich lithologies. Detailed sediment structure and trace fossils were particularly clear in the surfaces of cores that had been cut with a saw (Cores 138-850B-32X through -42X, 299–400 mbsf; Fig. 16).

In the foraminifer- and radiolarian-rich nannofossil ooze between 0 and 76 mbsf, bioturbation varied from slight to intense. Because few dark interbeds were seen between 10 and 25 mbsf, bioturbation

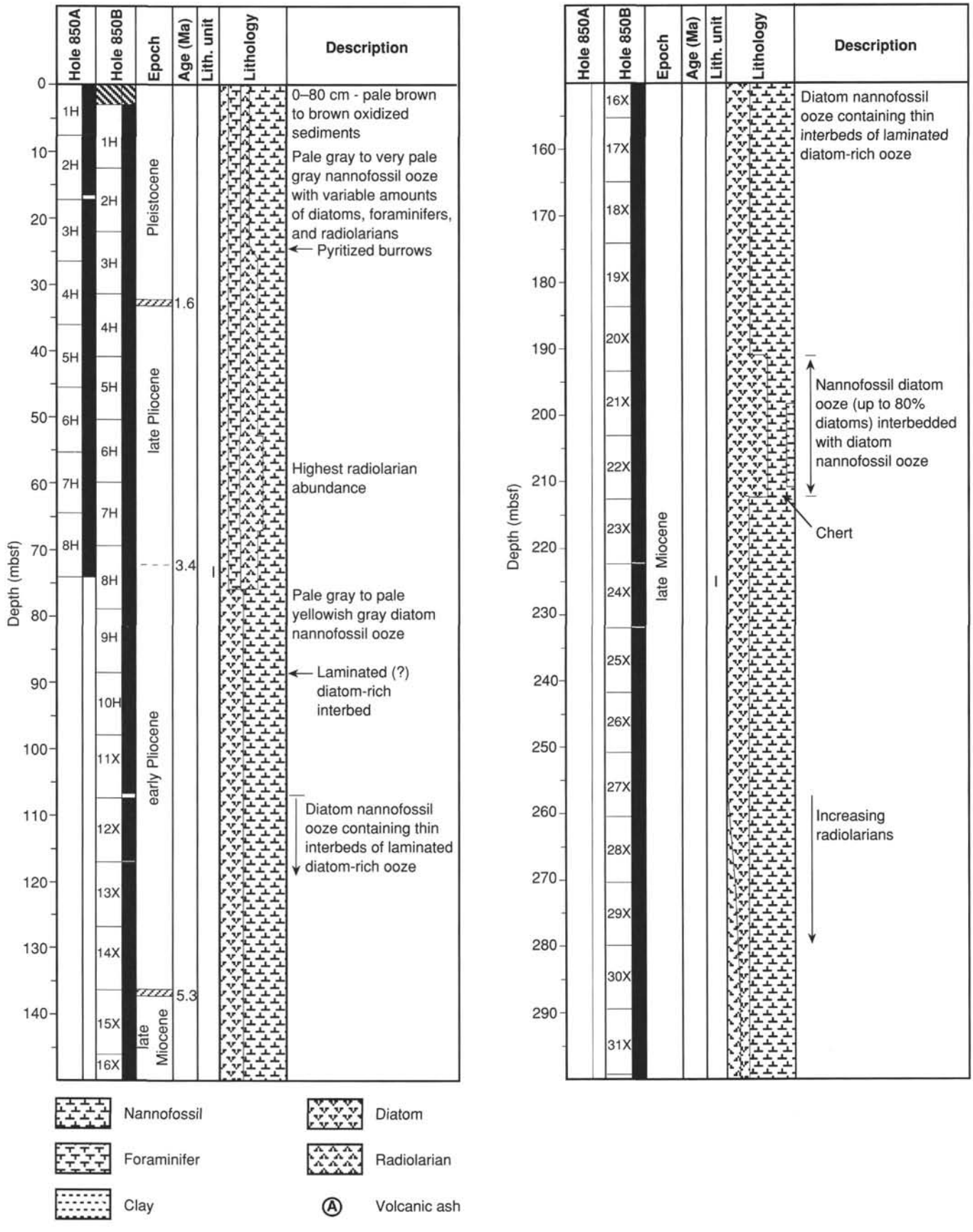

Figure 5. Lithostratigraphic summary of Site 850.

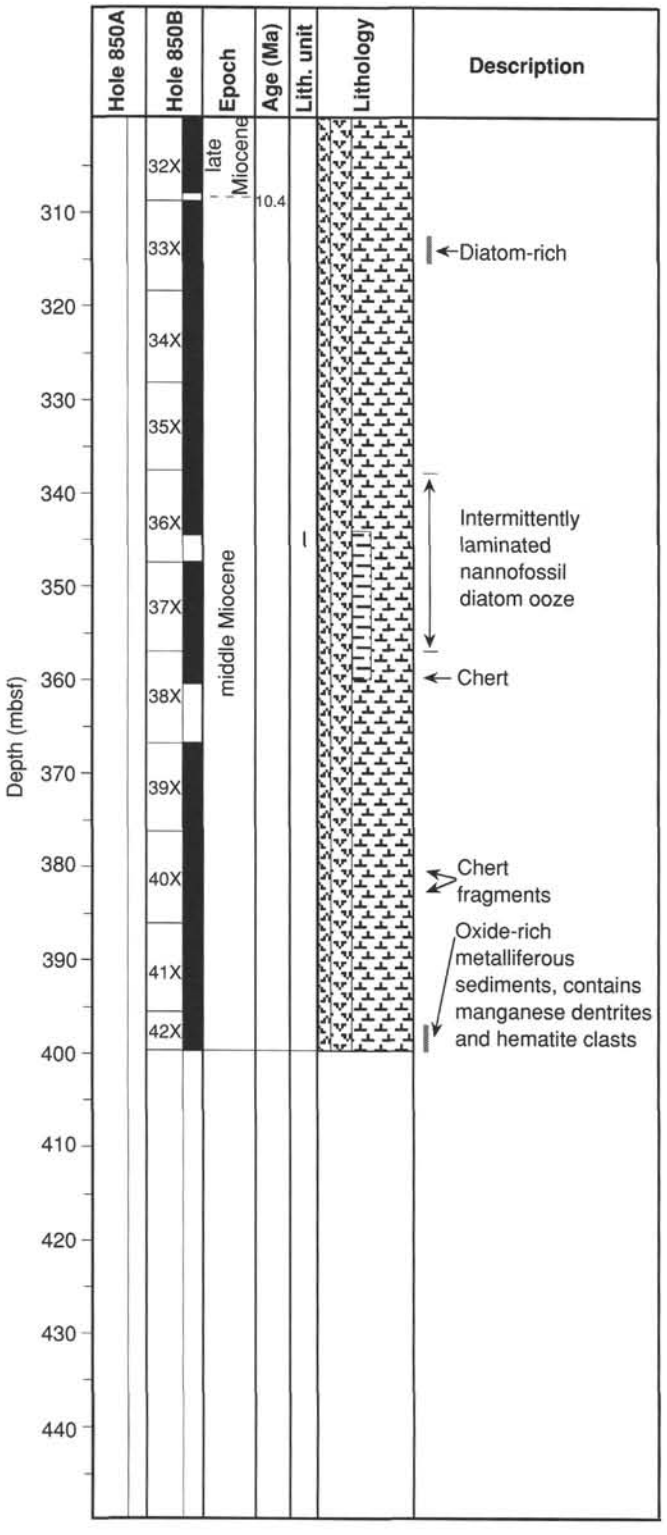

Figure 5 (continued).

appears slight in this depth range. *Skolithos* is present within the top meter and only rarely thereafter. We noted this at about 23 and 65 mbsf. Burrows having loose, pyrite-rich fill are common between about 22 and 40 mbsf. Open burrows are common above 20 mbsf, but are present as deep as 58 mbsf. *Chondrites* and *Zoophycos* were observed only at about 30 mbsf in this lithology. The almost total absence of *Chondrites* within the top 70 m may be because these trace fossils are difficult to see in very soft unconsolidated sediments.

Below 76 mbsf, within the diatom-nannofossil ooze and the lower radiolarian-rich zone, *Chondrites* is common, both within burrow fills and the sediment matrix. *Zoophycos* is very rare below 76 mbsf, but is present within a dark bed at 255 mbsf, between 320 and 330 mbsf, and in a very thin form at 388 mbsf.

Bioturbation appears to be absent in the thinly banded and laminated nannofossil diatom ooze (see Fig. 10). The nannofossil diatom ooze intervals are interbedded on a decimeter to meter scale with diatom nannofossil ooze (Fig. 17) that is generally highly bioturbated (Fig. 18). In many of the diatom ooze beds, bioturbation appears to have ceased abruptly at the sharp basal contact of the laminated sediment (Fig. 17B). The upper boundary of the decimeter-thick diatom ooze beds is generally more gradational.

Summary of Lithology

The dominant lithology at Site 850 is nannofossil ooze with varying amounts of foraminifers, radiolarians, and diatoms. The uppermost ~76 m of the sediments is richer in foraminifers and radiolarians than the average for the site, as indicated by smear slide analyses. Sediments between 76 and 288 mbsf are dominated by diatom nannofossil ooze with interbeds of nannofossil diatom ooze. Sediments between 288 and 395 mbsf are radiolarian and diatom nannofossil oozes. The 5 m above the inferred basement are iron oxide-rich metalliferous sediment.

BIOSTRATIGRAPHY

Sediments recovered from the two holes (850A and 850B) cored at Site 850 provide a continuous sedimentary record of the upper Pleistocene through upper middle Miocene sequence. Calcareous nannofossils, foraminifers, radiolarians, and diatoms are present throughout the sequence and have been used to develop the biostratigraphic framework (Tables 3–6; Fig. 19). Preservation of the calcareous nannofossils, radiolarians, and diatoms is moderate to good. The one exception is the lowermost core (Core 138-850B-42X), which has no diatoms. Preservation of the foraminifers is moderate down through Core 138-850B-7H and poor through the remainder of the sequence.

The epoch boundaries have been placed approximately as follows:

Boundary	Hole	Depth (mbsf)	Depth (mcd)	Event
Pleistocene/ Pliocene	850A	34.80–37.30	31.18–33.30	B *Gephyrocapsa oceanica* s.l.
	850B	33.39–32.01	31.74–32.01	
late/early Pliocene	850A	78.90–80.31	69.90–71.30	T *Reticulfenestra pseudoumbilicus*
	850B	79.55–79.75	71.80–72.00	
Pliocene/ Miocene	850B	144.13–144.50	136.38–136.73	T *Discoaster quinqueramus*
upper/middle Miocene	850B	355.85–357.36	348.10–347.61	T *Coccolithus miopelagicus*

B = bottom occurrence; T = top occurrence.

The lowermost portion of the recovered sequence (Sample 138-850B-42X-CC) was placed in the lower part of calcareous nannofossil Zone CN5b, indicating an age younger than 12.2 Ma. The stratigraphically lowest sample that contains radiolarians (138-850B-42X-CC) was assigned to the *Diartus pettersoni* Zone and contains the species *Carpocanium cristata*, whose last occurrence was approximately 10 Ma. The lowermost sample containing diatoms (Sample 138-850B-41X-CC) has been assigned to the diatom *Craspedodiscus coscinodiscus* Zone and includes species that indicate an age between 10.7 and 11.1 Ma.

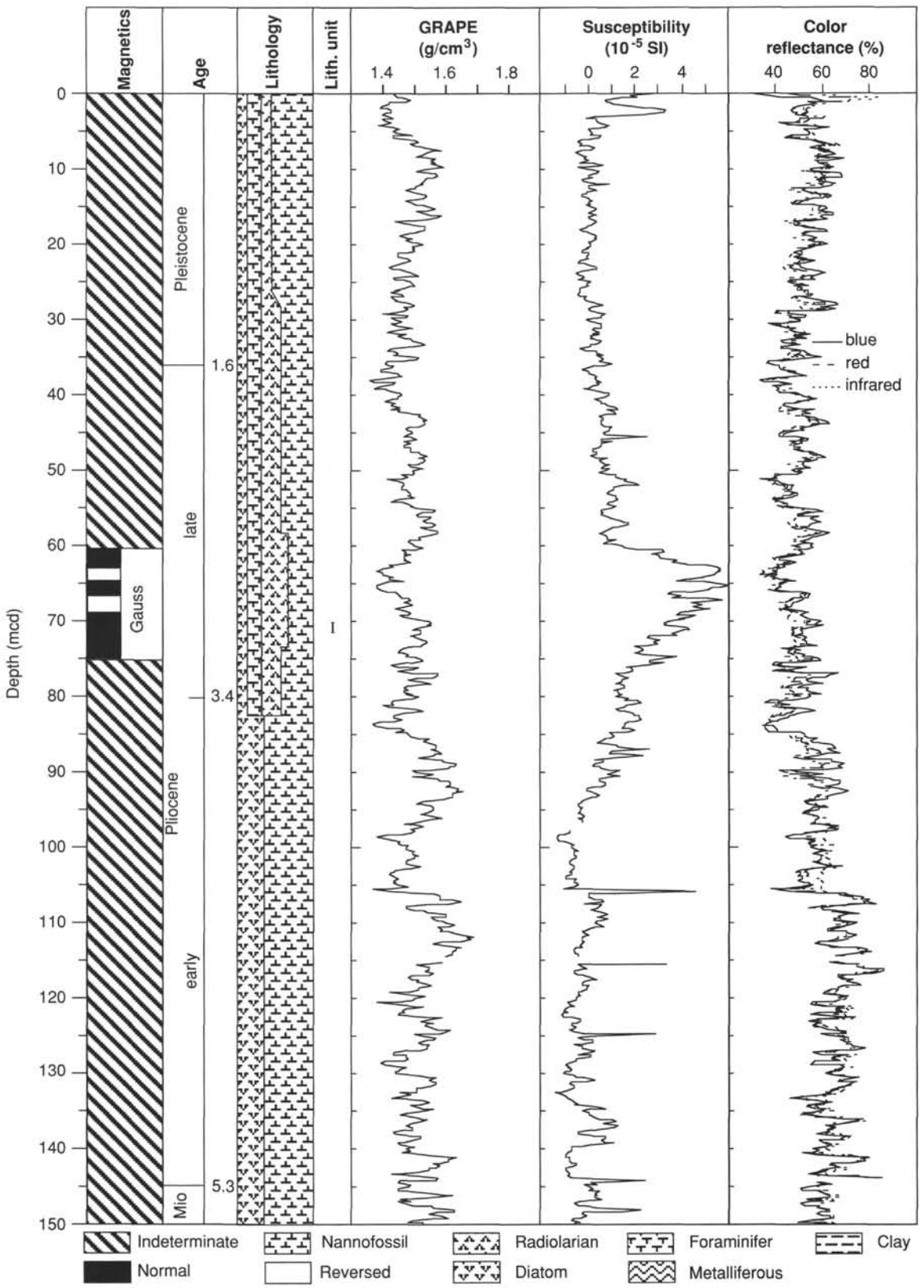

Figure 6. Composite summary of Site 850 lithology, age, magnetic data, GRAPE, and percentage of color reflectance. Composite data consits of sections spliced together from multiple holes drilled at the site. Data are shown plotted vs. composite depth, the new depth scale used when composite sections are constructed. GRAPE density, susceptibility, and color reflectance data have been smoothed using a 20-point Gaussian filter.

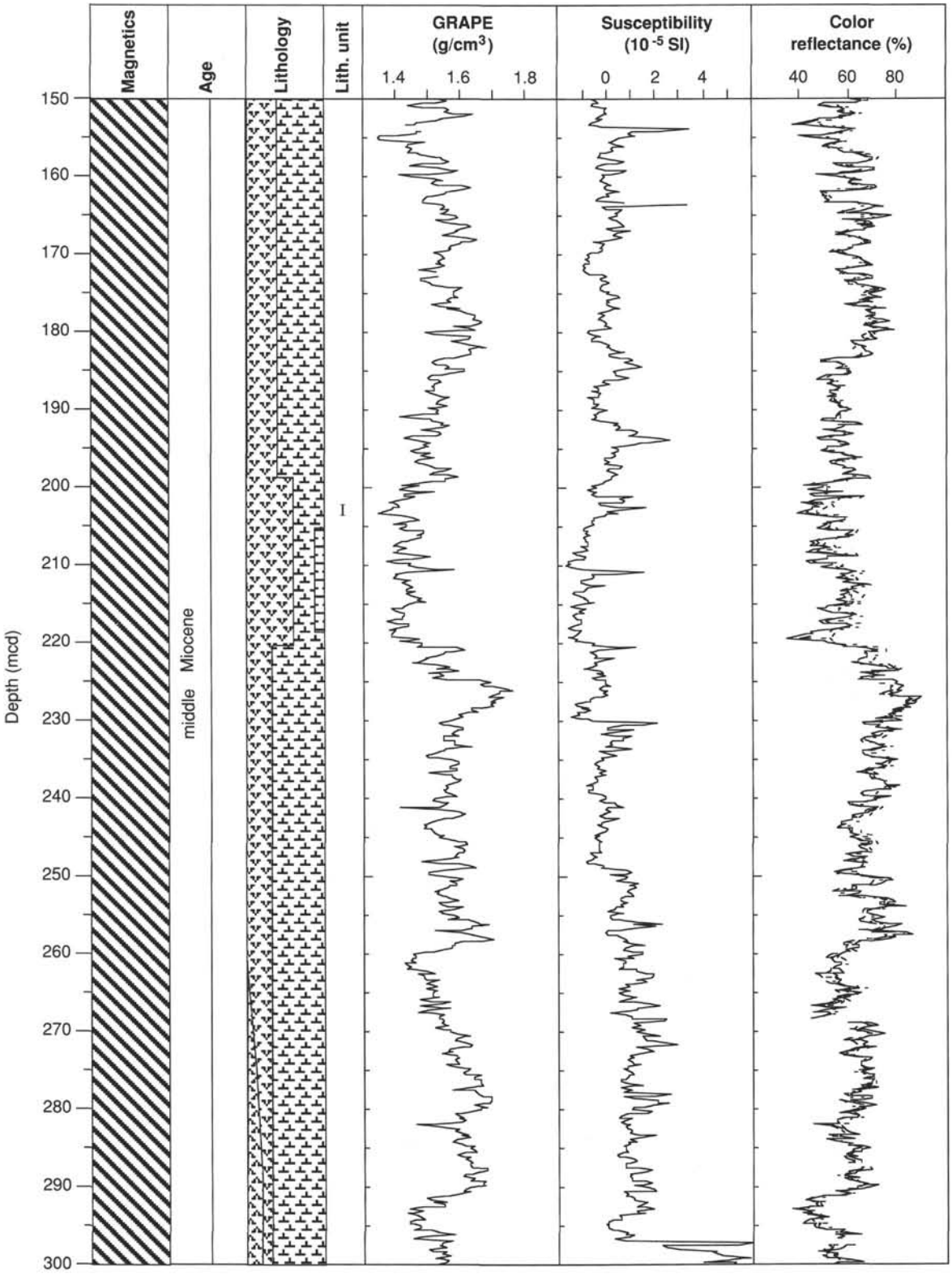

Figure 6 (continued).

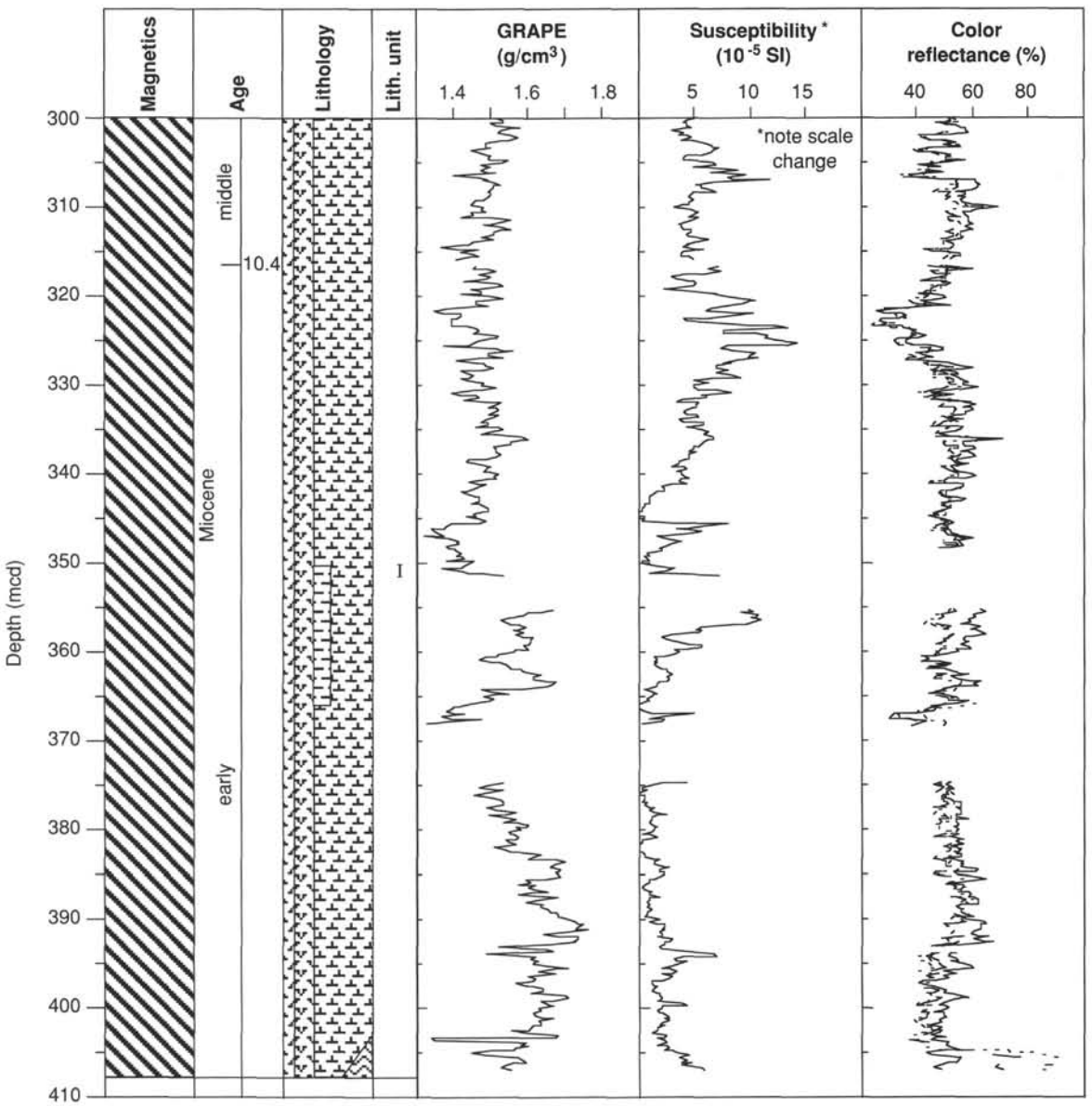

Figure 6 (continued).

The eight cores recovered from Hole 850A sampled the uppermost part of the section down to the diatom *Nitzschia jouseae* Zone, the radiolarian *Phormostichoartus doliolum* Zone, and Zone CN11 of calcareous nannofossils. The estimated age for the deepest sample from this hole (138-850A-8H-CC) is between 3.5 and 4.4 Ma.

The following discussion focuses on biostratigraphic results from Holes 850A and 850B.

Calcareous Nannofossils

Calcareous nannofossils recovered at Site 850 represent a stratigraphic succession from the upper Pleistocene (Zones CN14b from Okada and Bukry, 1980, and NN20 from Martini, 1971) through the upper middle Miocene (Zones CN5b and NN7) (Fig. 19). Nannofossils are abundant and generally well preserved through all of the sequence. The Pleistocene interval (Cores 138-850A-1H through -4H and -850B-1H through -3H) is characterized by well-preserved assemblages with *Pseudoemiliania lacunosa, Calcidiscus* spp., various morphotypes of *Gephyrocapsa* spp., and helicoliths. Discoasterids are common to abundant in the Pliocene (Cores 138-850A-4H through -8H and -850B-5H through -14X). In the Miocene (Cores 138-850B-15X through -42X), discoasterids fluctuate in abundance, varying from assemblages having abundant, diversified, and well-preserved asteroliths to assemblages having rare and strongly overgrown forms (mainly in the lower part of the section, Cores 138-850B-35X through -42X). Moderate etching was observed on placoliths in some samples in the Pliocene.

The nannofossil biostratigraphic events recognized at Site 850 are reported in Table 3. The first occurrence of *Gephyrocapsa oceanica* s.l. was recorded between Samples 138-850A-4H-4, 60 cm, and -4H-5, 60 cm, and between Samples 138-850B-3H-CC and -4H-1, 51 cm. This event approximates the Pleistocene/Pliocene boundary.

The Pliocene nannofossil assemblages are characterized by helicolithids, discoasterids, different morphotypes of *Reticulofenestra* spp., *Calcidiscus* spp., *Coccolithus pelagicus*, ceratolithids, and sphenoliths in the lower Pliocene interval. The nannofossil event which approximates the upper Pliocene/lower Pliocene boundary is the last occurrence of *Reticulofenestra pseudoumbilicus*, recorded between

Table 2. Summary of logging operations at Site 850.

Local day (June 1991)	Local time	Cumulative hours	Base of string (mbsf)	Comments
15	0615	0.0		Last core on deck
15	0810	1.9		Start rig up
15	0930	3.2		Geophysical tool rigged up (NGT/SDT/HLDT/DIT/TLT); RIH
15	1103	4.8	400.2	At TD, start main log up, no heave compensator
15	1211	5.9	79.2	End main log; close calipers and POOH
15	1425	8.2		Geophysical tool string at wellhead
15	1455	8.7		RIH with geochemical string (NGT/ACT/GST/TLT)
15	1602	9.8	0.0	Pause at mud line
15	1615	10.0	400.2	At TD; no heave compensator; calibrate while moving up slowly
15	1621	10.1	399.3	GST calibrated; start main log
15	1808	11.9	0.0	Stop main log; POOH
15	1920	13.1		Geochemical string at wellhead
15	2010	13.9		RIH with FMS string (NGT/GPIT/FMS)
15	2141	15.4	399.9	At TD, start FMS repeat log; no heave compensator
15	2155	15.7	304.8	End repeat section, drop to TD
15	2200	15.8	399.9	At TD, start main log up
15	2244	16.5	88.4	Stop main log, close calipers eventually, try to POOH
15	2317	17.0		Trouble getting back into pipe, finally made it and POOH
16	0015	18.0		FMS string at wellhead
16	0050	18.6		Rigged down from logging

Samples 850A-8H-4, 70 cm, and -8H-5, 61 cm, and between Samples 850B-8H-2, 80 cm, and -8H-2, 100 cm.

The last occurrence of *Discoaster quinqueramus* defines the boundary between Zones CN10 and CN9 (NN12/NN11) and approximates the Pliocene/Miocene boundary. This event is recorded between Samples 850B-14X-CC and -15X-1, 35 cm. In the uppermost part of their stratigraphic range *D. quinqueramus* and *D. berggreni* are common and well preserved; however, they decline in abundance through the upper Miocene interval. Ceratolithids, such as *Amaurolithus primus* and *A. delicatus* were not observed in the upper Miocene interval. The absence of these biostratigraphic markers precludes a precise zonal assignment for the interval between Cores 850B-16X and -32X. Discoasterids are almost completely missing in this interval, and peaks in abundance of *Dictyococcites* spp. (<6 µm in size) and *Reticulofenestra* spp. were observed.

Only rare and scattered specimens of *Discoaster hamatus*, characteristic of the Zone CN7 (NN9), were observed in samples from Cores 850B-34X and -35X, and the first and last occurrences of this species cannot be precisely identified. The last occurrence of *Coccolithus miopelagicus*, which approximates the upper middle Miocene boundary, is recorded between Samples 138-850B-37X-1, 60 cm, and -37X-2, 61 cm.

Because of the absence of zonal markers, the precise biostratigraphic assignment of the lowermost part of the sedimentary sequence at Site 850 (Cores 138-850B-38X through -41X) was difficult. *Catinaster coalitus* is missing; thus, it was not possible to identify Zone CN6 (NN8). However, samples observed in Core 138-850B-41X do contain rich assemblages with common *Discoaster kugleri*, which suggests that the basal part of the sequence is within the upper middle Miocene Subzone CN5b (Zone NN7).

Planktonic Foraminifers

Planktonic foraminifers are abundant in Cores 138-850B-1H through -10H, but in Sample 850B-9H-CC, are rare. These microfossils are rare to few below Core 138-850B-10H, except in Sample 138-850B-17H-CC, where these are common. Preservation is moderate in Cores 138-850B-1H through -7H and poor throughout the remainder of the sequence.

The dominant components of the coarse-fraction residues are foraminifers in Cores 138-850B-1H-CC through -3H-CC and radiolarians throughout the remainder of the section. Other major coarse-fraction components below Core 138-850B-3H are few to common sponge spicules and rare to few echinoid spines and fish teeth. Below Core 138-850B-9H, pyrite is rare to common. Volcanic glass is rare in samples below Core 138-850B-33X; however, few to common glass shards were observed in Samples 138-850B-34X-CC through -36X-CC. Manganese micronodules are common in Sample 138-850B-42X-CC.

Planktonic foraminiferal datums identified in the sequence are given in Table 4. The base of Zone N22 was equated to the last occurrence of *Globorotalia limbata* in Sample 138-850B-4H-CC and the base of Zone N21 to the last occurrence of *Sphaeroidinellopsis* in Sample 138-850B-6H-CC. The base of Zone N18 was placed at the first occurrence of *Globorotalia tumida* in Sample 138-850B-14X-CC, although dissolution may possibly curtail the lower range of this species. The interval from Sample 138-850B-15X-CC through -24X-CC was assigned to Zone N17 on the basis of the occurrence of rare morphotypes referable to *Globorotalia plesiotumida*. The lower part of the sequence (below Core 138-850B-24X) was unzoned because of the rarity of the planktonic fauna. Here, the assemblages contain only a few nondiagnostic species, including *Globoquadrina venezuelana, Globigerinoides sacculifer*, and *Globigerinoides obliquus*.

Radiolarians

Radiolarians sampled from Site 850 range in age from the Quaternary (*Collosphaera tuberosa* Zone) to the late middle Miocene (*Diartus pettersoni* Zone). The most recent radiolarian zone (*Buccinosphaera invaginata*) was not identified. The oldest material recovered that could be identified to the zonal level (*D. pettersoni* Zone) is from Sample 138-850B-42X-CC.

Preservation and abundance of the radiolarians are good within the Pleistocene–Pliocene section. Only a trace of reworking of older radiolarians into the upper Pliocene part of the section was seen in Samples 138-850B-5H-4, 110 cm; -6H-6, 110 cm; and -7H-CC. The Pleistocene–Pliocene section appears to be complete, with all the major zones and radiolarian datums recognized in the samples studied. The *Phormostichoartus fistula* Zone appears to be particularly expanded at this site. Specimens of *P. fistula* are comparable in abundance to those found at Site 849; however, their generally low abundance makes their last detected occurrence an unreliable datum for intersite correlations. Sufficient specimens of *Spongaster pentas* and *Spongaster berminghami* were found at this site to make useful comparisons with Site 849, but their scattered occurrence in other Leg 138 sites prevents them from being a useful marker for correlation.

The high accumulation rates in the lower Pliocene and upper Miocene greatly expands the *Phormostichoartus doliolum* and *So-*

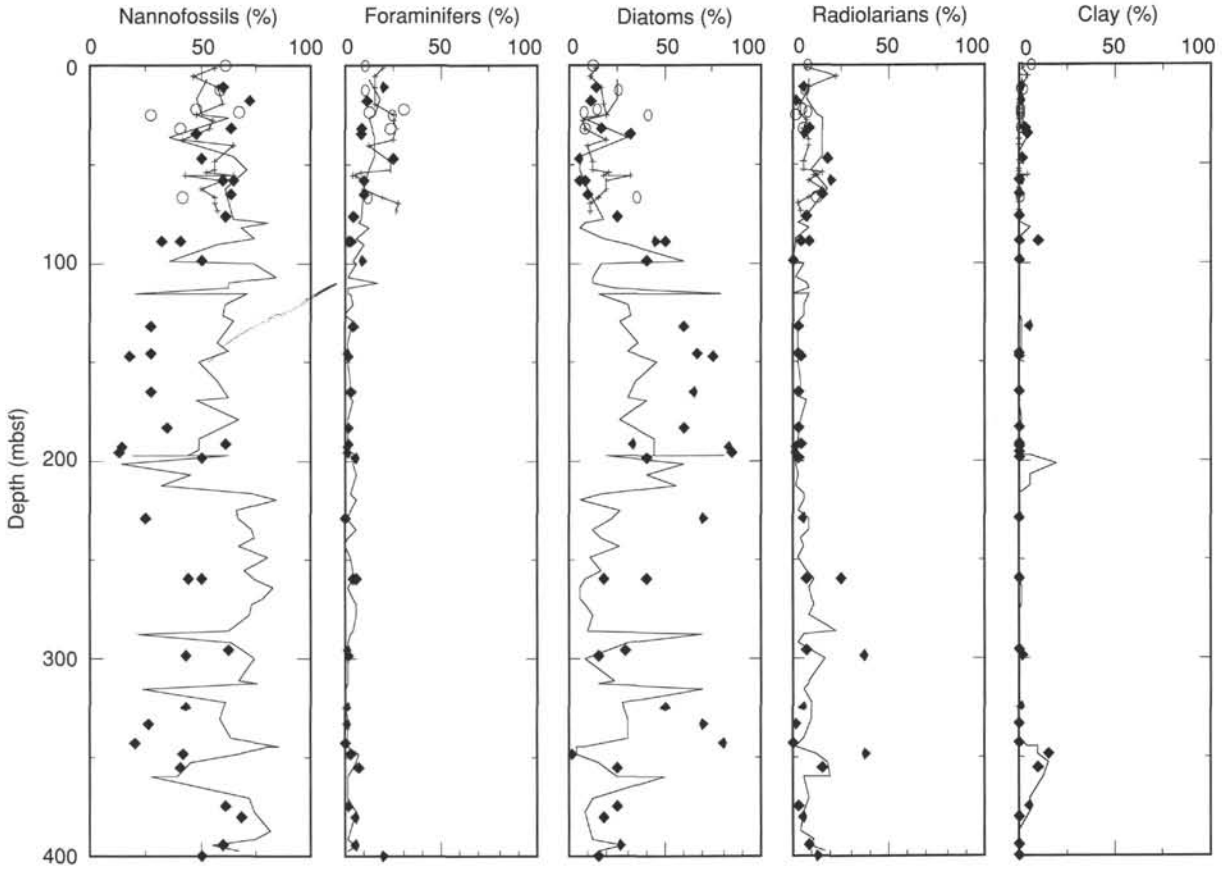

Figure 7. Summary of smear slide data from Site 850. Line with cross = Hole A dominant lithology; solid line = Hole B dominant lithology; filled diamonds = Hole A minor lithology; open circles = Hole B minor lithology.

lenosphaera omnitubus zones at this site, and most datums within this interval can be closely constrained in time. The occurrence of *Acrobotrys tritubus*, however, is scattered, and its first and last appearances cannot be used as reliable datums.

Radiolarians were common to abundant throughout the upper to middle Miocene part of the section, and preservation was generally good. Below Core 138-850B-31X, preservation decreases somewhat, but remains either moderate or moderately good. Moderately well-preserved radiolarians are present in the core-catcher sample of the deepest recovered core (138-850B-42X-CC). The oldest reliable datum (Table 5) is the last appearance of *Carpocanium cristata* (between Samples 138-850B-37X-CC and -38X-1, 127 cm). This datum occurs within the middle part of the *Diartus pettersoni* Zone and has an age of 10 (±0.1) Ma within the tropical Indian and Pacific oceans (Johnson and Nigrini, 1985).

Diatoms

Diatoms are present in the Quaternary (*Pseudoeunotia doliolus* Zone) through middle Miocene (*Crasepedodiscus coscinodiscus* Zone) sediments recovered from Site 850. Diatom preservation varies through the section, exhibiting moderate to good preservation in the Quaternary through upper Miocene interval and moderate to poor preservation in the lowermost upper Miocene through middle Miocene interval. Abundance of diatoms varies from few to abundant. Diatoms were not observed in samples examined from Core 138-850B-42X.

The diatom assemblage observed in samples from Site 850 consists of species typical of the low-latitude eastern equatorial Pacific Ocean (Table 6). Characteristic species include *Azpeitia nodulifer, Ethmodiscus rex, Hemidiscus cuneiformis, Nitzschia fossilis, Nitzschia jouseae, Nitzschia reinholdii, Pseudoeunotia doliolus, Rhizosolenia bergonii, Thalassionema nitzschioides, T. nitzschioides var. parva, Thalassiosira convexa,* and *Thalassiothrix longissima*.

Two holes were cored at Site 850. Hole 850A extends from the *P. doliolus* Zone to the *N. jouseae* Zone. Hole 850B extends from the *P. doliolus* Zone to the *Craspedodiscus coscinodiscus* Zone.

Core 138-850A-1H was assigned to the *P. doliolus* Zone on the basis of the occurrence of *P. doliolus* stratigraphically above the last occurrence of *Nitzschia reinholdii*. The last occurrence of *N. reinholdii* was observed in Samples 138-850A-2H-CC and -850B-1H-CC, which allowed us to place the *P. doliolus/N. reinholdii* boundary between Samples 138-850A-1H-CC and -2H-CC and in the upper portion of Core 138-850B-1H.

Samples 138-850A-2H-CC through -4H-3, 60 cm, and -850B-1H-CC through -4H-1, 60 cm, were placed in Subzone B of the *N. reinholdii* Zone. This zonal assignment is based on the presence of *N. reinholdii* and *P. doliolus* stratigraphically above the last occurrence of *Rhizosolenia praebergonii*. Samples 138-850A-4H-1, 60 cm, through -5H-2, 60 cm, and -850B-4H-2, 70 cm, through 4H-4, 70 cm, were assigned to Subzone A of the *N. reinholdii* Zone, based on the co-occurrence of *P. doliolus* and *R. praebergonii*. Samples 138-850A-5H-5, 60 cm, through -6H-CC cm and -850B-4H-CC through -7H-1, 70 cm, were placed in the *Rhizosolenia praebergonii* Zone. This zone has been divided into three subzones on the basis of the occurrences of *T. convexa* and *N. jouseae*. Samples 138-850A-5H-5, 60 cm, and -5H-6, 65 cm, and 138-850B-4H-CC and 5H-2, 70 cm, represent the interval between the first occurrence of *P. doliolus* and the last occurrence of *T. convexa*; this interval has been placed in Subzone C of the *R. praebergonii* Zone. Samples 138-850A-5H-7, 35 cm, through -5H-CC and -850B-5H-3, 70 cm, through -5H-CC have been assigned to Subzone B of this zone, based

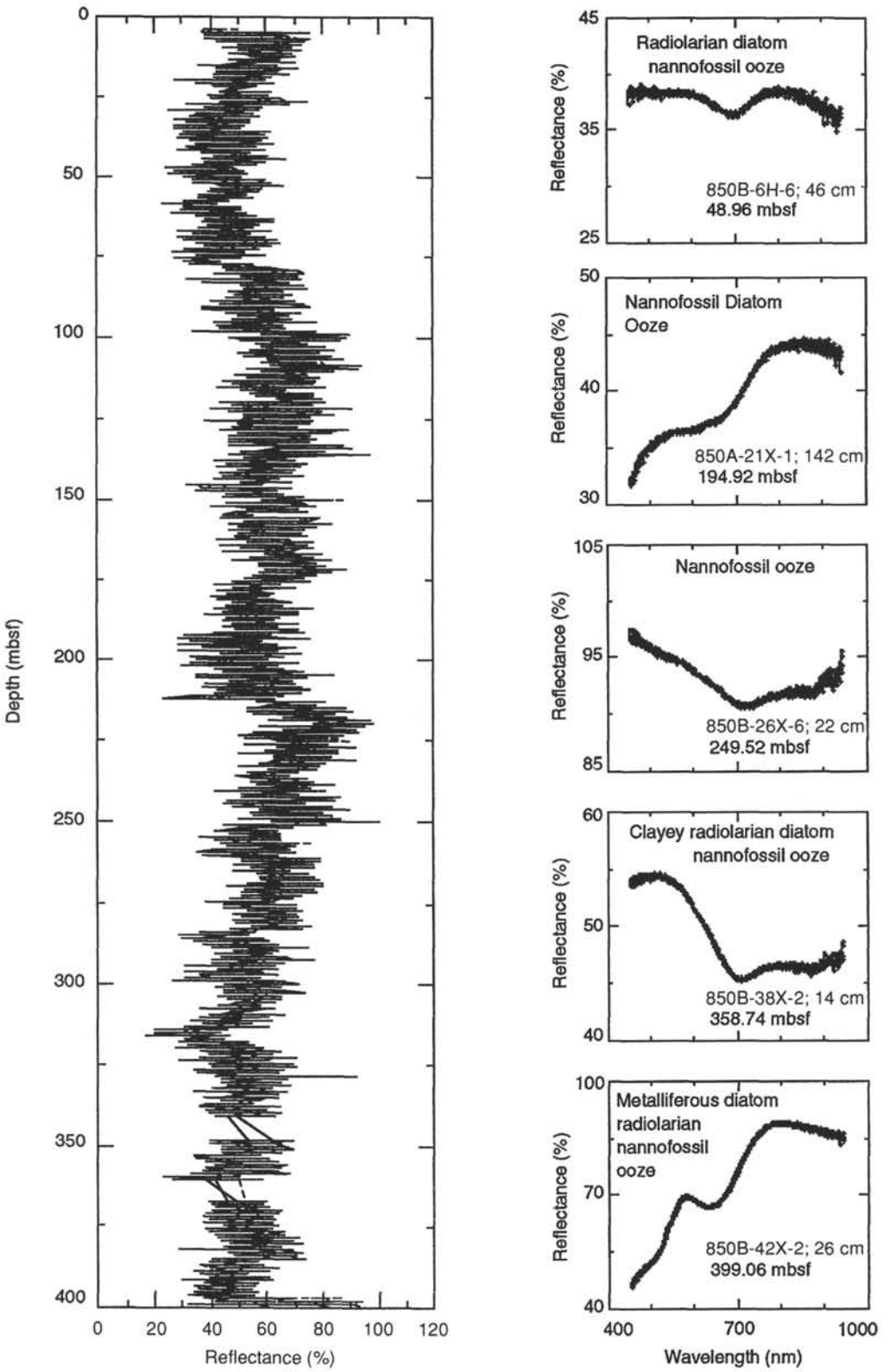

Figure 8. Left, percentage of reflectance of the blue (450–500 nm) = solid line, red (650–700 nm) = dashed line; and infrared (850–900 nm) = dotted line, color wavelength bands at Site 850. Right, examples of color reflectance spectra for lithologies at Site 850.

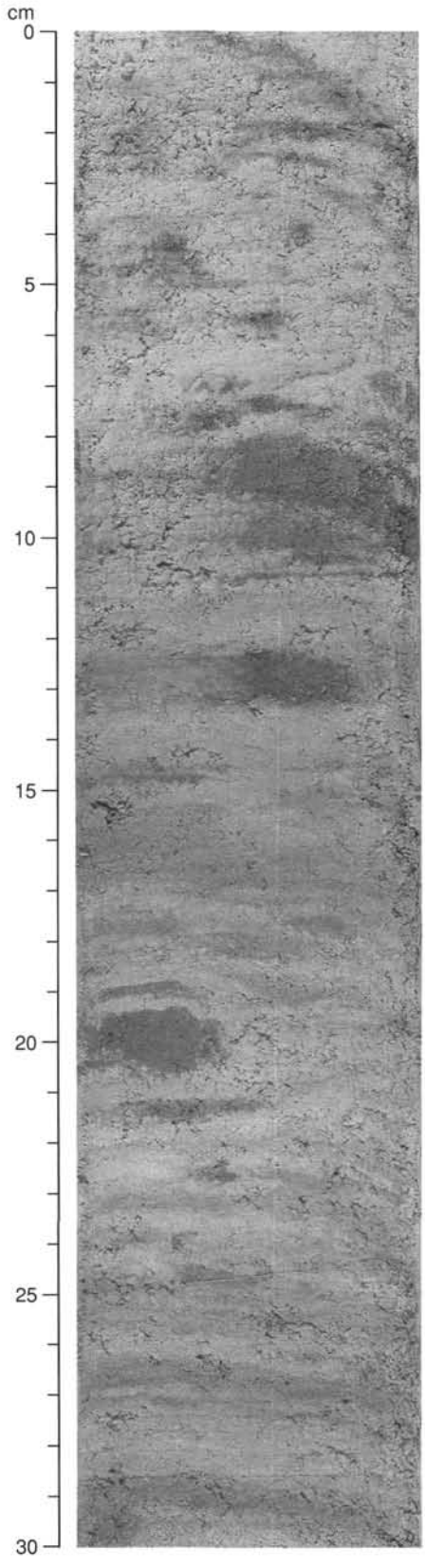

Figure 9. Top of an interval of thin color bands (laminations) in nannofossil diatom ooze (Core 138-850B-10H-7, 0–30 cm) showing increased bioturbation (including *Planolites*) and decreased continuity of thin-banding upward as the lithology grades to diatom nannofossil ooze.

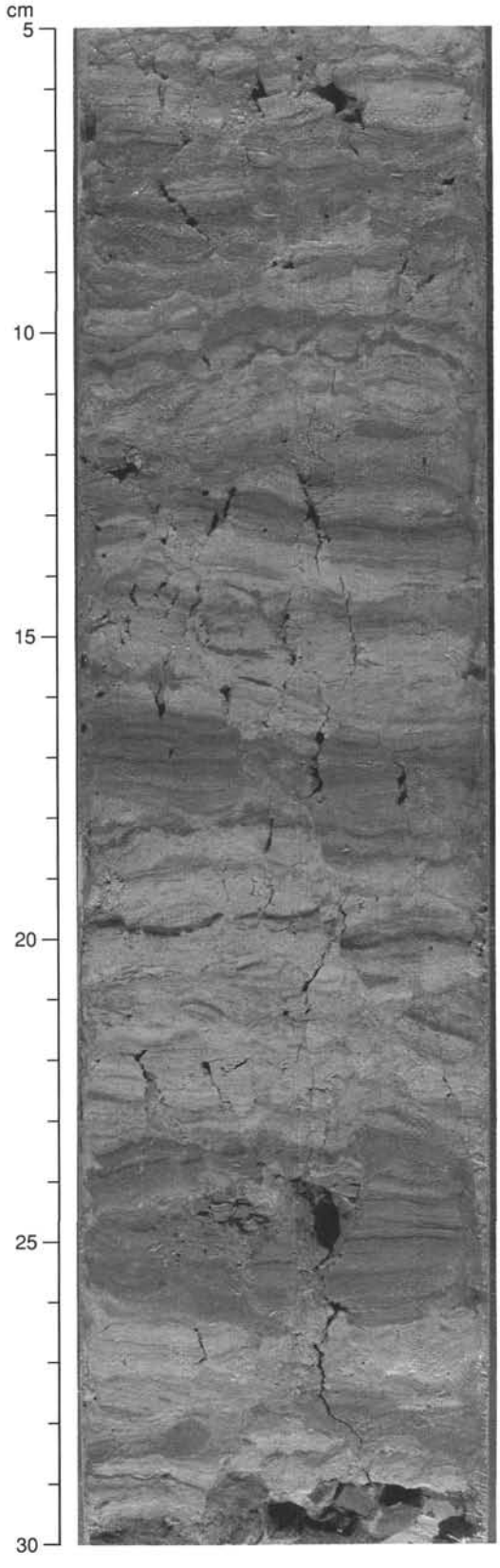

Figure 10. Laminated diatom ooze (Section 138-850B-38X-3 at 5–30 cm).

Table 3. Sample and depth constraints of calcareous nannofossil events for Site 850.

Event	Hole 850A			Hole 850B		
	Interval (cm)	Depth (mbsf)	Depth (mcd)	Interval (cm)	Depth (mbsf)	Depth (mcd)
T *Pseudoemiliania lacunosa*	2H-2, 106–2H-3, 100	10.26–11.70	11.81–13.25	1H-4, 60–1H-5, 63	8.10–9.63	8.10–9.63
B *Gephyrocapsa* sp. 3	3H-1, 110–3H-2, 103	18.30–19.73	19.95–21.38	2H-4, 41–2H-5, 41	17.41–18.91	19.31–20.81
T *Gephyrocapsa* spp. >5.5 µm	3H-4, 60–3H-5, 62	22.30–23.82	23.95–25.47	3H-1, 88–3H-2, 54	22.88–24.04	24.53–25.69
B *Gephyrocapsa* spp. >5.5 µm	3H-CC–4H-1, 66	27.27–27.36	28.92–30.36	3H-3, 54–3H-4, 54	25.54–27.04	27.19–28.69
T *Calcidiscus macintyrei*	4H-1, 66–4H-2, 60	27.36–28.80	30.36–31.80	3H-5, 62–3H-6, 62	28.62–30.12	30.27–31.77
B *Gephyrocapsa oceanica* s.l.	4H-4, 60–4H-5, 60	31.80–33.30	34.80–36.30	3H-CC–4H-1, 51	31.74–32.01	33.39–36.36
T *Discoaster brouweri*	5H-1, 60–5H-2, 55	36.80–38.25	40.60–42.05	4H-5, 50–4H-5, 65	38.00–38.25	42.35–42.60
T *Discoaster surculus*	6H-1, 70–6H-2, 68	46.40–47.88	52.15–53.63	5H-CC–6H-1, 20	51.08–50.70	55.48–56.20
T *Discoaster tamalis*	6H-3, 73–6H-4, 66	49.43–50.86	55.18–56.61	6H-1, 20–6H-1, 65	50.70–51.15	56.20–56.65
T *Sphenolithus* spp.	8H-2, 59–8H-3, 72	66.79–68.42	75.79–77.42	7H-CC–8H-1, 60	70.11–70.10	76.66–77.85
T *Reticulofenestra pseudoumbilicus*	8H-4, 70–8H-5, 61	69.90–71.31	78.90–80.31	8H-2, 80–8H-2, 100	71.80–72.00	79.55–79.75
T *Ceratolithus acutus*				11X-CC–12X-1, 70	106.90–108.20	114.65–115.95
B *Ceratolithus rugosus*				12X-1, 70–12X-2, 60	108.20–109.60	115.95–117.35
B *Ceratolithus acutus*				13X-3, 25–13X-3, 60	120.35–120.70	128.10–128.45
T *Discoaster quinqueramus*				14X-CC–15X-1, 35	136.38–136.75	144.13–144.50
T *Coccolithus miopelagicus*				37X-1, 60–37X-2, 61	348.10–349.61	355.85–357.36

T = top occurrence; B = bottom occurrence.

on the co-occurrence of *R. praebergonii* and *T. convexa* stratigraphically above the last occurrence of *N. jouseae*. Sample 138-850A-6H-CC and Samples 138-850B-6H-CC and -7H-1, 78 cm, were placed in Subzone A of the *R. praebergonii* Zone on the basis of the co-occurrences of *T. convexa, N. jouseae,* and *R. praebergonii*.

The *Nitzschia jouseae* Zone is defined as the stratigraphic interval from the first occurrence of *R. praebergonii* to the first occurrence of *N. jouseae*. Samples 138-850A-7H-3, 62 cm, through -8H-CC (base of Hole 850A) and -850B-7H-2, 70 cm, through -11H-CC were assigned to this zone. Stratigraphic events observed in this interval include (1) the first occurrence of *T. convexa* var. *convexa* (Samples 138-850B-7H-CC through -8H-CC), (2) the first occurrence of *Asteromphalus elegans* (Samples 850B-8H-CC through -9H-CC), (3) and the last occurrence of *Nitzschia cylindrica* (Samples 138-850B-10H-CC through -11H-CC).

Samples 138-850B-12X-CC through -16H-5, 60 cm, represent Subzone C of the *T. convexa* Zone, which has been defined as the interval between the first occurrence of *N. jouseae* and the last occurrence of *T. miocenica*. This interval contains few to common specimens of *N. cylindrica, T. convexa* var. *aspinosa*, and common to abundant specimens of *Thalssiosthrix longissima*. Unlike at other sites, *T. miocenica* has a consistent first occurrence and allows precise placement of the Subzone C/B boundary between Samples 850B-16H, 60 cm, and -16H, 60 cm. Samples 16H-5, 60 cm, through -19H-2, 80 cm, are placed in Subzone B of the *T. convexa* zone based on the occurrence of *T. miocenica* stratigraphically above the last occurrence of *T. praeconvexa*. The last occurrence of *N. miocenica* occurs in this subzone between Samples 138-850B-17H-CC and -18H-3, 51 cm. Samples 138-850B-19H-3, 80 cm, through -21H-CC were assigned to Subzone A of the *T. convexa* Zone, based on the co-occurrences of *T. miocenica, T. convexa,* and *T. praeconvexa*. The base of the *T. convexa* Zone was placed between Samples 138-850B-21X-CC and -22-CC at the first occurrence of *T. miocenica* and *T. convexa*.

The *Nitzschia miocenica* Zone represents the interval from the first occurrences of *T. miocenica* and *T. convexa* to the first occurrence of *N. miocenica*. This zone has been subdivided into two subzones based on the first occurrence of *T. praeconvexa*. Sample 138-850B-22X-CC was assigned to Subzone B, and Samples 138-850B-23X-2, 60 cm, through -26H-1, 61 cm, were placed in Subzone A. The *N. miocenica/N. porteri* boundary was placed between Samples 138-850B-26X-1, 61 cm, and -26X-3, 58 cm.

The occurrences of *N. porteri, N. cylindrica,* and *Rossiella paleacea* below the first occurrence of *N. miocenica* and above the last occurrence of the *T. yabei* Group permits Samples 138-850B-26X-3, 58 cm, through -28X-1, 75 cm, to be assigned to the *N. porteri* Zone. The occurrence of *Thalassiosira burckliana* in Sample 138-850B-27X-CC allows us to place the Subzone A/Subzone B boundary tentatively between Samples 138-850B-27X-7, 20 cm, and -27X-CC. Unfortunately, *T. burckliana* is scattered in Hole 850B.

Samples 138-850B-28X-3, 23 cm, through -32X-CC were placed in the *Thalassiosira yabei* Zone. This zonal placement has been based on the occurrence of *T. yabei* above the last occurrence of *Denticulopsis hustedtii*. *Thalassiosira burckliana* occurs in the uppermost portion of this interval (Sections 138-850B-28X-3 through -30X-CC), indicating that this interval is equivalent to Subzone B of the *T. yabei* Zone. The exact placement of the Subzone B/Subzone A boundary cannot be determined. Samples 138-850B-31X-CC through -32X-CC were assigned to Subzone A.

The *T. yabei/A. moronensis* boundary is defined by the last occurrence of *A. moronensis*. Unlike other Leg 138 sites, at Site 850 *A. moronensis* was observed stratigraphically above the last occurrence of *D. hustedtii*, suggesting that Sample 138-850B-33H-1, 70 cm, approximates the uppermost portion of the *A. moronensis* Zone. However, *A. moronensis* is scattered and thus prevents the precise stratigraphic placement of this boundary. The *T. yabei/A. moronensis* boundary was tentatively placed between Samples 138-850B-32X-CC and -33H-1, 70 cm. Samples 138-850B-33X-1, 70 cm, through -39X-CC were assigned to the *A. moronensis* Zone.

Samples in Cores 138-850B-40X through -41X were assigned to the *Crasepedodiscus coscinodiscus* Zone. Species characteristic of this interval include *Crasepedodiscus coscinodiscus, R. paleacea, Hemidiscus cuneiformis, D. hustedtii, Coscinodiscus gigas* var. *diorama,* and *T. yabei*. Diatoms were not observed in samples examined from Core 138-850B-42X.

PALEOMAGNETISM

Procedures

We performed pass-through paleomagnetic measurements on all APC cores obtained at Site 850 (8 cores from Holes 850A and 10 cores from Hole 850B). Both natural remanent magnetization (NRM) and remanence were measured after applying 15 mT demagnetization to the cores from Hole 850A. We measured remanence only after 15 mT demagnetization for cores from Hole 850B. All pass-through magnetometer measurements were taken at 10-cm intervals in Hole 850A and at 5-cm intervals in Hole 850B. No measurements of discrete samples were conducted on board ship; however, samples were taken in the APC-cored part of the section for later shore-based study. Automated susceptibility measurement was conducted rou-

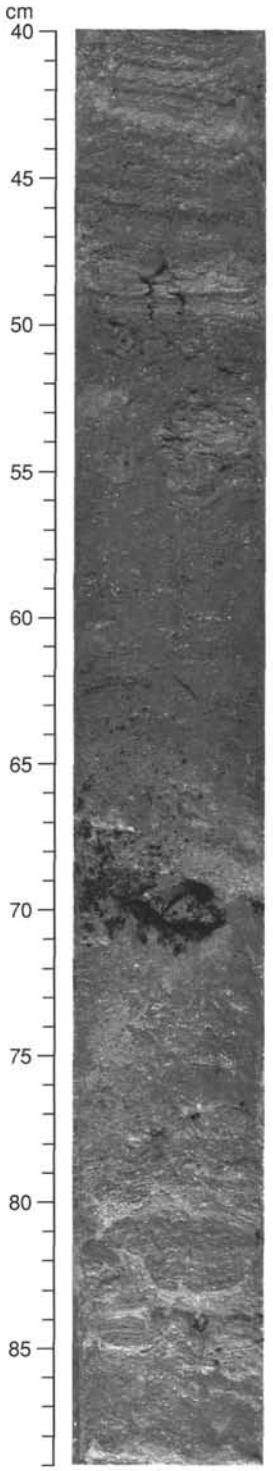

Figure 11. Chert within a nannofossil diatom ooze interval in Section 138-850B-36X-4 at 40–89 cm.

tinely at 5-cm intervals in conjunction with other measurements of the multisensor track.

Results

Paleomagnetic Remanence

Remanence intensities are generally low (about 0.1 mA/m), and remanence directions are scattered, with two significant exceptions. The topmost 3 m of sediment in Hole 850A has stronger remanence and more consistent direction than sediments below. This change corresponds to the brown-to-green transition in sediment color (see "Lithostratigraphy" section, this chapter), which presumably reflects a change in the oxidation state of the sediments.

Lower in the section, the interval between 55 and 69 mbsf has a relatively strong remanence of about 3 mA/m (Fig. 20, left). The transitions into and out of the more weakly magnetized intervals above and below this more highly magnetized zone are abrupt and were not accompanied by any obvious lithologic change or variation in sediment color. This distinctly magnetized zone (DMZ) is also expressed in the low-field susceptibility record (Fig. 20, right); however, susceptibility shows a more gradual evolution between low and high values and thus does not clearly define the boundaries of the DMZ.

Remanence directions within the DMZ appear extremely stable in the sense that they show good serial correlation, near-zero inclinations (as are appropriate for the site latitude of 1°N), and full 180° declination swings at polarity zone boundaries. We assigned polarity sense to the polarity zonation obtained (Figs. 21 and 22) using the multishot results (Table 7). These orientation camera results clearly define the polarity sense for Cores 138-850A-6H, -7H, -8H, and -850B-7H, where oriented directions fall within 20° of the north-south axis. However, multishot orientation for Core 138-850B-6H is ambiguous in that oriented declinations lie at nearly 90° and 270°. We have interpreted polarity sense in this core simply by matching the reversal pattern with the corresponding interval in Hole 850A.

Discussion

Assignment of the polarity record to the magnetic polarity time scale (Fig. 23, Table 8) builds on the general biostratigraphic framework established for this site (see "Biostratigraphy" section, this chapter). For example, the location of the CN11/12 boundary in Cores 138-850A-8H and -850B-8H indicates that these sediments are somewhat younger than upper Gilbert. Given such constraints, the only reasonable assignment of this middle to late Pliocene interval is to the Gauss. Indeed, the relative spacing of the five reversal boundaries matches our expectations for the ages of the onset of the Gauss and the boundaries of the Mammoth and Kaena subchrons (Fig. 23), given the guiding assumption of uniform sedimentation rates within this zone.

The mechanisms that control the preservation of a paleomagnetic signal at this site are particularly intriguing. Although the downcore loss of signal at the brown-to-green transition may correspond to our general notion of magnetite dissolution by reduction diagenesis, the factors controlling the preservation of the magnetic carrier within the DMZ, the cause of the abrupt onset of preservation, and the sudden loss of preservation, all remain unclear. Sedimentation rates within the DMZ do not appear anomalous, and the usual color indicators of redox conditions do not vary through this interval. The results of geochemical logging suggest that this zone may be somewhat enriched in clays (see "Downhole Measurements" section, this chapter); however, this enrichment is quite minor and no indication of enhanced clay content is seen in smear-slide analysis (see "Lithostratigraphy" section, this chapter).

Low-Field Initial Susceptibility

The susceptibility profile of Site 850 sediments is flat, with values generally within $\pm 1 \times 10^{-5}$ SI of zero. However, two zones exist in which susceptibility is higher (Fig. 24). One of these, the DMZ, has been discussed. The other falls roughly in the interval between 290 and 400 mbsf. Sediments in this interval are relatively rich in radiolarians and slightly grayer than the overlying units (see "Lithostratigraphy" section, this chapter). The decreased diatom abundance in this interval may indicate a period of somewhat lower productivity and suggests that the susceptibility signal might perhaps be controlled by the amount of organic carbon being deposited. This correlation thus matches the general ten-

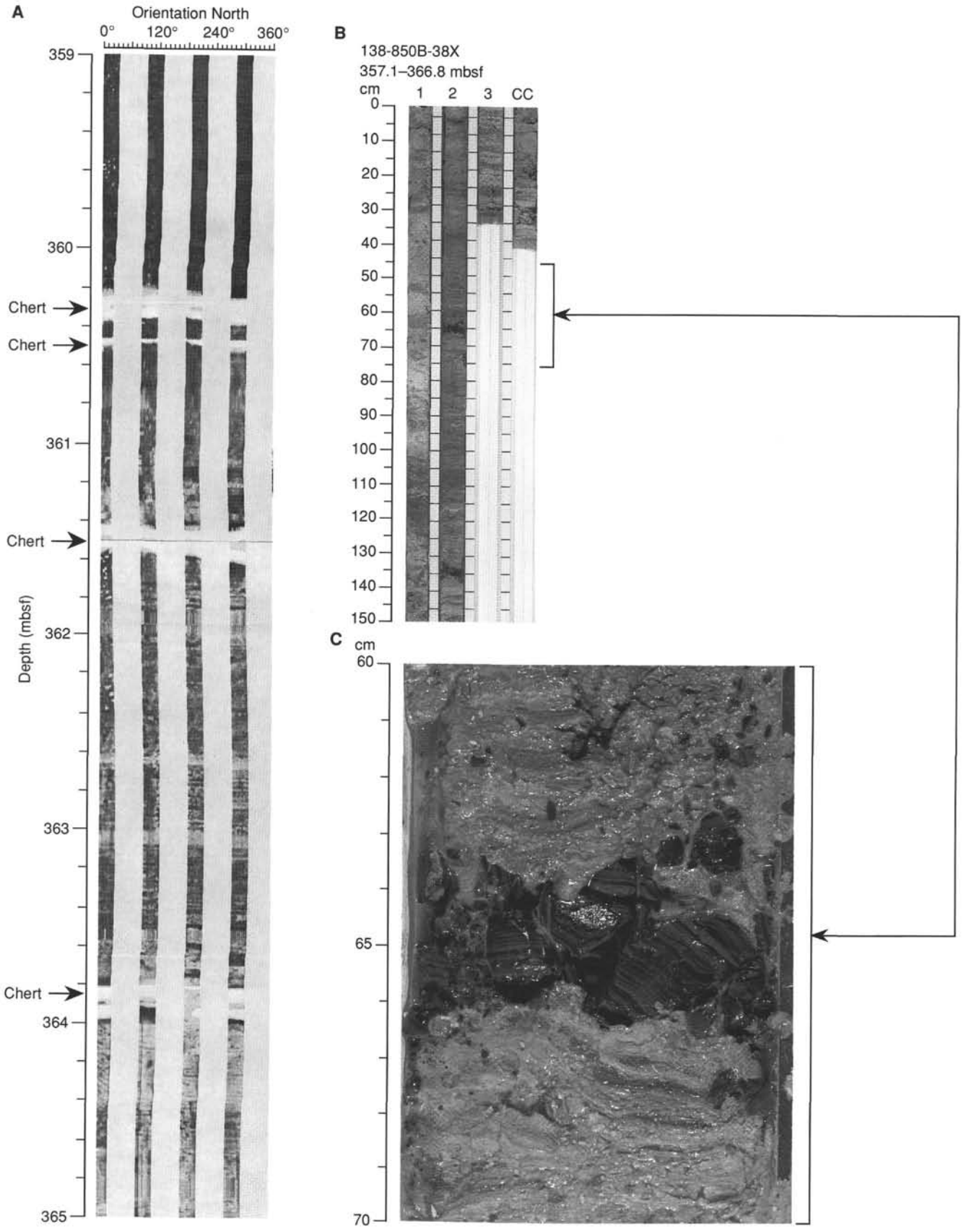

Figure 12. **A.** Formation microscanner log of Hole 850B, showing the high resistivity intervals inferred to correspond to the cherts in Core 138-850B-38X. **B.** Core 138-850B-38X. Chert layers are located at Section 2, 65–66 and 133–135 cm. **C.** Laminated chert within laminated nannofossil diatom ooze (Core 138-850B-38X at 60–70 cm).

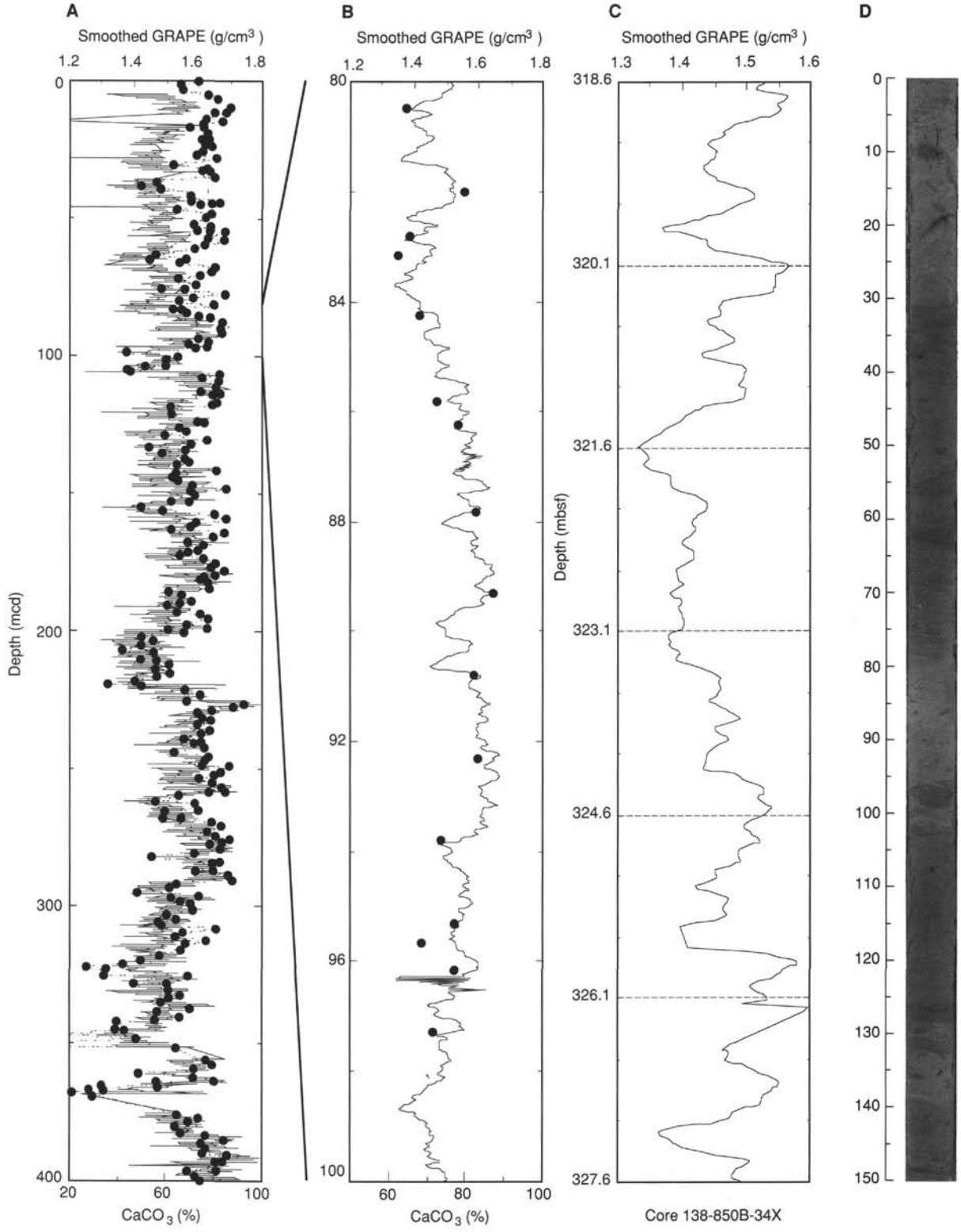

Figure 13. **A.** Smoothed GRAPE density (solid line) and calcium carbonate content (dashed line with symbol) of Hole 850B sediments. **B.** Smoothed GRAPE density (solid line) and carbonate content (dots) of sediments from 80 to 100 mcd in Hole 850B. **C.** Smoothed GRAPE density of Core 138-850B-34X. Only the first six sections of the core have been plotted. Dotted lines indicate section boundaries. **D.** Section 138-850B-34X-2. Note the correspondence between sediment color and density of sediments.

Table 4. Sample and depth constraints of planktonic foraminifer events for Site 850.

Event	Hole 850B		
	Interval	Depth (mbsf)	Depth (mcd)
T *Globorotalia limbata*	3H-CC–4H-CC	27.27–36.83	28.92–39.83
T *Dentoglobigerina altispira*	5H-CC–6H-CC	46.21–55.81	50.01–61.56
T *Sphaeroidinellopsis* spp.	5H-CC–6H-CC	46.21–55.81	50.01–61.56
B *Globorotalia tumida*	14X-CC–15X-CC	136.38–146.05	144.13–153.80
B *Globorotalia plesiotumida*	28X-CC–29X-CC	270.26–279.93	278.01–287.68

T = top occurrence; B = bottom occurrence.

Table 5. Sample and depth constraints of radiolarian events for Site 850.

Event	Hole 850A			Hole 850B		
	Interval	Depth (mbsf)	Depth (mcd)	Interval	Depth (mbsf)	Depth (mcd)
B *Buccinosphaera invaginata*						
T *Stylatractus universus*				1H-4–1H-6	8.60–11.60	8.60–11.60
B *Collosphaera tuberosa*				1H-4–1H-6	8.60–11.60	8.60–11.60
T *Lamprocyrtis neoheteroporus*				2H-CC–3H-2	22.15–24.60	24.05–26.25
T *Anthocyrtidium angulare*				2H-4–2H-6	18.10–21.10	19.69–22.69
T *Theocorythium vetulum*				2H-CC–3H-2	22.15–24.60	24.05–26.25
B *Lamprocyrtis nigriniae*				2H-CC–2H-2	22.15–24.60	24.05–26.25
B *Theocorythium trachelium*				3H-4–3H-6	27.60–30.60	32.26–33.39
B *Pterocorys minythorax*				3H-6–3H-CC	30.60–31.74	32.26–33.39
B *Anthocyrtidium angulare*				3H-CC–4H-2	31.74–34.10	33.39–37.14
T *Pterocanium prismatium*				3H-CC–4H-2	31.74–34.10	33.39–37.14
T *Lamprocyrtis heteroporos*				2H-CC–3H-2	22.15–24.60	24.05–26.25
T *Anthocyrtidium jenghisi*				5H-4–5H-6	46.60–49.60	50.41–53.41
B *Theocalyptra davisiana*				5H-6–5H-CC	49.60–51.08	53.41–55.5
T *Stichocorys peregrina*				5H-CC–6H-2	51.08–53.60	55.50–58.89
T *Anthocyrtidium pliocenica*				6H-6–6H-CC	59.60–60.60	64.89–66.10
B *Lamprocyrtis neoheteroporos*	6H-CC–7H-CC	55.81–65.22	61.56–72.57	6H-2–6H-6	53.60–59.60	61.60–64.89
B *Lamprocyrtis heteroporos*				6H-6–6H-CC	59.60–60.60	64.89–66.10
T *Phormostichoartus fistula*				6H-6–6H-CC	59.60–60.60	64.89–66.10
T *Lychnodictyum audax*				7H-CC–8H-2	70.11–72.10	76.68–81.14
T *Spongaster pentas*	7H-CC–8H-CC	65.22–74.76	72.57–83.76	8H-2–8H-4	72.10–75.10	81.14–83.80
T *Phormostichoartus doliolum*	7H-CC–8H-CC	65.22–74.76	72.57–83.76	8H-2–8H-4	72.10–75.10	81.14–83.80
B *Amphirhopalum ypsilon*	7H-CC–8H-CC	65.22–74.76	72.57–83.76	8H-2–8H-4	72.10–75.10	81.14–83.80
B *Spongaster tetras*				9H-CC–10H-2	89.08–91.10	96.83–98.85
T *Didymocyrtis penultima*				8H-CC–9H-2	79.59–81.60	87.34–88.35
B *Pterocanium prismatium*				11X-2–11X-4	100.60–103.60	107.35–110.35
T *Spongaster berminghami*				12X-CC–13X-2	117–119.70	127.48–130.48
B *Spongaster pentas*				12X-CC–13X-2	117–119.70	124.75–127.48
T *Solenosphaera omnitubus*				13X-6–13X-CC	125.70–126.74	133.47–134.49
T *Siphostichartus corona*				15X-6–15X-CC	145–146.05	152.75–153.80
T *Acrobotrys tritubus*				22X-4–22X-CC	208.70–212.83	216.45–220.58
T *Stichocorys johnsoni*				19X-6–19X-CC	182.80–183.95	190.55–191.70
Stichocorys delmontensis > *S. peregrina*				22X-CC–23X-2	212.83–215.40	220.58–223.15
T *Calocycletta caepa*				19X-6–19X-CC	182.80–183.95	190.55–191.70
B *Solenosphaera omnitubus*				24X-CC–25X-2	231.95–234.70	239.70–242.45
T *Diartus hughesi*				27X-2–27X-4	253.60–256.60	261.35–264.35
B *Acrobotrys tritubus*				25X-2–25X-CC	234.70–241.73	242.45–249.48
B *Spongaster berminghami*				30X-4–30X-CC	285–289.57	292.25–297.32
T *Stichocorys wolffii*				31X-CC–32X-2	299.34–301.80	307.09–308.55
T *Botryostrobus miralestensis*				29X-6–29X-CC	278.90–279.93	286.65–287.68
T *Diartus pettersoni*				29X-CC–30X-2	279.93–282.50	287.68–290.25
B *Lithopera bacca*				37X-6–37X-CC	356.10–357.20	362.85–365.03
Diartus pettersoni >*D. hughesi*				30X-CC–31X-2	289.57–292.20	297.32–299.95
B *Diartus hughesi*				31X-2–31X-4	292.20–295.20	299.95–302.95
T *Cyrtocapsella japonica*				35X-2–35X-4	330.80–333.80	338.55–341.55
T *Lithopera thornburgi*				32X-6–33X-CC	304.80–318.75	314.55–326.50
T *Carpocanium cristata*				37X-CC–38X-1	357.20–358.37	365.03–366.12

T = top occurrence; B = bottom occurrence; > = evolutionary transition.

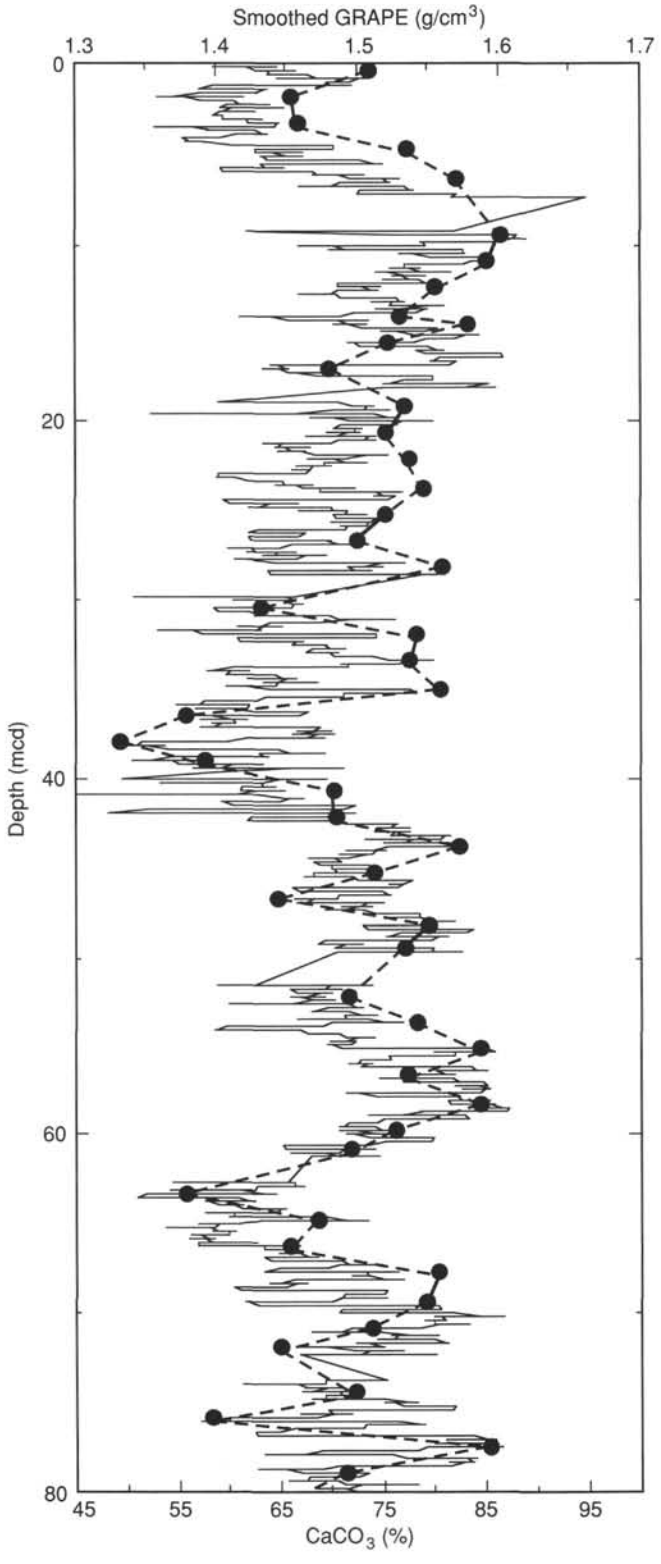

Figure 14. Smoothed GRAPE density (solid line) and calcium carbonate content (dashed line with filled circle) of Hole 850A, 0–80 mcd.

dency seen at this and other western transect sites for diatom abundance and susceptibility to be inversely related.

SEDIMENTATION RATES

A sedimentary section just 400 m thick, covering the time interval from the late Pleistocene to the bottom of the late Miocene, was recovered at Site 850. Biostratigraphic age control was provided by all four of the chief planktonic microfossil groups.

The composite depth section for Site 850 is given in Table 9. This composite was formed by comparing shipboard measurements of GRAPE density, magnetic susceptibility, and percent reflectance (from the automated color analyzer) at adjacent holes. These comparisons were then integrated to form a single composite depth section for the site (a detailed discussion on the construction of composite sections during Leg 138 is presented in Hagelberg et al., this volume).

For the holes and cores listed in Column 1 of Table 9, Column 2 gives the ODP sub-bottom depth of each core's top and bottom (in meters below seafloor, or mbsf). Note that the depth given in Column 2 corresponds to the depth of the bottom of the recovered core. This depth places the core catchers in their correct position in the composite depth section and is not the same as the standard ODP core-catcher depth. Column 3 shows the length of core recovered. Column 4 gives the composite depth of each core's top and bottom (in meters composite depth, or mcd). Column 5 indicates the amount of offset between the ODP depth and the composite depth. ODP sub-bottom depths were converted to composite depths by adding the offset listed in Column 5 for a given core.

GRAPE density and percent reflectance data both produced records with high amplitudes and variability through much of the section in Holes 850A (8 cores) and 850B (42 cores) at Site 850 (Fig. 25, back pocket). Magnetic susceptibility data were of low amplitude through much of the sequence and were not as useful a correlation tool as at previous sites. Because of time constraints for drilling this site, only the upper 74 m was cored twice to provide an overlapping section. The composite section formed from Holes 850A (Cores 1–8) and 850B (Cores 1–8) indicates that overlapping of adjacent holes was maintained through 87 mcd, the entire interval that had been double-cored.

Developing a satisfactory sedimentation rate record for Site 850 was assisted by a good paleomagnetic record for part of the Pliocene. In addition, all four microfossil groups provided good biostratigraphic information in different parts of the record. Table 10 gives the control points selected to generate the age-vs.-depth plots shown in Figures 26A through 26D. In the Pliocene–Pleistocene section, nannofossil control points were used to supplement the reversal boundaries, which are well determined for the Gauss Chron and the Kaena and Mammoth within it. In the late Miocene section, nannofossils were less useful and diatom datums were used almost exclusively. The sedimentation rate pattern shows that the sediment accumulated at a rather uniform rate of a little more than 20 m/m.y. over most of the Pliocene–Pleistocene, but that this rate was much higher, approaching 100 m/m.y., in the earliest Pliocene and in part of the latest late Miocene (Figs. 27 and 28).

INORGANIC GEOCHEMISTRY

Results of Pore-Water Studies at Site 850

Seventeen interstitial-water samples were collected at Site 850, one from Hole 850A at 1.5 mbsf and sixteen from Hole 850B that ranged in depth from 31.0 mbsf to just above basement at 398.8 mbsf

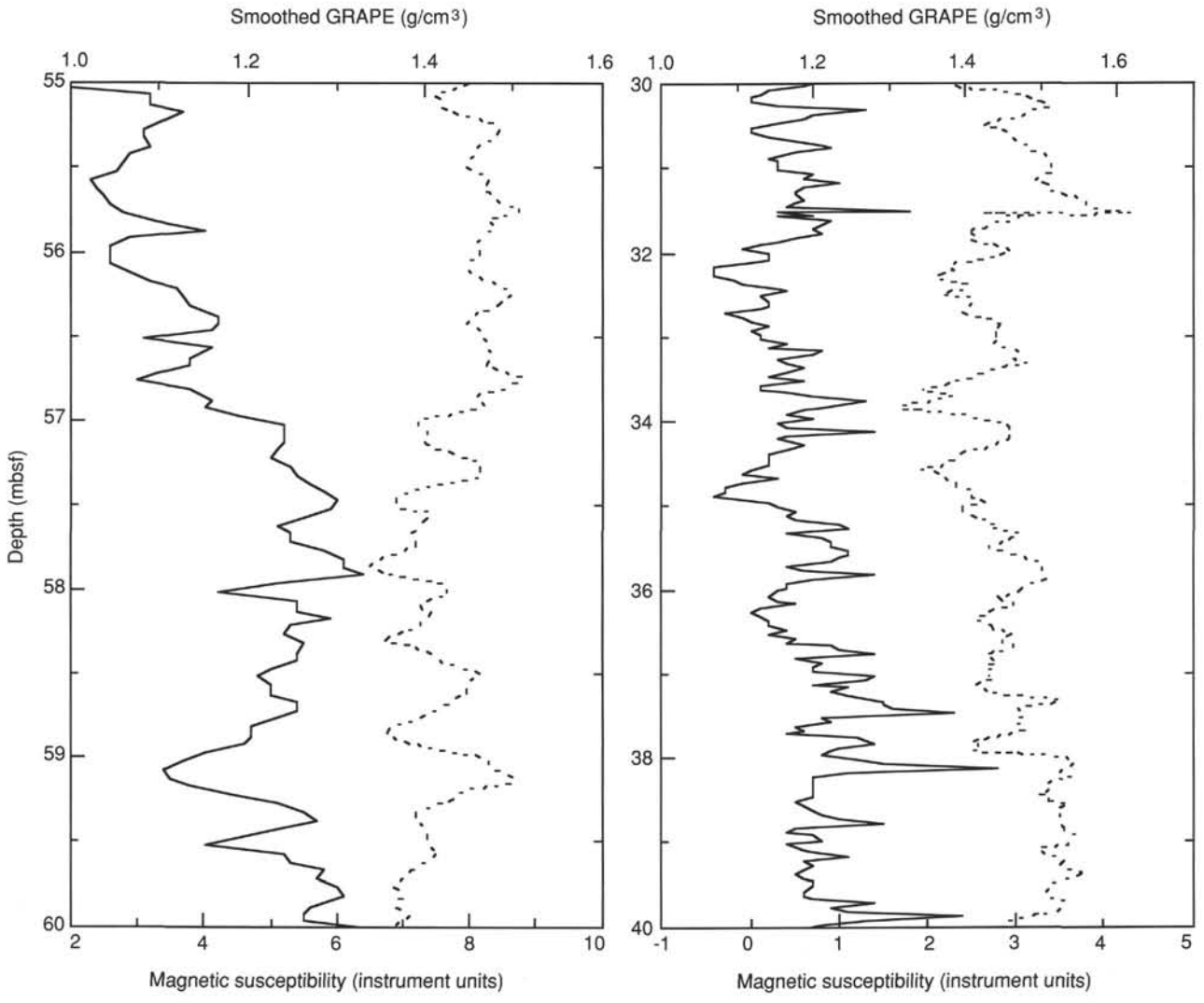

Figure 15. **A.** Magnetic susceptibility (solid line) and smoothed GRAPE density data (dashed line) from 55–60 mbsf, Hole 850A. **B.** Magnetic susceptibility (solid line) and smoothed GRAPE density data (dashed line) from 30–40 mbsf, Hole 850A.

(Table 11). Results from these two holes are considered here to constitute a single depth.

Core 138-850A-1H consists of diatom foraminifer radiolarian nannofossil ooze (see "Lithostratigraphy" section, this chapter). Interstitial-water sampling in Hole 850B began with a sample from the third core (Section 138-850B-3H-6), composed of white foraminifer radiolarian nannofossil ooze. Beginning with this core, one interstitial-water sample was taken from every third core through Core 138-850B-39X. The sediments in these upper sections consist of variations of nannofossil ooze. Beginning with Core 138-850B-40X, one interstitial-water sample was taken from every core to basement.

A lithology change occurs below Core 138-850B-36X, where the sediments shift from nannofossil ooze to diatom nannofossil ooze (see "Lithostratigraphy" section, this chapter). This change in the dominant lithology was accompanied by the occurrence of three layers of finely laminated chert. The top layer is found in Section 138-850B-36X-4; chert also occurs as two distinct layers in Sections 138-850B-38X-2 and again as discrete fragments in the top of Section 138-850B-41X-1. The last four interstitial-water samples were taken from below these chert layers. Irregular offsets can be seen in some of the pore-water profiles across these chert layers (Figs. 29, 30, and 31). This irregularity is reminiscent of the offset at Site 849. The abrupt change in diffusive exchange below 350 mbsf also is apparent in the profile of methane for this site (see "Organic Geochemistry" section, this chapter).

Below these chert layers, diatom nannofossil ooze continues to be the dominant lithology to near the bottom of the hole. Sediments in the last core (138-850B-42X) grade gradually into pale yellow radiolarian diatom nannofossil ooze, which contains manganese dendrites and hematite (see "Lithostratigraphy" section, this chapter).

A faint smell of H_2S may have existed during the coring of Hole 850B. Certainly the smell of H_2S was much less pronounced than at the previous site.

The chemistry of interstitial water at Site 850 (Table 11) is influenced by crystallization and diagenesis; alteration of crust seems to be less important here than at some other Leg 138 sites. Concentration-vs.-depth profiles from this site (Figs. 29, 30, and 31) are subtly different from those developed for Site 849. Because Sites 849 and 850 are near each other and have similar depositional histories, it is interesting to compare their pore-water chemistries, as has been done in Figures 32 and 33.

Concentrations of sodium (Fig. 29A) and chloride (Fig. 29B) do not change downcore or across the chert layers. These monotonous

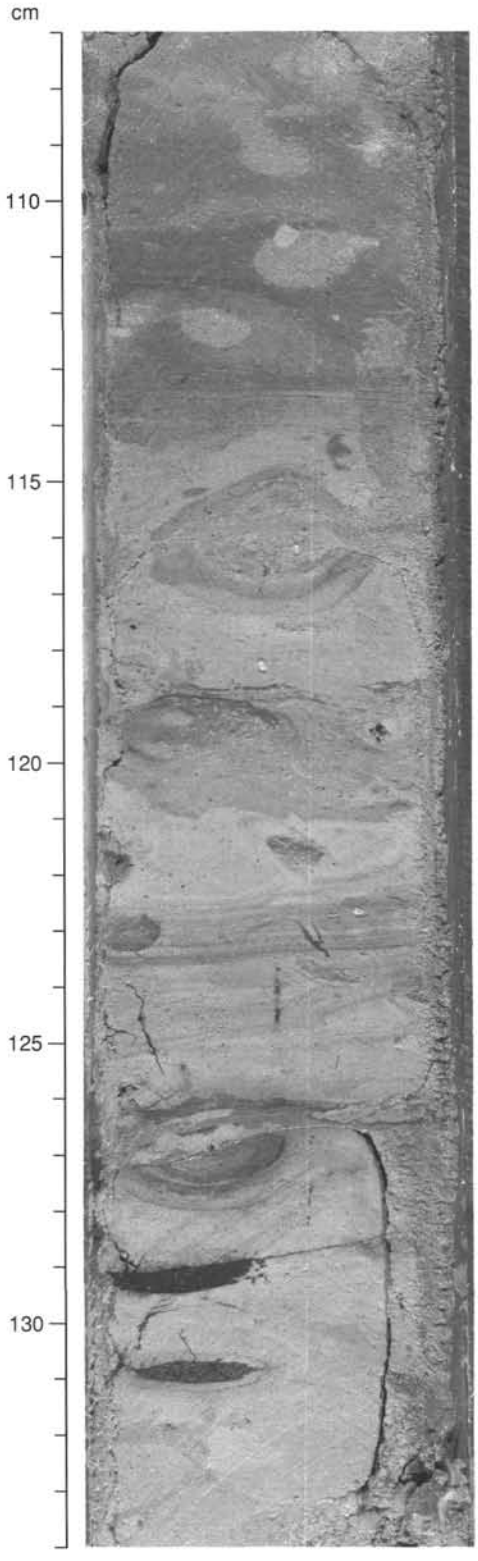

Figure 16. A wide variety of trace fossils can be seen on this saw-cut surface (Core 138-850B-41X-2, 107–134 cm), including *Planolites,* solid burrows, rind burrows, *Chondrites,* and some black burrows filled with pyrite.

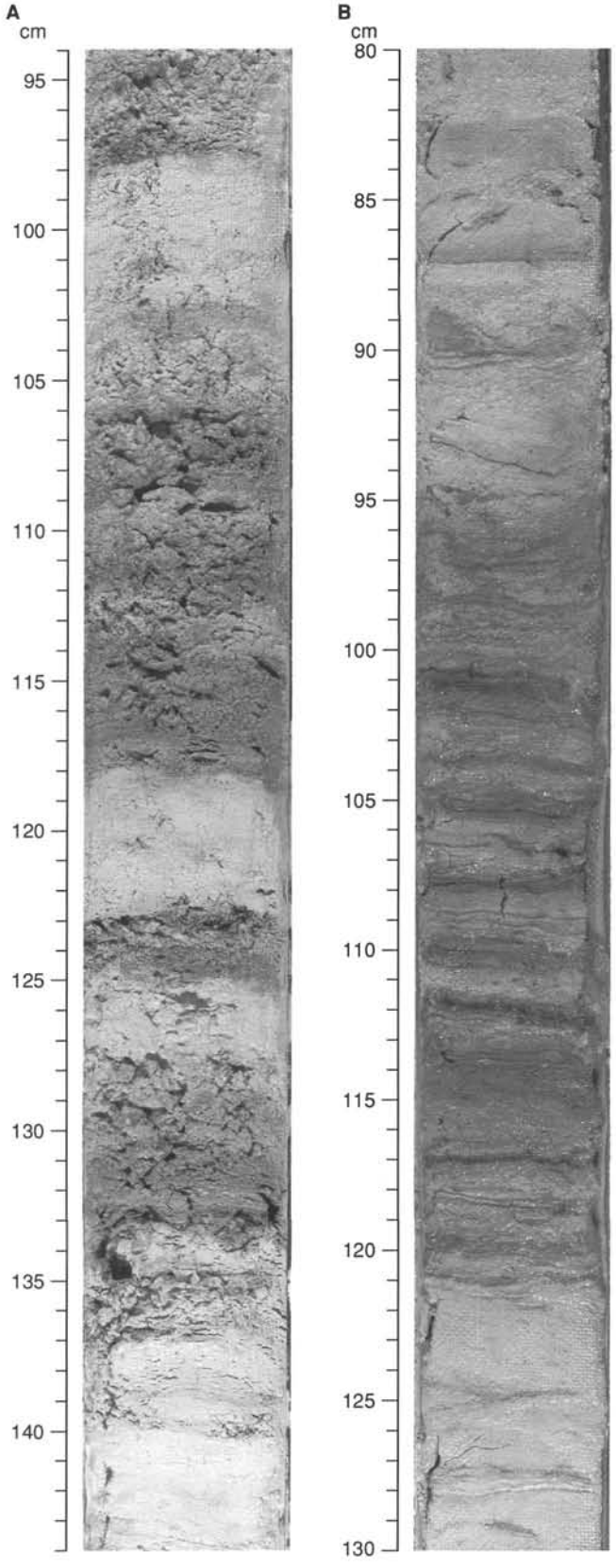

Figure 17. Contrast in lamination visible on the roughened, wire-cut core (138-850B-21X-5, 94–144 cm) (**A**) and lamination visible on the saw-cut surface (138-850B-36X-3, 80–130 cm) (**B**).

Table 6. Sample and depth constraints of diatom events for Site 850.

Event	Hole 850A			Hole 850B		
	Interval	Depth (mbsf)	Depth (mcd)	Interval	Depth (mbsf)	Depth (mcd)
T *Nitzschia reinholdii*	1H-CC–2H-CC	7.68–16.74	7.68–18.29	1H-2–1H-CC	5.30–12.78	5.30–12.78
T *Nitzschia fossils*	1H-CC–2H-CC	7.68–16.74	7.68–18.29	1H-CC–2H-CC	12.78–22.15	14.68–24.05
T *Rhizosolenia praebergonii*	4H-3–4H-4	30.30–31.80	33.30–34.80	4H-1–4H-2	32.20–33.7	36.55–38.05
B *Pseudeunotia doliolus*	5H-2–5H-5	38.30–42.80	42.10–46.60	4H-4–4H-6	35.70–38	40.01–42.40
T *Thalassiosira convexa*	5H-6–5H-7	44.35–45.55	48.15–49.35	5H-2–5H-3	43.20–44.70	47.6–49.10
T *Nitzschia jouseae*	5H-CC–6H-CC	46.21–55.81	50.01–61.56	5H-CC–6H-2	51.08–52.80	56.58–58.30
B *Rhizosolenia praebergonii*	6H-CC–7H-CC	55.81–65.22	61.56–72.57	7H-1–7H-2	60.70–62.20	67.25–68.75
F *Thalassiosira convexa var. convexa*	7H-4–7H-CC	60.31–67.66	67.66–72.57	8H-2–8H-CC	71.80–79.59	79.55–87.34
B *Actinocyclus elegans*	7H-CC–8H-CC	65.22–74.76	72.57–83.76			
T *Nitzschia cylindrica*				10H-CC–11X-CC	98.49–106.90	106.24–114.65
B *Nitzschia jouseae*				11X-CC–12X-CC	106.90–117	114.65–124.75
T *Thalassiosira miocenica*				16X-4–16X-5	151.20–152.70	158.95–160.45
T *Nitzschia miocenia*				18X-2–18X-3	167.02–168.51	174.77–176.26
T *Thalassiosira praeconvexa*				19X-2–19X-3	176.50–178.00	184.25–185.75
B *Thalassiosira miocenica*				21X-CC–22X-3	203.15–206.90	210.90–214.65
B *Thalassiosira convexa var. aspinosa*				21X-CC–22X-3	203.15–206.90	210.90–214.65
B *Thalassiosira praeconvexa*				22X-CC–23X-2	212.83–214.90	220.55–222.65
B *Nitzschia miocenica*				26X-1–26X-2	242.40–243.88	250.15–251.63
T *Rhizosolenia paleacea*				26X-2–26X-3	243.90–245.98	251.65–253.73
T *Thalassiosira burckliana*				26X-CC–27X-CC	251.49–260.79	259.24–268.54
T *Actinocyclus ellipticus var. javnicus*				27X-6–27X-7	259.10–260.20	266.87–267.95
B *Nitzschia marina*				27X-7–27X-CC	260.18–260.79	267.95–268.54
B *Nitzschia cylindrica*				28X-1–28X-3	261.54–263.93	269.29–271.68
T *Thalassiosira yabei*				28X-3–28X-CC	269.93–270.26	271.68–278.01
B *Thalassiosira burckliana*				30X-CC–31X-CC	289.57–299.34	297.32–307.09
T *Denticulopsis hustedtii*				32X-4–32X-5	304.50–306.06	312.25–313.81
T *Actinocyclus moronensis*				32X-CC–33X-1	308.22–309.60	315.97–317.35
T *Craspedodiscus coscinodiscus*				40X-2–40X-4	378.45–381.38	386.20–389.13

T = top occurrence; B = bottom occurrence.

distributions indicate that sodium and chloride are not being produced or consumed at this site. Deviations from simple burial can be accommodated within analytical uncertainties.

Profiles of alkalinity (Fig. 29C) and sulfate (Fig. 29D) are best characterized as two distinct zones. Above 350 mbsf, microbial degradation of organic matter consumes sulfate and produces alkalinity (Claypool and Kaplan, 1974), which generates concave-downward and concave-upward profiles for sulfate and alkalinity, respectively. Below 350 mbsf, both parameters return abruptly to levels of seawater.

Even the most reducing interstitial water at Site 850 is only mildly anoxic. Alkalinity in truly reducing sediments (i.e., 0 sulfate) can reach levels that are 10-fold higher than the highest concentration found at this site, such as those sampled by Harrison et al. (1982) at Sites 496 and 497 on the Middle America Trench slope during DSDP Leg 67.

Ammonia displays the greatest change across the 350 mbsf chert boundary (Fig. 31C), decreasing 22-fold across this interval (Table 11). The same phenomenon was observed at Site 849. Clearly, ammonia is being produced by microbial activity above the layer, but is behaving more-or-less conservatively below.

Potassium (Fig. 30C) is statistically invariant downcore. On the other hand, in the upper sections, magnesium (Fig. 30A) and calcium (Fig. 30B) decrease downhole. Such changes occur when alkalinity is produced by microbial activity (Fig. 29C), initiating the precipitation of carbonate phases. The calcium-rich chert layers below 350 mbsf appear relict in this view because these depths are not the focal point of calcium diagenesis at the present time.

Silica displays a regular increase with depth, indicative of reactions with biogenic silica (Kastner, 1981; Gieskes, 1974). A definite change in this trend is seen as decreasing concentrations below the chert boundary (Fig. 30D). Silica concentrations below 350 mbsf decrease into basement; however, there is no dramatic change within the chert zone. The absence of an associated chemical signature in the present-day pore water supports the view that these chert layers are relict.

The strontium profile at this site (Fig. 31B) is similar to that for nearby Site 572, as reported by Stout (1986). The increasing trend of strontium with depth observed at these and many other sites is known to be produced by recrystallization of biogenic calcite (Elderfield and Gieskes, 1982; Baker et al., 1982; Gieskes et al., 1986; Baker, 1986). The shape of the concentration-vs.-depth profile of lithium (Fig. 31A and 33D) in the upper sections of this hole suggests that this element is being removed by this same process, which is consistent with profiles of interstitial lithium recorded at other sites during this leg. In general, however, lithium geochemistry in deep-sea sediments apparently is more complex than these observations would imply, as it behaves differently at other DSDP/ODP sites (Gieskes, 1983).

Comparison with Site 849

Subtle differences are seen in the pore-water results from Sites 849 and 850, especially if one looks closely at the chemistry above the chert zone. Figures 32 and 33 are plots of pore water data down through Core 24X for these two sites that have been plotted vs. each other.

Concentrations of sulfate (Fig. 32B) are lower in Site 849 sediments, at some depths. This implies a somewhat greater reductive intensity at Site 849, which is consistent with the olfactory records of H_2S.

A comparison of ammonia levels at these sites (Fig. 32C) reveals some differences, but mainly in the distribution, not in the standing crops of ammonia. Silica (Fig. 32D) levels are somewhat higher at Site 850, which suggests a greater extent of recrystallization in the biogenic silica fraction.

Magnesium (Fig. 33A) and calcium (Fig. 33B) profiles at these two sites are significantly different. Magnesium and calcium decrease higher in the sediment column at Site 849, which is consistent with the decrease in sulfate at shallow depths at this site (Fig. 32B). This response in calcium and magnesium makes sense because bicarbonate is produced when sulfate is consumed during the oxidation of organic matter, thus precipitating diagenetic carbonates. This difference is consistent with a slightly higher organic carbon burial rate at Site 849 relative to Site 850. Moreover, this scenario is in agreement with the fact that alkalinities at these sites are similar (Fig. 32A), because this

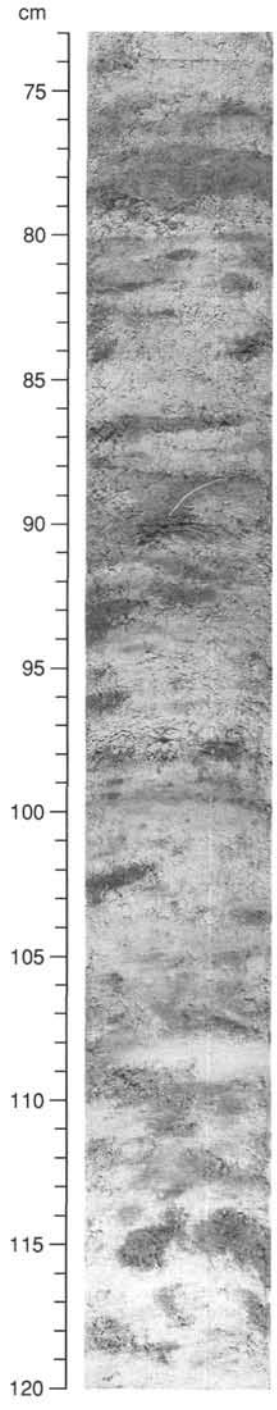

Figure 18. Bioturbated diatom nannofossil ooze having darker, disrupted layers and burrow fills of nannofossil diatom ooze in a zone of alternating laminated and bioturbated diatom-rich sediment (Core 138-850B-10H-2, 73–120 cm).

process should buffer the alkalinity generated during diagenesis. It is also interesting to note that the calcium contents of the laminated cherts at Site 849 are twofold higher than those at Site 850 (based on XRF analyses).

A comparison of strontium (Fig. 33C) to lithium (Fig. 33D) at these nearby sites reveals two things. First, strontium levels at Site 849 are higher throughout much of the sediment column. This situation is indicative of more extensive recrystallization at Site 849, which is the response one would expect from exposure to a more corrosive pore

Table 7. Multishot orientation tool results.

Core	Azimuthal orientation (0°-360°)	Deviation from direction (0°-360°)	Vertical drift (°)
850A-4H	025	346	1.0
5H	125	350	1.6
6H	010	351	1.0
7H	040	336	1.7
8H	122	348	1.7
850B-4H	344	300	3.2
5H	260	305	3.5
[a]6H	(232)	310	3.5
[a]6H	161		
7H	254	303	3.2
8H	080	300	3.2
9H	132	307	3.4
10H	196	312	3.1

For multishot orientation the measured declination is corrected by adding to it the multishot azimuthal orientation and the local geomagnetic deviation (9.0°).

[a]Secondary orientation (SOR) angle is the value used to adjust average measured declination to 0° or 180° for normal or reversed chronozones, respectively, when the multishot orientation is not available or inconsistent. Multishot azimuth values in parentheses are considered to be erroneous, and in the interpretation we use the SOR value in the following line.

fluid maintained by a higher level of diagenetic activity. Second, the difference in dissolved strontium concentrations between these sites is not matched in lithium. This decoupling suggests that, while the diagenetic behavior of strontium and lithium are linked in a general way, substantial differences exist in detail.

The behavior of these parameters below 350 mbsf at Site 850 seems to be unrelated to diagenesis or crystallization. Furthermore, there does not seem to be a classic response to basement as recorded at other locations (McDuff, 1981). The near-basement concentrations seem to be fixed at seawater levels (with the exception of silica), much like what was observed at Site 849.

In summary, the pore-water chemistry at Site 850 is similar to that at nearby Site 849, but some real differences exist. In particular, sulfate reduction is somewhat earlier at Site 849. The slight compression of the diagenetic sequence at Site 849 initiates precipitation of diagenetic carbonates at shallower depths, as apparent in magnesium and calcium profiles. This same process has a buffering effect on alkalinity concentrations, which are similar at the two sites. Enhanced diagenesis at Site 849 relative to Site 850 creates a more corrosive environment that leads to increased levels of biogenic calcite recrystallization, driving dissolved strontium concentrations up and dissolved lithium concentrations down. Below the chert zone, the pore-water concentrations are similar to seawater levels.

Sediment Chemistry

Sediment samples from Site 850 were analyzed by X-ray fluorescence spectroscopy in order to determine the general trends in sediment chemistry. These samples were the sediment scraped from the surface of the archive half of sections to prepare them for color reflectance scanning. We analyzed the sediment scraped from the first section of most cores to provide an average record of the sediment chemistry that has not been aliased by the extensive lithologic variability present throughout the site.

Cores 138-850B-32X through -42X were very firm and were cut by a saw. Their cut surfaces were smooth and did not require scraping. To extend the sediment chemistry analyses to the base of the sedimentary section, we also analyzed one discrete sample from Section 1 of Cores 138-850B-33X through -42X. These samples were chosen to be as representative of the entire section as possible. Fortunately, each of the

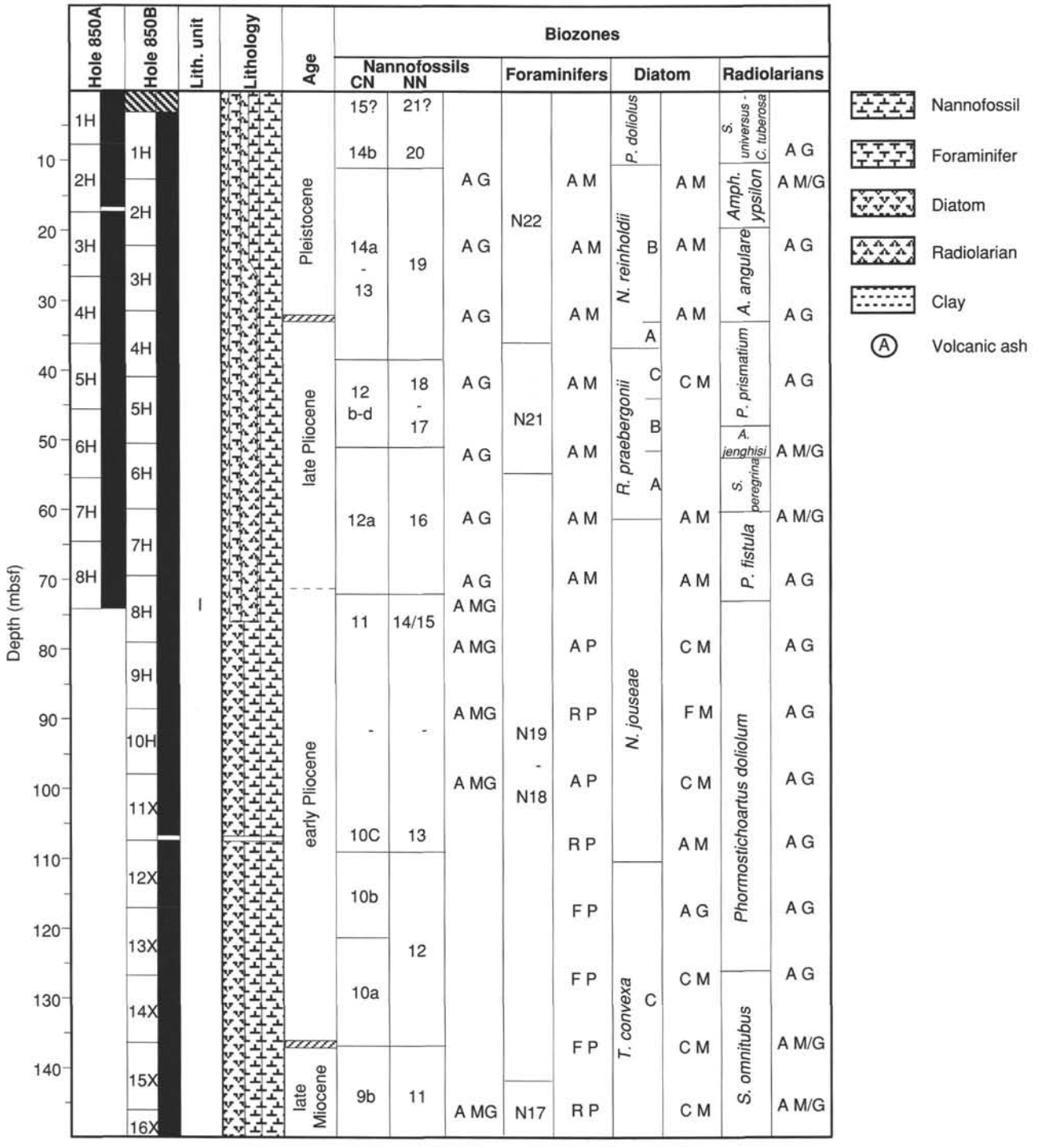

Figure 19. Stratigraphic summary for Site 850. Depth is in meters below seafloor (mbsf). Hatched area represents intervals where specimens of a particular microfossil group are rare or absent, preventing zonal assignment. Dashed lines represent uncertainty in placement of a zonal boundary. Microfossil abundance is recorded as A = abundant; C = common; F = few; R = rare; and B = barren. Microfossil preservation is recorded as G = good; M = moderate; P = poor. This figure presents a general overview of the stratigraphic results at Site 850. Placement of specific stratigraphic boundaries may differ slightly among holes. Data presented in this figure are based on results from Hole 850B.

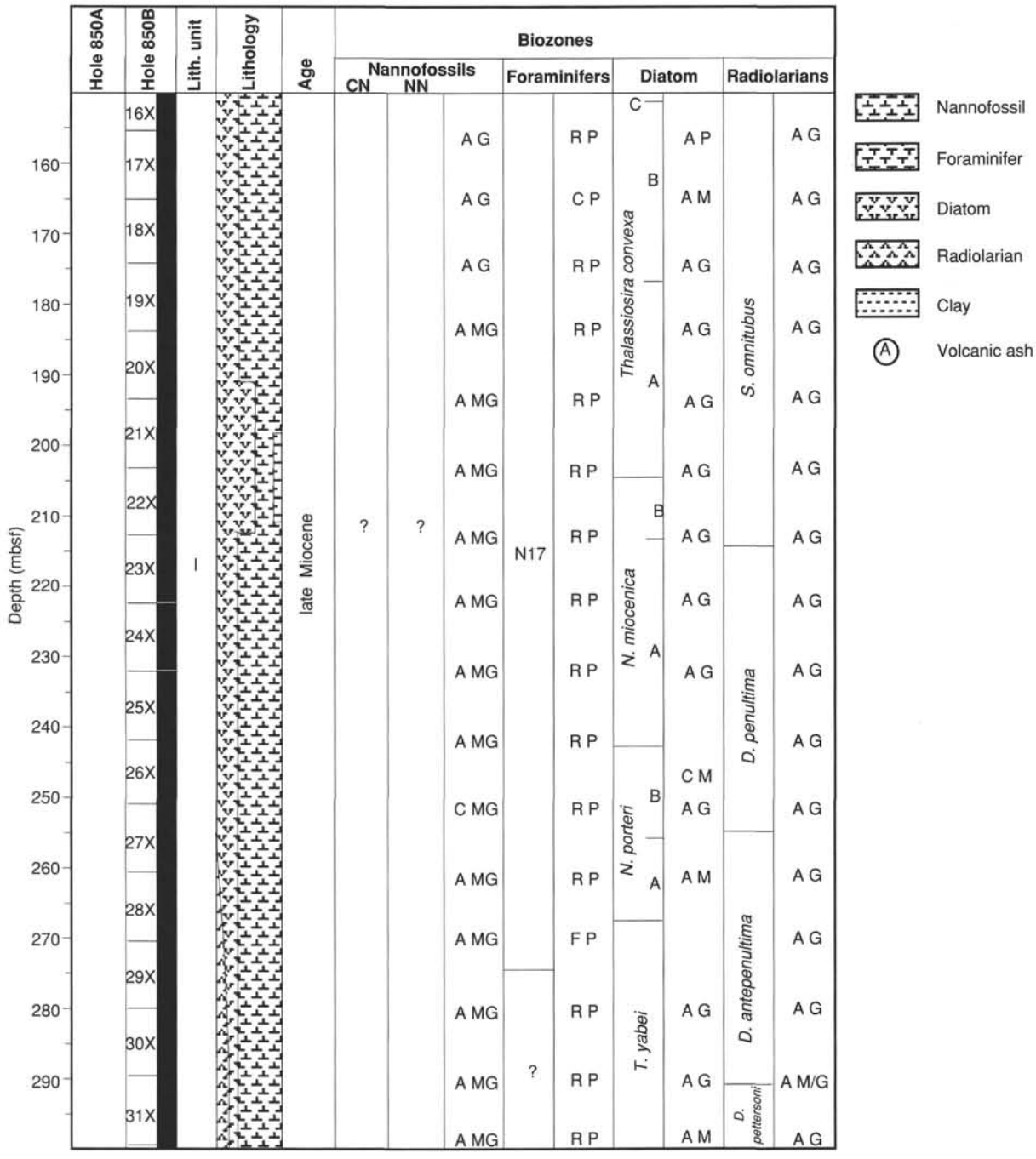

Figure 19 (continued).

first sections was homogeneous. Nonetheless, these samples will not be as representative of the general trends in sediment chemistry as were the scraped samples. Three samples of chert also were analyzed.

Most sediments had high concentrations of calcium carbonate. The shipboard algorithm used for calculating composition from the X-ray fluorescence intensity data was optimized for igneous rocks, and we encountered several problems when interpreting the composition data. For example, the concentrations indicated for MgO were negative because of the overlapping of the Ca and Mg fluorescence wavelengths used for analysis and the use of corrections for this overlapping that were based on an igneous rock matrix. The high concentrations of calcium in the sample also interfered with analyses of K_2O and Na_2O. The fluorescence intensity for TiO_2 was within the noise level of the instrument. Despite these problems, the sums of the major oxides accounted for by the analyses after taking into account loss on ignition (Table 12) suggest that the data for Al_2O_3, SiO_2, CaO, Fe_2O_3, MnO_2, and P_2O_5 are good. The high values for loss on ignition are typical of sediment rich in $CaCO_3$ and reflect CO_2 driven off on ignition.

Calcium and Calcium Carbonate

We compared several data sets of the sediment chemistry with other available Site 850 data sets to determine whether these data were reliable. Because virtually all of the CaO in the samples was from $CaCO_3$, we estimated the $\%CaCO_3$ from CaO (assuming that all CaO was present as $CaCO_3$ and that all loss on ignition was CO_2 driven off

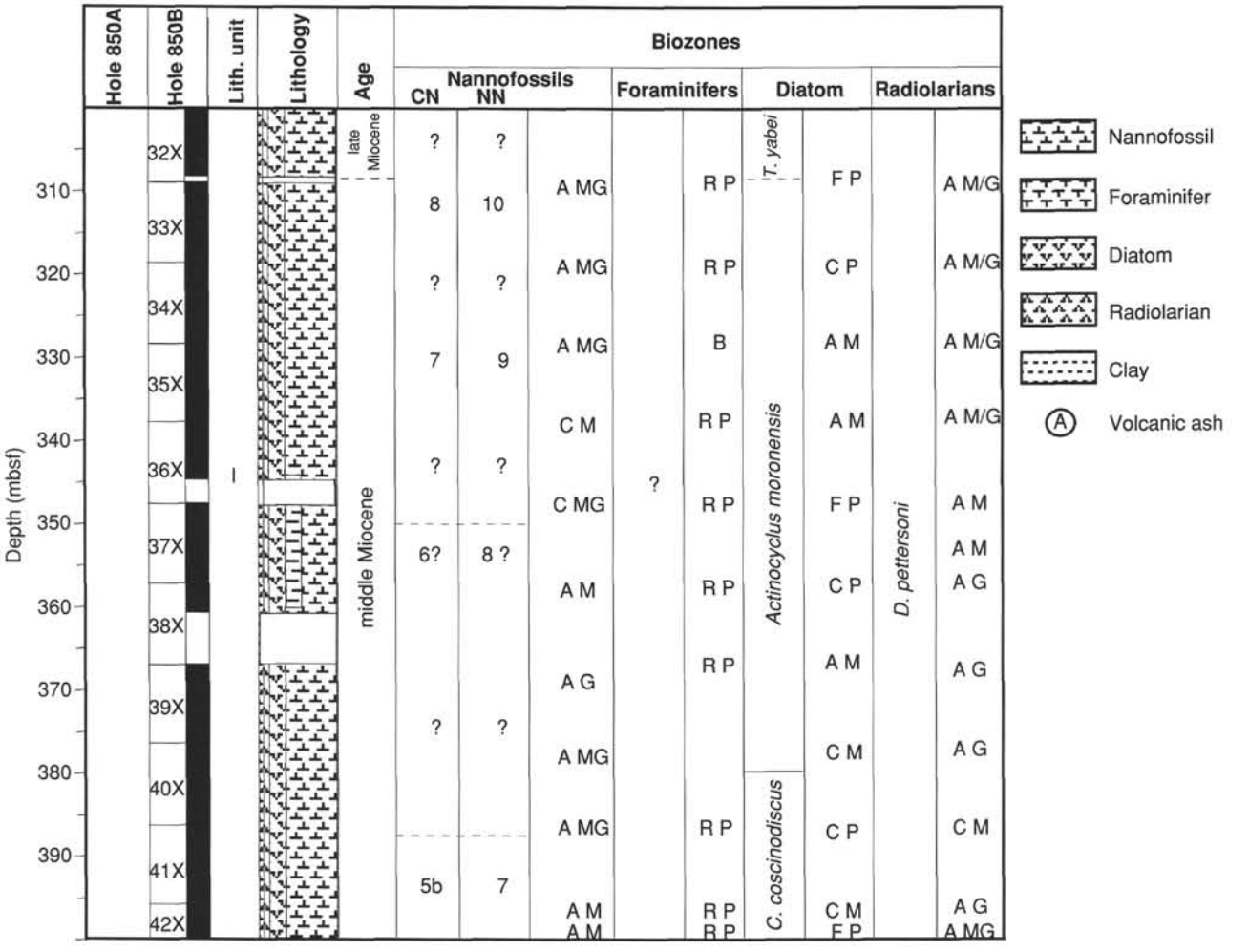

Figure 19 (continued).

the carbonate) and compared these data to independent coulometric $CaCO_3$ measurements of the same samples (Table 13; Fig. 34) to verify the CaO analyses. These data suggest that our $CaCO_3$ estimates (based on XRF data) were ~2.5 wt% too high, but that the difference between measured and estimated $CaCO_3$ was linear. Our assumption that all LOI was due to CO_2 loss undoubtedly was wrong and contributed to the error; however, the minimal difference between the two values suggests that the CaO data are good despite the inappropriate matrix correction algorithm. These data give credence to the other elemental data. These findings also indicate that the analytical data should be recalculated to take into account the fact that the loss on ignition was primarily the result of the carbonate content (Table 13).

Biogenic Silica

The sediments are very rich in silica (Fig. 35). The element suite allowed us to make an estimate of the biogenic silica (opal) content of the sediments. The crustal ratio of SiO_2/Al_2O_3 is roughly 3.0. Estimates of this ratio in Cenozoic equatorial Pacific Ocean sediments based on quantitative quartz and clay mineralogical analyses (Leinen, 1979) indicate that this value is reasonable for our samples. Therefore, an estimate of the biogenic silica content of the sediments (Fig. 36) is obtained from:

$$SiO_{2\,(biogenic)} = SiO_{2\,(total)} - (3 \times Al_2O_3).$$

The error for this estimate can be considerable, especially for low opal sediments. Overestimates of opal by as much as 20 wt% (on a carbonate-free basis) are possible (Leinen, 1977). One can better estimate content with the addition of other elements, notably MgO, but our XRF data preclude such refinements.

The estimate of biogenic silica suggests that the sediment contains roughly 10% to 20% biogenic silica (~40%–60% on a carbonate-free basis) in the upper foraminifer- and radiolarian-rich nannofossil ooze lithology (0–76 mbsf, 0–81 mcd), 20% biogenic silica (~60%–80% on a carbonate-free basis) in the diatom nannofossil ooze lithology (76–288 mbsf, 81–296 mcd), and 10% to 30% biogenic silica, excluding the cherts (~60%–80% on a carbonate-free basis) in the radiolarian nannofossil ooze lithology (288–397 mbsf, 296–405 mcd). In a few intervals, the nearly pure diatom oozes, the bulk sediments have as much as 40% to 60% opal, but the carbonate-free sediments never exceed 80 wt% opal. The concentration of opal on a carbonate-free basis exhibits less variability in the lower half of the site than concentration of bulk opal (Fig. 36) and implies a relatively constant balance between siliceous biogenic sedimentation and nonbiogenic sedimentation.

Elements from Terrigenous and Hydrothermal Sources

The Al_2O_3 concentration of the samples is very low in all sediments (Fig. 35), but is much greater in the upper 78 mbsf (87 mcd)

Table 8. Reversal boundary determinations.

Interval (cm)	Depth (mbsf)	Depth (mcd)	Interpretation[a]	Age (Ma)
850A-7H-1, 30	55.50	62.86	Kaena (t)	2.92
7H-2, 55	57.25	64.61	Kaena (o)	2.99
7H-3, 100	59.20	66.56	Mammoth (t)	3.08
7H-5, 35	61.55	68.91	Mammoth (o)	3.18
8H-1, 130	66.00	75.04	Gauss/Gilbert	3.40
850B-6H-5, 85	57.35	62.85	Kaena (t)	2.92
6H-6, 110	59.10	64.60	Keano (o)	2.99
7H-2, 70	62.20	68.77	Mammoth (o)	3.18
7H-6, 80	68.30	74.87	Gauss/Gilbert	3.40

[a] (t) = termination; (o) = onset.

and in the lower 100 m than in between. Despite the minimal detail of the Al log (Fig. 37; see "Downhole Measurements" section, this chapter), which was at the limit of Al detection, a comparison of the weight fraction of Al with the wt% Al_2O_3 determined by XRF confirms both the Al concentrations and the pattern of higher Al concentrations in the upper 75 mbsf and below 300 mbsf.

The Fe_2O_3 content of the sediment has maxima between 56 and 70 mbsf (63–78 mcd) and at 250 mbsf (260 mcd). The Fe_2O_3 concentrations are also large in the silica-poor intervals below 290 mbsf (300 mcd, Fig. 35). When calculated on a carbonate- and biogenic silica-free basis, Fe_2O_3 concentrations are about 5 to 7 wt% in the sediment above 250 mbsf and 10 to 20 wt% of the sediment below this depth. The pattern of Fe_2O_3 concentration does not match the Fe indicated in logs, however (Fig. 38; see "Downhole Measurements" section, this chapter). Unlike the logging data, the Fe_2O_3 in the bulk sediment, the Fe_2O_3 concentration in nonbiogenic sediment, the Fe/Al ratio, and the inferred hydrothermal Fe accumulation rate (Fig. 39) all show clear evidence of iron enrichment over the entire lower 100 m of the sediment sequence. Elemental yields, including iron, from the logging tool in the interval from 254.6 to 258.4 mbsf were large. The anomalously large Fe_2O_3 concentration at 251.75 mbsf (259.5 mcd; 2.94%, 15% carbonate-free) is very close to this depth interval. Smear slides and visual core descriptions of this interval provide no evidence of lithologic differences that might account for the high Fe_2O_3 concentrations.

The Fe/Al ratio of the sediments is always greater than the crustal ratio and the andesite ratio, suggesting that much of the iron is not terrigenous (Fig. 39). Heath and Dymond (1977) calculated the hydrothermal iron concentration of equatorial Pacific Ocean sediments assuming that the only significant sources of iron were terrigenous sediment and hydrothermal phases and that the terrigenous contribution of iron to the sediments was proportional to the Fe/Al crustal ratio, 0.6:

$$\text{wt\% hydrothermal Fe} = \text{wt\% Fe} - (0.6 \times \text{\% Al})$$

The hydrothermal iron content of the sediments calculated in this manner (Fig. 39) is ~0.2 to 1 wt% (5% of the carbonate-free fraction).

The concentration of MnO (Fig. 35, Table 13) is highest between 56 and 70 mbsf (63–78 mcd) and below 250 mbsf (260 mcd). The chemistry of Site 850 sediments does not show the characteristic Fe/Mn pattern with distance from the ridge crest (Fig. 39) that has been described by Lyle (1986) and that was present at Site 848. Most sediments are close to the hydrothermal Fe/Mn ratio of 3:1.

The P_2O_5 concentrations (Table 13, Fig. 35), like those of silica, are variable over the upper 300 m at the site, but show little change in average concentration (~0.075 wt%) with depth. The concentration of P_2O_5 is inversely correlated with SiO_2 in the upper 300 m. Below 300 m, P_2O_5 concentrations are highly variable and are at a minimum near the cherts. Froelich et al. (1977) have shown that phosphorus is enriched in metal-rich hydrothermal sediments near ridge crests because it is adsorbed onto the highly surface-reactive iron oxides and hydroxyoxides.

Table 9. Depths of top and bottom of each core in Site 850 in the composite depth section.

Core	ODP depth (mbsf)	Core length (m)	Composite depth (mcd)	Delta (m)
138-850A-1H	0.00–7.68	7.68	0.00–7.68	0.00
2H	7.70–16.74	9.04	9.25–18.29	1.55
3H	17.20–27.27	10.07	18.85–28.92	1.65
4H	26.70–36.83	10.13	29.70–39.83	3.00
5H	36.20–46.21	10.01	40.00–50.01	3.80
6H	45.70–55.81	10.11	51.45–61.56	5.75
7H	55.20–65.22	10.02	62.55–72.57	7.35
8H	64.70–74.76	10.06	73.70–83.76	9.00
-850B-1H	3.00–12.78	9.78	3.00–12.78	0.00
2H	12.50–22.15	9.65	14.40–24.05	1.90
3H	22.00–31.74	9.74	23.65–33.39	1.65
4H	31.50–41.57	10.07	35.85–45.92	4.35
5H	41.00–51.08	10.08	45.40–55.48	4.40
6H	50.50–60.60	10.10	56.00–66.10	5.50
7H	60.00–70.11	10.11	66.55–76.66	6.55
8H	69.50–79.59	10.09	77.25–87.34	7.75
9H	79.00–89.08	10.08	86.75–96.83	7.75
10H	88.50–98.49	9.99	96.25–106.24	7.75
11X	98.00–106.90	8.90	105.75–114.65	7.75
12X	107.50–117.00	9.50	115.25–124.75	7.75
13X	117.10–126.74	9.64	124.85–134.49	7.75
14X	126.80–136.38	9.58	134.55–144.13	7.75
15X	136.40–146.05	9.65	144.15–153.80	7.75
16X	146.10–155.60	9.50	153.85–163.35	7.75
17X	155.70–164.90	9.20	163.45–172.65	7.75
18X	165.00–174.65	9.65	172.75–182.40	7.75
19X	174.20–183.95	9.75	181.95–191.70	7.75
20X	183.80–193.53	9.73	191.55–201.28	7.75
21X	193.50–203.15	9.65	201.25–210.90	7.75
22X	203.10–212.83	9.73	210.85–220.58	7.75
23X	212.80–222.39	9.59	220.55–230.14	7.75
24X	222.50–231.95	9.45	230.25–239.70	7.75
25X	232.10–241.73	9.63	239.85–249.48	7.75
26X	241.80–251.49	9.69	249.55–259.24	7.75
27X	251.00–260.79	9.79	258.75–268.54	7.75
28X	260.70–270.26	9.56	268.45–278.01	7.75
29X	270.30–279.93	9.63	278.05–287.68	7.75
30X	279.90–289.57	9.67	287.65–297.32	7.75
31X	289.60–299.34	9.74	297.35–307.09	7.75
32X	299.20–308.22	9.02	306.95–315.97	7.75
33X	308.90–318.75	9.85	316.65–326.50	7.75
34X	318.60–328.50	9.90	326.35–336.25	7.75
35X	328.20–338.16	9.96	335.95–345.91	7.75
36X	337.80–344.67	6.87	345.55–352.42	7.75
37X	347.50–357.28	9.78	355.25–365.03	7.75
38X	357.10–360.77	3.67	364.85–368.52	7.75
39X	366.80–376.66	9.86	374.55–384.41	7.75
40X	376.40–386.18	9.78	384.15–393.93	7.75
41X	386.10–395.95	9.85	393.85–403.70	7.75
42X	395.80–399.92	4.12	403.55–407.67	7.75

Note: For a discussion of composite depth, see text.

Accumulation Rates

Biogenic Silica

The mass accumulation rate (g/cm²/ky) of estimated biogenic SiO_2 (opal; Fig. 40, Table 14) was calculated for the intervals represented by the XRF samples using the mass accumulation rates from Table 15. The opal accumulation rate has four maxima which exceed the average background rate of 200 mg/cm²/k.y. by at least a factor of five: 9.7–10.4 Ma (~1500 mg/cm²/k.y.), 5.9–6.6 Ma (~2500 mg/cm²/k.y.), 4.9 Ma (~1500 mg/cm²/k.y.) and 4.1 Ma (~1000 mg/cm²/k.y.).

The first period of high opal accumulation rates at the site, 9.7–10.4 Ma, is defined by discrete samples. The rates are highly variable, but lithologies in this interval are also highly variable: interbedded radiolarian nannofossil ooze, diatom nannofossil ooze, nannofossil ooze and chert. (The chert samples have not been included in the accumulation rate plots but they are listed in Table 14.) Laminated

Table 10. Control points for sedimentation rates.

Composite depth (mcd)	Rate (m/m.y.)	Age (Ma)	Remarks
0		0	Core top
30.94	21.34	1.45	T *Calcidiscus mcintyrei*
63.66	22.36	2.92	T Kaena subchron
65.40	24.86	2.99	B Kaena subchron
67.36	21.78	3.08	T Mammoth subchron
69.65	22.90	3.18	B Mammoth subchron
75.67	27.36	3.40	B Gauss chron
79.65	27.06	3.56	T *Reticulofenestra pseudoumbilicus*
116.65	33.32	4.66	B *Ceratolithus rugosus*
159.70	97.73	5.10	T *Thalassiosira miocenica*
185.00	36.21	5.80	T *Thalassiosira praeconvexa*
221.60	122.00	6.10	B *Thalassiosira praeconvexa*
250.90	43.70	6.75	B *Nitzschia miocenica*
267.4	27.50	7.35	T *Actinocyclus ellipticus* var. *javanicus*
274.85	37.25	7.55	T *Thalassiosira yabei*
313.03	30.50	8.80	T *Denticulopsis hustedti*
356.60	38.30	9.94	T *Coccolithus miopelagicus*
387.70	47.10	10.60	T *Craspedodiscus concinodiscus*

B = bottom occurrence; T = top occurrence.

diatom ooze dominated by pennate diatoms occurs in this time interval and it is likely that both the extremely high accumulation rates and the variability in the rates are real.

An opal accumulation rate maximum from 6.6 to 5.9 Ma is the best constrained period of high opal accumulation interval at the site. This time period comprises nannofossil diatom ooze, diatom nannofossil ooze, and chert that have exceptionally high opal contents (nearly 60 wt%) and that accumulated at exceptionally high rates (3000 mg/cm^2/k.y.). An opal accumulation rate maximum at 4.9 Ma is based on only one sample, but the rate reflects not only high bulk sediment accumulation rates (see "Organic Geochemistry" section, this chapter), but also an opal content nearly double that of sediments above and below the sample. The latest opal accumulation rate maximum (4.1 Ma) reflects very high opal contents rather than high bulk sediment accumulation rates. During all other peak opal accumulation intervals both the rate and the relative quantity of opal in the samples increases.

Aluminum

The mass accumulation rate of aluminum (Fig. 40, Table 14) is a good indicator of the terrigenous sediment influence at Site 850. As the crustal abundance of Al is about 7%, the accumulation rate of all terrigenous material should be roughly an order of magnitude greater than that of Al, or about 100 mg/cm^2/k.y. The accumulation rate of Al_2O_3 never increases by as much as a factor of 5 above the long term average, as does opal. Three times in the past, Al_2O_3 accumulation rates increased by a factor of two larger than average. The first time was 9.2 Ma. This maximum is a single point peak corresponding to an Al_2O_3 concentration maximum. During the 5.9–6.1 Ma sediment accumulation rate maximum, Al_2O_3 accumulation rates double. This change is entirely due to sedimentation rate increases, however, as the concentration is relatively low at the time. The peak at 4.9 Ma reflects an increase in both sediment accumulation and in Al_2O_3 concentration. The P_2O_5 accumulation rate (Fig. 40) is most nearly like that of Al_2O_3.

Iron and Manganese

The accumulation rates of Fe and Mn are influenced by both terrigenous and hydrothermal sources. An accumulation rate for the hydrothermal component of Fe_2O_3 (Fig. 39) is based on the assumptions discussed above. The hydrothermal Fe accumulation rate, as well as those of Fe_2O_3 and MnO (Fig. 40; Table 14), was greatest (20–60 mg/cm^2/k.y.) when the site was nearest the ridge crest at

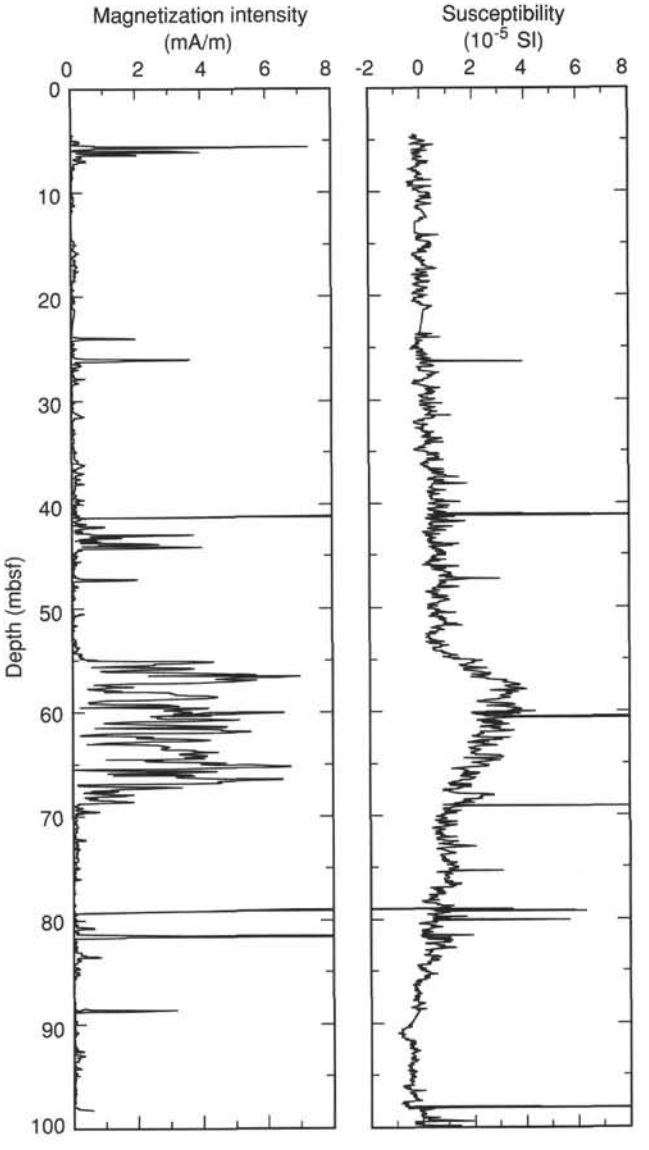

Figure 20. Remanent intensity (left) and low-field magnetic susceptibility (right) in the upper 100 m of Hole 850B. Remanence is after 15 mT demagnetization treatment.

11 Ma. Since that time, Fe_2O_3 and hydrothermal Fe accumulation rates have decreased exponentially as the site moved away from the spreading ridge. This pattern of exponential decrease with distance from the ridge is well known for modern hydrothermal sediments (Dymond, 1981) and ancient sediments formed at the East Pacific Rise (e.g., Leinen and Stakes, 1979; Lyle et al., 1986). Superimposed on the exponential decrease are three intervals of substantially greater hydrothermal deposition. The first of these occurred at 6.6–7 Ma when hydrothermal accumulation rates increased by a factor of four. This interval is particularly intriguing as it has the lowest bulk sediment accumulation rate of any time between 4 and 11 Ma. Thus, the enhanced burial rates are not due to stratigraphic averaging. Furthermore, the Al accumulation rates were quite low at this time and it is unlikely that the hydrothermal rate maximum is due to sediment ponding or other benthic or water column amplification processes. The depth interval equivalent to this time is that in which high Fe concentrations were measured by geochemical logs as well. The time interval has not been previously identified as an interval of enhanced hydrothermal activity, and MnO accumulation did not

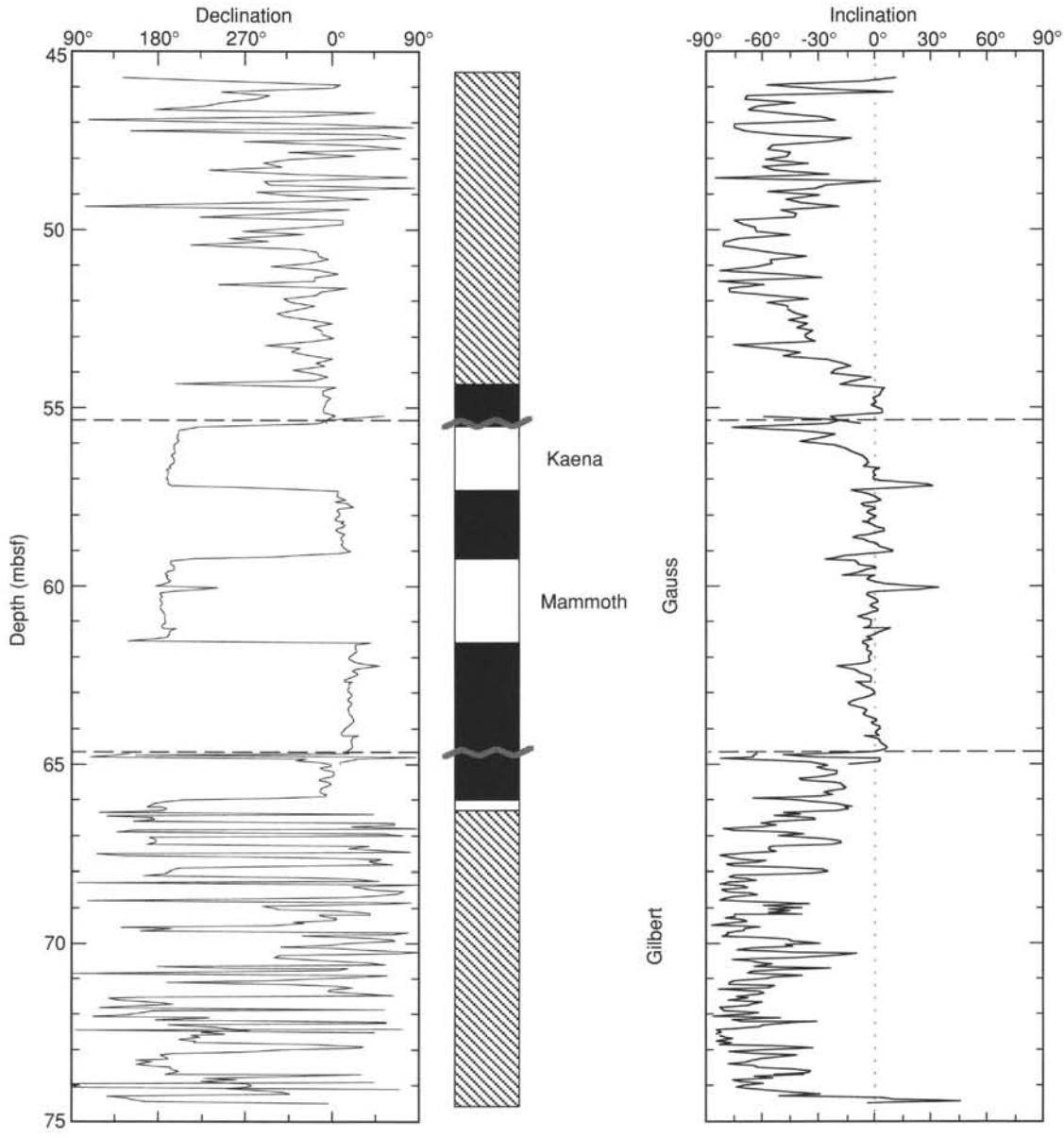

Figure 21. Remanence directions (after 15 mT demagnetization) in Cores 138-850A-6H, -850A-7H, and -850A-8H, with interpretation of polarity zonation. Black indicates normal polarity; white, reverse polarity; hatched lines, no interpretation. Declinations have been rotated accordingly, using the parameters given in Table 7. Dashed lines show location of core breaks.

increase at the same time. One other explanation for the rate maximum is that the high Fe_2O_3 concentrations were due to deposition of remobilized Fe from organic carbon diagenesis; the sediments from this interval contain a few pyritized burrows. However, sediments surrounding the interval are not depleted in Fe_2O_3. Peaks in Fe_2O_3 and hydrothermal Fe accumulation at 5.9 and 4.9 Ma correspond to the two primary biogenic sediment accumulation rate maxima at the site.

The highest MnO accumulation rates occurred between 9 and 11 Ma, when the site was near the ridge crest. MnO and Fe_2O_3 accumulation rates are strongly anti-correlated in sediments older than 10 Ma, which were rapidly accumulating biogenic sediments. Diagenetic remobilization of Mn associated with organic carbon oxidation is much more extensive than for Fe_2O_3 and may be responsible for the negative correlation. The 5.9–6.1 Ma and 4.9 Ma accumulation rate events are reflected in the MnO profiles.

Accumulation Rate Maxima at 5.9–6.1 and 4.9 Ma

It is unusual for sediment deriving from very different sources to have coincident accumulation maxima, such as those for opal, Al, hydrothermal Fe, MnO, and P_2O_5 at about 4.9 Ma and 5.9–6.1 Ma. Such coupled accumulation rate maxima often reflect errors in stratigraphy that amplify or reduce the accumulation rates of all sediment components. The stratigraphy of these intervals is well-constrained, (see "Biostratigraphy" section, this chapter), however, and it is unlikely that the maxima are solely artifacts. A second explanation,

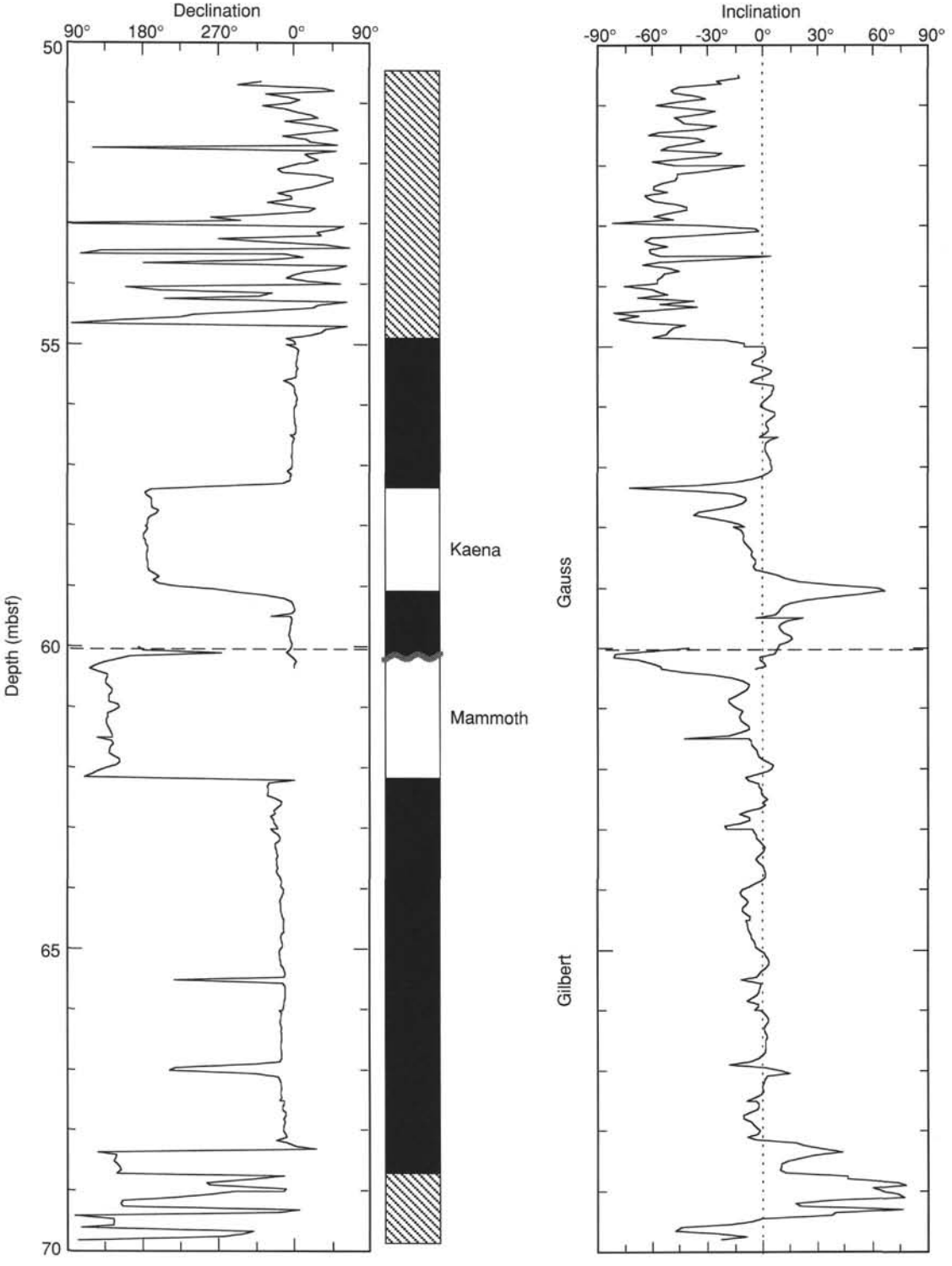

Figure 22. Remanence directions (after 15 mT demagnetization) in Cores 138-850B-6H and -850B-7H, with interpretation of polarity zonation. Black indicates normal polarity; white, reverse polarity; hatched lines, no interpretation. Declinations have been rotated accordingly, using the parameters given in Table 7. Dashed lines show location of core breaks.

which has been used frequently to explain similar biogenic and terrigenous accumulation rate patterns is that the terrigenous material is transported to the site by the wind and that the atmospheric circulation and upwelling are coupled leading to mutual increases in terrigenous and biogenic sediment accumulation. However, unless the supply of silica to the ocean increases much more than that of the terrigenous flux, the ocean quickly adjusts preservation of opal to a new steady state equilibrium and little of the excess opal flux is preserved. The extremely high accumulation rate, high silica content, diatom ooze events that occurred during the two accumulation rate maxima may have been relatively short and represent deposition in far less time than indicated by our shipboard stratigraphy (200 k.y.). The duration of the

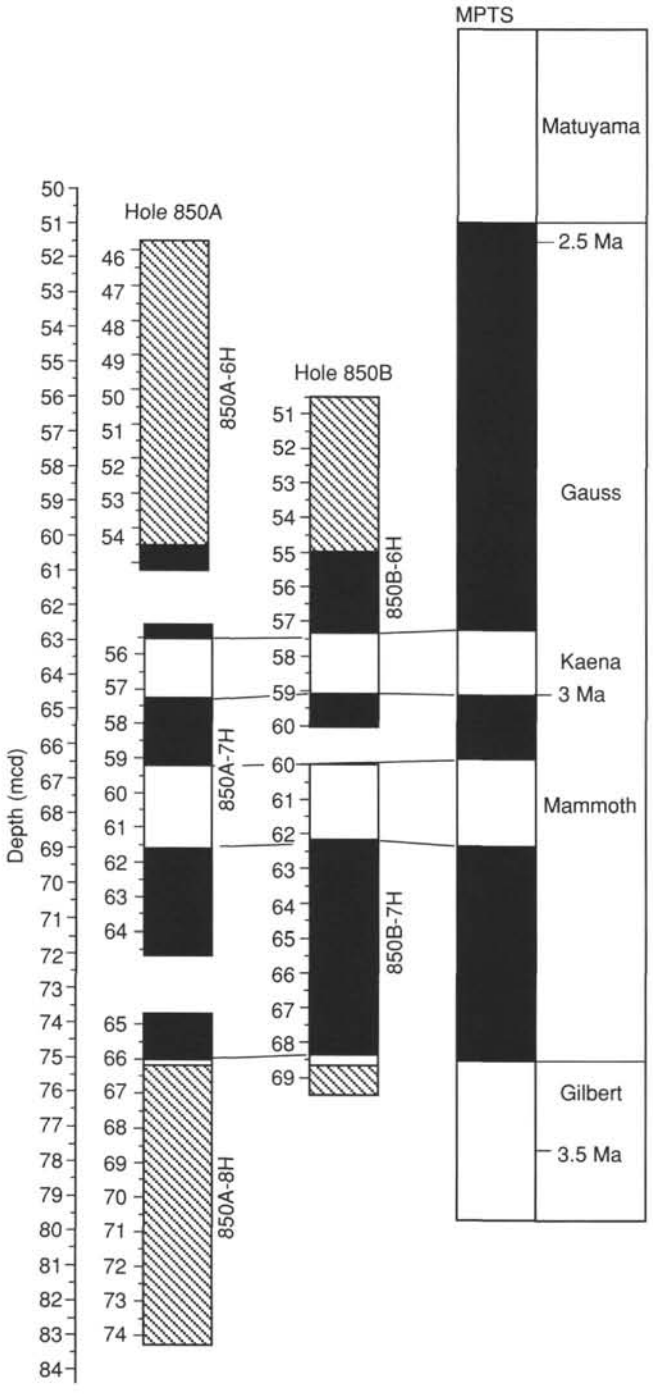

Figure 23. Composite magnetic polarity stratigraphy for the DMZ. Ticks on each core in mbsf; cores are placed in mcd according to scale at left. Correlation with a Pliocene interval of the magnetic polarity time scale shown by solid lines.

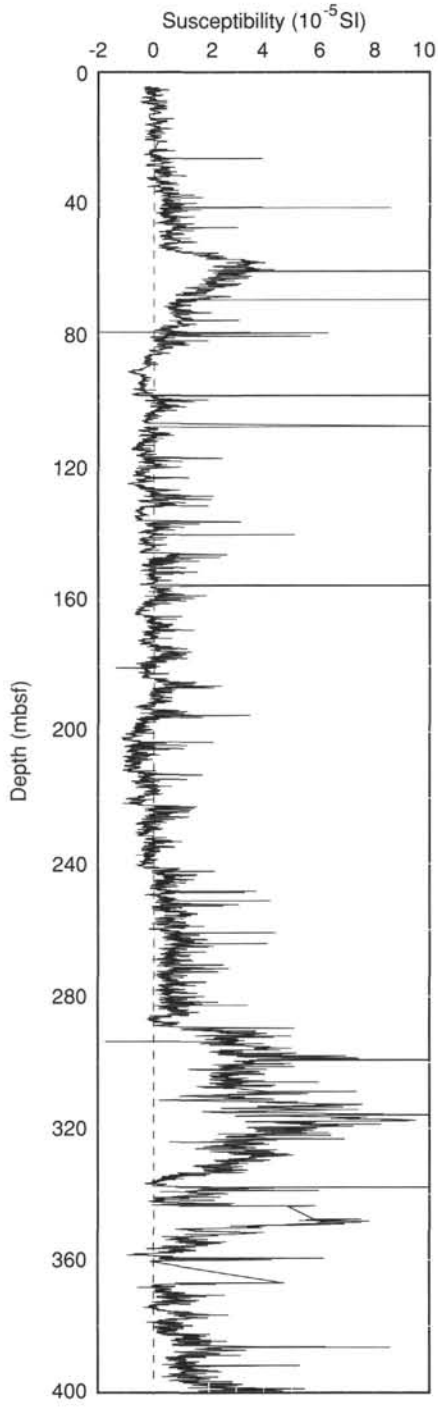

Figure 24. Low-field initial susceptibility from Hole 850B.

events might be close to the residence times of Si and P in seawater (20 k.y. and 70 k.y., respectively), but were probably much longer than the residence time of Al (620 yr), Mn (1.3 k.y.), and Fe (54 yr) (Broecker and Peng, 1982). We know little of the geochemical cycle of lithophile elements in particles on such time scales. It is possible, for example, that much of the standing stock of detrital Al-bearing particles was transported to the seafloor rapidly in a single bloom event. However, over scales of even a few 100 yr the deposition rate of Al would decrease unless continental supply increased. Thus these rates, if substantiated by more detailed sediment chemistry, challenge our concepts of how terrigenous fluxes and biogenic fluxes are coupled.

Invoking a coupled flux does not explain a change in the flux of hydrothermal Fe or in MnO. One possible explanation is that oxidation of the organic carbon associated with the very high biogenic accumulation rates resulted in reduction diagenesis of Fe and Mn in terrigenous and hydrothermal phases and its eventual deposition in the upper portions of the high sedimentation rate intervals. The restriction of the Fe and Mn accumulation rate maxima to the most

Table 11. Interstitial water geochemical data for Holes 850A and 850B.

Core, section, interval (cm)	Depth (mbsf)	pH	Salinity	Chloride (mM)	Sodium (mM)	Alkalinity (mM)	Sulfate (mM)	Magnesium (mM)	Calcium (mM)	Potassium (mM)
850A-1H-1, 145–150	1.5	7.29	35.5	556	484	2.985	28.03	53.54	10.45	10.7
850B-3H-6, 145–150	31.0	7.18	36.0	559	487	3.670	27.44	53.42	10.26	11.2
6H-6, 145–150	59.5	7.16	36.5	559	486	4.024	26.76	53.46	9.73	11.3
9H-6, 142–150	88.0	7.12	35.2	560	487	4.231	25.20	52.43	9.31	10.9
12X-6, 142–150	116.5	7.20	35.0	561	487	4.713	24.23	51.87	9.23	10.5
15X-6, 144–150	145.4	7.10	34.8	559	485	5.406	23.80	51.49	9.13	10.7
18X-5, 144–150	172.5	7.07	35.0	555	480	5.161	22.54	51.12	8.78	10.6
21X-6, 144–150	202.5	7.30	35.0	556	483	5.388	22.82	50.74	8.75	10.4
24X-6, 144–150	231.5	7.10	35.0	554	480	5.382	22.25	50.50	8.75	10.6
27X-6, 145–150	260.0	7.09	34.8	557	484	5.414	21.97	49.95	8.74	10.6
30X-6, 144–150	288.9	7.09	36.5	556	482	4.999	22.45	50.62	8.79	10.8
33X-6, 142–150	317.9	7.31	34.8	555	481	3.800	22.94	51.00	8.74	11.2
36X-6, 140–150	343.8	7.18	35.5	556	483	3.996	23.21	50.93	9.05	11.0
39X-6, 140–150	374.3	7.31	35.5	558	484	2.979	27.95	53.49	11.23	10.3
40X-6, 140–150	385.4	7.25	35.5	557	484	2.556	27.67	53.32	10.84	10.8
41X-6, 140–150	395.1	7.34	—	557	483	2.631	27.34	53.46	10.78	10.4
42X-2, 140–150	398.8	7.24	—	556	482	2.636	27.44	53.65	10.67	10.1

— indicates a missed analysis.

recent part of the biogenic accumulation rate maximum could reflect such remobilization and redeposition.

ORGANIC GEOCHEMISTRY

Carbonate and Organic Carbon

Concentrations of inorganic and organic carbon were measured in one sample per section in Holes 850A and 850B following the methods outlined in the "Explanatory Notes" chapter (this volume). From the inorganic carbon data, we calculated the weight percent of calcium carbonate (%$CaCO_3$). Percent organic carbon (%C_{org}) was determined in approximately one sample per core in Hole 850A and in two samples per core in Hole 850B. To determine concentrations of C_{org}, we measured the amount of carbon in the dried residues from Coulometer analyses after treatment with 2N HCl (see "Explanatory Notes" chapter, this volume) to optimize results in sediments low in C_{org} and high in carbonate. The analytical results are listed in Table 16 (CD ROM, back pocket) with respect to both ODP depth (mbsf) and to composite depth (mcd; see "Sedimentation Rates" section, this chapter). If a duplicate analysis was performed on a given sample, the mean value of the original analysis and the duplicate is listed in Table 16. Duplicate %$CaCO_3$ analyses are listed in Table 17 (CD ROM, back pocket). The results indicate a reproducibility of 0.7%.

Figures 41 and 42 show %$CaCO_3$ and %C_{org} vs. ODP depth and vs. composite depth and age, respectively, based on datum levels identified at Site 850 (see "Sedimentation Rates" and "Paleomagnetism" sections, this chapter). The %$CaCO_3$ record at Site 850 is characterized by high values (near 75%) that are punctuated by several intervals of significantly lower %$CaCO_3$ (from 20% to 50%; Fig. 41). Organic carbon concentrations are low (0.0%–0.2% with a few higher values in the range 0.3%–0.5%). Most of the low %$CaCO_3$ intervals coincide with increased diatom percentages, based on smear slide analysis (see "Lithostratigraphy" section, this chapter). The low %$CaCO_3$ intervals are also often associated with higher C_{org} values. According to shipboard chronostratigraphy, several of the low carbonate intervals appear to be coeval with low %$CaCO_3$ intervals at companion Sites 848 and 849.

Accumulation Rates

We calculated the average values of several sedimentary parameters in time intervals delimited by the chronostratigraphic levels discussed in the "Sedimentation Rates" section (this chapter) to estimate mass accumulation rates (MARs) of bulk sediment and individual sedimentary components. The average values of %$CaCO_3$, %C_{org}, linear sedimentation rate (LSR), dry bulk density (DBD), bulk-sediment mass accumulation rate (bulk MAR), $CaCO_3$ MAR, non-$CaCO_3$ MAR, and C_{org} MAR for 17 time intervals since 10.6 Ma are listed in Table 15. The mean values are presented vs. composite depth in Figure 43 and vs. age in Figure 44. Superimposed on the mean values are estimates of the instantaneous MAR calculated for each sample. The mean accumulation rates of bulk sediment reach up to 6.5 g/cm^2/k.y. in the period from 7 to 4 Ma at Site 850, but do not exceed 3 g/cm^2/k.y. in either the middle and lower Miocene or the Pleistocene. The broad maximum of accumulation rates in the period from 8 to 4 Ma is a common feature at Sites 848, 849, and 850.

Gas Geochemistry

One sample for gas analysis was taken from each core of Hole 850B. Gas was released from a sediment sample (about 5 cm^3) by thermal desorption (i.e., the "headspace technique," see "Explanatory Notes" chapter, this volume) and the measured concentrations of hydrocarbons in the head space volume (in ppm) were converted to µL/L of sediment and are reported in Table 18 (CD ROM, back pocket). Methane concentrations do not exceed 40 µL/L sediment, and ethane and higher hydrocarbon gases are below detection limits. An intriguing feature of the methane concentration curve with depth (Fig. 45) is the abrupt increase in sorbed methane concentrations at a depth of approximately 130 mbsf, below which level concentrations per volume of sediment increase by a factor of 3. Several of the interstitial water compositional parameters exhibit changes that indicate a tight coupling between production of methane and diagenesis of organic matter under suboxic conditions (see "Inorganic Geochemistry" section, this chapter). The maximum values for sorbed methane coincide with a minimum in interstitial sulfate concentration around 240–260 mbsf. Ammonia concentration in the pore waters also appears to be highly correlated with methane concentration.

PHYSICAL PROPERTIES

Introduction

A complete set of physical property measurements were performed on cores from Site 850. For whole-round sections, GRAPE-density, compressional-wave velocity (using the multisensor track [MST]), and thermal conductivity were measured. On split cores, wet-bulk density, dry-bulk density, grain density, porosity, wet water content, dry water content, and void ratio were measured. Vane shear

Table 11 (continued).

Core, section, interval (cm)	Strontium (μM)	Lithium (μM)	Silica (μM)	Ammonia (μM)
850A-1H-1, 145–150	89	26.9	857	15
850B-3H-6, 145–150	136	21.6	865	130
6H-6, 145–150	187	18.8	872	142
9H-6, 142–150	238	15.6	918	177
12X-6, 142–150	290	12.6	985	179
15X-6, 144–150	342	10.7	1079	270
18X-5, 144–150	363	8.8	1033	349
21X-6, 144–150	411	8.8	1099	343
24X-6, 144–150	420	8.4	1120	372
27X-6, 145–150	417	8.4	1163	398
30X-6, 144–150	390	10.4	1099	343
33X-6, 142–150	373	11.4	1140	330
36X-6, 140–150	320	12.1	1240	338
39X-6, 140–150	104	18.2	1125	15
40X-6, 140–150	97	18.7	1099	<10
41X-6, 140–150	95	22.9	1099	<10
42X-2, 140–150	92	23.6	918	<10

strength and compressional-wave velocity measurements were also made on split cores. The digital sonic velocimeter (DSV) was employed for discrete sample velocity measurements.

Physical properties were measured in every section of cores recovered from Hole 850B. Velocity, shear strength, and index properties were measured twice per section, while shear strength was measured only for the sections recovered by the APC. In Hole 850A, velocity and index properties were measured once per section. Shear strength and thermal conductivity were not measured in Hole 850A. Index property samples were always taken at the same depth interval as the velocity measurements. Thermal conductivity was routinely measured for Sections 1, 3, and 7 for cores from Hole 850B.

Index Properties

Wet-bulk density values range from 1.22 to 1.7 g/cm^3 and generally increase with depth although the variability of the data is high (Fig. 46; Table 19, CD ROM, back pocket). Dry water content ranges from 291% to 55% and porosity from 88% to 59% (Figs. 47 and 48; Table 19). Both of these parameters generally increase with depth but also exhibit the high variability seen in the bulk density data. Grain density varies between 2.20 and 2.88 g/cm^3, with most values lying in the range between 2.50 and 2.70 g/cm^3 (Fig. 49; Table 19, CD ROM, back pocket).

Compressional-Wave Velocity

Compressional-wave velocity was measured parallel to the core axis on split cores from Hole 850A and 850B (Fig. 50; Table 20, CD ROM, back pocket). Some data between 154 and 260 mbsf are missing due to a computer storage problem.

Velocity values range between 1502 m/s and 1597 m/s and generally increase with depth. The logging velocity values in the interval of missing data systematically increase except for around 200 mbsf, where high porosity-diatom-rich sediments occur (see "Downhole Measurements" and "Lithostratigraphy" sections, this chapter).

Shear Strength

The profile of undrained shear strength for Hole 850B is presented in Figure 51 (Table 21, CD ROM, back pocket). The values range between 11.3 and 138.5 kPa and generally increase with depth. The high strength value at 98 mbsf corresponds to an interval having high diatom concentrations (see "Lithostratigraphy" section, this chapter). The effect of interlocking structure of diatomaceous sediment (which results in high shear strength) was documented by Hill and Marsters (1990) and was seen at other sites during this leg (see "Physical Properties" section at Sites 845, 846, and 849).

Thermal Conductivity

Thermal conductivity (Fig. 52; Table 22, CD ROM, back pocket) varies from 0.74 to 1.41 W/(m•K). The mean value is 1.08 W/(m•K), with most values found between 0.9 and 1.3 W/(m•K). Because thermal conductivity is mainly determined by water content (Bullard, 1963), the profile mirrors those of porosity and dry water content.

Relationships of Physical Properties to Lithology

Variations in index properties at Site 850 are closely related to sediment composition and progressive diagenesis. The effect of composition on index properties can be seen by comparing calcium carbonate content (see "Organic Geochemistry" section, this chapter) and index properties profiles. The occurrence of a radiolarian-rich zone at about 24 mbsf corresponds to a decrease in wet-bulk density and an increase in dry water content and porosity. The first large minimum in grain density (2.45 g/cm^3) also occurs at this depth. This increase in radiolarian abundance results in a decrease in grain density because the grain density of biogenic silica is lower (2.0–2.1 g/cm^3; Baas Becking and Moore, 1959) than biogenic calcite (2.72 g/cm^3). Similar variations in index properties can be seen at 90 to 100 mbsf, 175 to 215 mbsf, 250 to 260 mbsf, and 290 to 340 mbsf.

Between 76 and 255 mbsf, the index property profiles reflect the progressive effects of diagenesis and consolidation with depth. Wet-bulk density increases and porosity and water content decrease with depth as a result of dewatering processes due to mechanical compaction. Grain density is relatively constant in this interval, except for around 200 mbsf, where sediments consist of nannofossil diatom ooze (up to 80% diatom). Below 300 mbsf, index properties such as porosity and water content decrease rapidly indicating compaction.

DOWNHOLE MEASUREMENTS

Hole 850B is the middle site in the detailed equatorial transect at 110°W (Sites 849–851). Since these sites are each separated by less than 150 km it is not surprising that the logs from all three sites resemble each other closely. Nevertheless, each site is distinctive in detail. For example, Site 849, which is now on the equator, has an expanded Pliocene-Pleistocene section when compared to the other two. Site 850, at 1°17′N, crossed the equator at about 4 Ma, and has an expanded late Miocene-Pliocene section. Many of the differences between the three sites occur in the XCB-cored interval, and logging data help to provide stratigraphic control in the critical Miocene intervals.

Quality of Data

Table 23 lists the usable log intervals recorded in Hole 850B. The data collected are of high quality except for GST data in the interval 254.6–258.4 mbsf, where the tool briefly fell out of calibration. This interval is marked by a large spike in all the elemental yields from the tool (Ca, Fe, Si, S, Cl, and H). The large data variations also apparently affected the transmission of aluminum data from the ACT. Aluminum data from precisely the same interval are bad, even though the tools are separated on the string by over 10 m. Since data from all the tools in the string are stored in buffers and reported simultaneously for each depth interval, one must suspect that the bad data from the GST contaminated the ACT data. Natural gamma-ray activity over this interval is normal and compares well with that seen during other logging runs.

All the density data are good, except for a short interval between 73.7 and 76.3 mbsf near the top of the logged interval and another

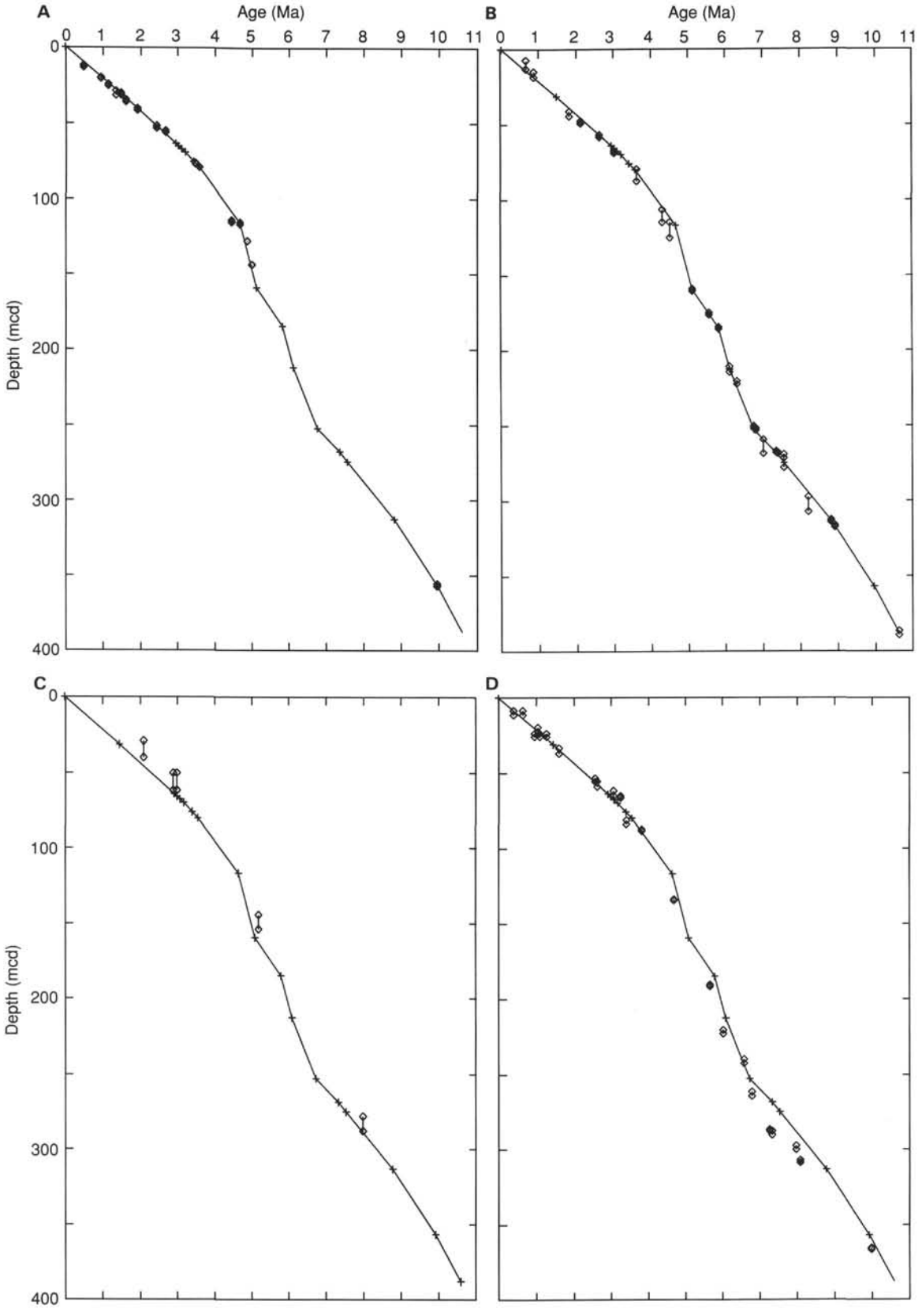

Figure 26. Plot of age vs. depth for Site 850 based on the calibration points in Table 10, compared with microfossil datums. **A.** Nannofossils. **B.** Diatoms. **C.** Foraminifers. **D.** Radiolarians. For radiolarians, only datums that have appeared consistent in the earlier sites of Leg 138 are shown. Age control points from Table 10 are indicated by crosses. Depth range of datums is shown by paired symbols.

Table 12. Concentrations of SiO_2, $A1_2O_3$, Fe_2O_3, MnO, CaO, Na_2O, K_2O and P_2O_5 in ignited sediments from Site 850.

Core, section, interval (cm)	Depth (mbsf)	Depth (mcd)	SiO_2 (wt%)	TiO_2 (wt%)	Al_2O_3 (wt%)	Fe_2O_3 (wt%)	MnO (wt%)	CaO (wt%)	Na_2O (wt%)	K_2O (wt%)	P_2O_5 (wt%)	Total (wt%)	LOI (wt%)
138-850A-1H-1, 0–150	0.00	0.75	20.01	0.00	0.99	0.69	0.29	76.93	0.00	0.00	0.11	99.02	43.03
2H-1, 0–150	7.70	10.00	14.12	0.00	1.17	0.90	0.17	82.38	0.00	0.00	0.14	98.88	41.28
3H-1, 0–150	17.20	19.60	23.37	0.00	1.20	1.01	0.20	71.49	0.00	0.00	0.13	97.40	41.27
4H-1, 0–150	26.70	30.45	23.85	0.00	1.48	1.34	0.28	70.70	0.00	0.00	0.13	97.78	38.62
5H-1, 0–150	36.20	40.75	31.10	0.00	1.25	1.27	0.27	64.06	0.00	0.00	0.11	98.06	37.25
6H-1, 0–150	45.70	52.20	19.77	0.00	1.23	1.55	0.39	73.28	0.00	0.00	0.14	96.36	39.16
7H-1, 0–150	55.20	63.30	23.19	0.00	1.41	1.90	0.45	69.70	0.00	0.00	0.16	96.81	38.39
8H-1, 0–150	64.70	74.45	28.93	0.00	1.37	1.75	0.43	65.50	0.00	0.00	0.17	98.15	36.97
-850B-1H-1, 0–150	3.00	3.75	32.34	0.00	1.63	1.07	0.21	62.87	0.00	0.00	0.13	98.25	38.55
8H-1, 0–150	69.50	78.00	17.52	0.00	1.35	1.69	0.46	76.22	0.00	0.00	0.13	97.37	39.76
10H-1, 0–150	88.50	97.00	42.07	0.00	0.72	0.64	0.19	53.00	0.00	0.00	0.09	96.71	33.50
11X-1, 0–150	98.00	106.50	16.82	0.00	0.80	0.73	0.16	79.68	0.10	0.00	0.12	98.41	40.55
14X-1, 0–150	126.80	135.30	31.44	0.00	0.86	1.31	0.17	63.27	0.00	0.00	0.14	97.19	35.23
17X-1, 0–150	155.70	164.20	19.40	0.00	0.60	0.74	0.22	76.91	0.00	0.00	0.11	97.98	39.34
18X-1, 0–150	165.00	173.50	28.45	0.00	0.58	0.82	0.12	67.64	0.00	0.00	0.10	97.71	36.92
19X-1, 0–150	174.20	182.70	18.69	0.00	0.61	0.73	0.22	77.40	0.00	0.00	0.16	97.81	39.53
20X-1, 0–150	183.80	192.30	27.75	0.00	0.67	1.22	0.22	66.66	0.00	0.00	0.13	96.65	36.46
21X-1, 0–150	193.50	202.00	58.99	0.00	0.49	0.56	0.07	36.53	1.02	0.02	0.05	97.73	26.45
22X-1, 0–150	203.10	211.60	57.75	0.00	0.47	0.56	0.08	39.08	0.71	0.00	0.05	98.70	28.22
23X-1, 0–150	212.80	221.30	34.83	0.00	0.56	0.65	0.16	62.51	0.04	0.00	0.09	98.84	36.68
24X-1, 0–150	222.50	231.00	27.34	0.00	0.46	0.67	0.10	70.42	0.00	0.00	0.11	99.10	37.22
25X-1, 0–150	232.10	240.60	35.03	0.00	0.50	1.31	0.17	60.10	0.70	0.00	0.08	97.89	34.68
27X-1, 0–150	251.00	259.50	36.75	0.00	0.61	2.94	0.26	52.81	1.47	0.01	0.06	94.91	32.06
28X-1, 0–150	260.70	269.20	26.16	0.00	0.62	1.26	0.32	71.18	0.00	0.00	0.10	99.64	37.90
29X-1, 0–150	270.30	278.80	16.61	0.00	0.65	1.14	0.25	78.86	0.00	0.00	0.12	97.63	39.67
30X-1, 0–150	279.90	288.40	15.94	0.00	0.73	1.40	0.28	79.90	0.00	0.00	0.12	98.37	39.34
31X-1, 0–150	289.60	298.10	29.05	0.00	0.76	1.49	0.33	66.08	0.00	0.00	0.11	97.82	35.89
32X-1, 60–62	299.80	307.56	21.65	0.00	1.02	2.02	0.27	72.40	0.00	0.00	0.16	97.52	37.81
33X-1, 81–83	309.71	317.47	50.15	0.00	0.75	1.23	0.27	45.36	0.44	0.00	0.07	98.27	29.45
34X-1, 127–129	319.87	327.63	45.37	0.00	1.20	3.04	0.41	45.49	0.49	0.01	0.16	96.17	29.54
35X-1, 86–88	329.06	336.82	32.41	0.00	0.86	2.32	0.41	61.50	0.00	0.00	0.17	97.67	34.48
36X-1, 60–62	338.40	346.16	79.10	0.00	0.59	1.32	0.19	17.98	1.97	0.09	0.03	101.27	18.09
36X-1, 70–72	338.50	346.26	99.46	0.00	0.38	0.28	0.05	2.55	0.00	0.00	0.00	102.72	8.27
37X-1, 44–46	347.94	355.70	17.79	0.00	1.17	2.63	0.46	74.97	0.00	0.00	0.22	97.24	38.71
38X-1, 28–30	357.38	365.14	45.06	0.00	0.83	1.58	0.36	49.88	0.73	0.01	0.09	98.54	30.74
38X-2, 63–66	359.23	366.99	96.78	0.00	0.39	0.61	0.07	5.14	0.00	0.00	0.00	102.99	10.46
38X-2, 133–136	359.93	367.69	93.62	0.00	0.33	0.27	0.08	8.23	0.00	0.00	0.00	102.53	11.96
39X-1, 40–42	367.20	374.96	51.06	0.00	0.64	2.66	0.22	41.31	0.90	0.03	0.08	96.90	27.69
40X-1, 41–43	376.81	384.57	18.06	0.00	0.69	1.51	0.36	77.23	0.00	0.00	0.27	98.12	40.61
41X-1, 43–47	386.53	394.29	24.56	0.00	0.74	3.33	0.19	68.08	0.00	0.00	0.18	97.08	36.76
42X-1, 45–47	396.25	404.01	31.36	0.00	0.59	2.32	0.19	63.97	0.00	0.00	0.11	98.54	34.85

LOI = loss on ignition.

short interval between 361.4 and 362.0 mbsf, where cherts are found (Fig. 53). Velocity data are good except for four small dropouts between 345 and 365 mbsf (348.4 mbsf, 351–351.8 mbsf, 359.6–360.3 mbsf, and 362.4–363.2 mbsf).

FMS data are also good, even though the log was run without heave compensation. A few uncompensated accelerations can be found in the logged interval, but not many. Between 114 and 88 mbsf, the hole is wider than the FMS calipers in one direction, and only two pads of the FMS are in contact with the wall in this interval.

Log Stratigraphic Units

The logging data from Hole 850B are similar to Site 846 but more subdued, as are the data from Sites 849 and 851 (compare Fig. 53, this chapter, with Fig. 42, "Site 846" chapter, this volume). For example, log stratigraphic Unit 2 in Hole 846B is equivalent to the depth interval between about 300 and 360 mbsf in Hole 850B. In Hole 850B, however, the density/velocity/resistivity minimum is not as pronounced as in log Unit 2 of Hole 846B. For example, the wet bulk density difference between the interval and the sediments above is about 0.1 g/cm^3 less in Hole 850B than at Hole 846B (Fig. 54). Because the log responses were subdued we decided to group the entire sediment column at Site 850B into one log stratigraphic unit.

The geochemical logs show periodic variations but no distinct sedimentary intervals (Fig. 55). The strongest signal in both the Si and Ca logs is the chert interval centered at 360 mbsf. The cherts appear as a pronounced Ca yield minimum and a Si yield maximum. Unlike Sites 845, 846, and 848, the logs show no strong Fe-rich basal interval. The lithostratigraphic descriptions also indicate that the basal metalliferous sediment layer is not as pronounced at Site 850 as at some of the earlier sites (see "Lithostratigraphy" section, this chapter).

Cherts at Site 850

The chert section in Hole 850B has some surprising details that only appear on close examination of the interval. Based on the porewater geochemistry (see "Inorganic Geochemistry" section, this chapter), the cherts form a barrier to pore water diffusion. Porewater composition below them is significantly different to the pore water composition immediately above them. The FMS resistivity images of the borehole wall have given a detailed view of their *in-situ* structure. Actually, two intervals of chert can be seen. One small interval occurs at approximately 344 mbsf and was recovered in Core 850B-36X (Fig. 56; see "Lithostratigraphy" section, this chapter) and shows up as a thin white stripe in the middle of a major dark (low resistivity/high porosity) interval. The major chert interval occurs between 360 and 365 mbsf (Figs. 56 and 57). It is composed of 4 chert layers that appear as white bands at 360.2, 360.4, 361.3, and 363.7 mbsf. Two of these chert layers were recovered in Core 138-850B-38X (see "Lithostratigraphy" section, this chapter). The top chert layer separates dark, high porosity/low resistivity sediment from less porous sediment.

Table 13. Concentrations of SiO_2, Al_2O_3, Fe_2O_3, MnO, CaO, Na_2O, K_2O and P_2O_5 in ignited sediments from Site 850 recalculated assuming all loss on ignition is CO_2 driven off $CaCO_3$.

Core, section, interval (cm)	Depth (mbsf)	Depth (mcd)	SiO_2 (LOI) (wt%)	Al_2O_3 (LOI) (wt%)	Fe_2O_3 (LOI) (wt%)	MnO (LOI) (wt%)	CaO (LOI) (wt%)	Na_2O (LOI) (wt%)	K_2O (LOI) (wt%)	P_2O_5 (LOI) (wt%)	$CaCO_3$ (measured)	$CaCO_3$ (estimated)
138-850A-1H-1, 0–150	0.00	0.75	11.40	0.56	0.39	0.17	43.83	0.00	0.00	0.06	77.15	78.21
2H-1, 0–150	7.70	10.00	8.29	0.69	0.53	0.10	48.37	0.00	0.00	0.08	82.65	86.33
3H-1, 0–150	17.20	19.60	13.73	0.70	0.59	0.12	41.99	0.00	0.00	0.08	75.04	74.93
4H-1, 0–150	26.70	30.45	14.64	0.91	0.82	0.17	43.40	0.00	0.00	0.08	73.94	77.44
5H-1, 0–150	36.20	40.75	19.52	0.78	0.80	0.17	40.20	0.00	0.00	0.07	67.93	71.74
6H-1, 0–150	45.70	52.20	12.03	0.75	0.94	0.24	44.58	0.00	0.00	0.09	76.74	79.56
7H-1, 0–150	55.20	63.30	14.29	0.87	1.17	0.28	42.94	0.00	0.00	0.10	73.26	76.63
8H-1, 0–150	64.70	74.45	18.23	0.86	1.10	0.27	41.28	0.00	0.00	0.11	70.30	73.68
-850B-1H-1, 0–150	3.00	3.75	19.87	1.00	0.66	0.13	38.63	0.00	0.00	0.08	65.40	68.95
8H-1, 0–150	69.50	78.00	10.55	0.81	1.02	0.28	45.91	0.00	0.00	0.08	78.85	81.94
10H-1, 0–150	88.50	97.00	27.98	0.48	0.43	0.13	35.25	0.00	0.00	0.06	61.76	62.90
11X-1, 0–150	98.00	106.50	10.00	0.48	0.43	0.10	47.37	0.06	0.00	0.07	81.89	84.54
14X-1, 0–150	126.80	135.30	20.36	0.56	0.85	0.11	40.98	0.00	0.00	0.09	69.79	73.13
17X-1, 0–150	155.70	164.20	11.77	0.36	0.45	0.13	46.65	0.00	0.00	0.07	81.22	83.26
18X-1, 0–150	165.00	173.50	17.95	0.37	0.52	0.08	42.67	0.00	0.00	0.06	74.70	76.14
19X-1, 0–150	174.20	182.70	11.30	0.37	0.44	0.13	46.80	0.00	0.00	0.10	81.98	83.53
20X-1, 0–150	183.80	192.30	17.63	0.43	0.78	0.14	42.36	0.00	0.00	0.08	73.60	75.59
21X-1, 0–150	193.50	202.00	43.39	0.36	0.41	0.05	26.87	0.75	0.01	0.04	46.95	47.95
22X-1, 0–150	203.10	211.60	41.45	0.34	0.40	0.06	28.05	0.51	0.00	0.04	48.39	50.06
23X-1, 0–150	212.80	221.30	22.05	0.35	0.41	0.10	39.58	0.03	0.00	0.06	69.63	70.64
24X-1, 0–150	222.50	231.00	17.16	0.29	0.42	0.06	44.21	0.00	0.00	0.07	75.97	78.90
25X-1, 0–150	232.10	240.60	22.88	0.33	0.86	0.11	39.26	0.46	0.00	0.05	68.95	70.06
27X-1, 0–150	251.00	259.50	24.97	0.41	2.00	0.18	35.88	1.00	0.01	0.04	63.20	64.03
28X-1, 0–150	260.70	269.20	16.25	0.39	0.78	0.20	44.20	0.00	0.00	0.06	77.24	78.88
29X-1, 0–150	270.30	278.80	10.02	0.39	0.69	0.15	47.58	0.00	0.00	0.07	83.58	84.90
30X-1, 0–150	279.90	288.40	9.67	0.44	0.85	0.17	48.47	0.00	0.00	0.07	83.42	86.49
31X-1, 0–150	289.60	298.10	18.62	0.49	0.96	0.21	42.36	0.00	0.00	0.07	73.01	75.60
32X-1, 60–62	299.80	307.56	13.46	0.63	1.26	0.17	45.03	0.00	0.00	0.10	78.34	80.35
33X-1, 81–83	309.71	317.47	35.38	0.53	0.87	0.19	32.00	0.31	0.00	0.05	55.67	57.11
34X-1, 127–129	319.87	327.63	31.97	0.85	2.14	0.29	32.05	0.35	0.01	0.11	56.17	57.20
35X-1, 86–88	329.06	336.82	21.24	0.56	1.52	0.27	40.29	0.00	0.00	0.11	69.96	71.91
36X-1, 60–62	338.40	346.16	64.79	0.48	1.08	0.16	14.73	1.61	0.07	0.02	25.63	26.28
36X-1, 70–72	338.50	346.26	91.23	0.35	0.26	0.05	2.34	0.00	0.00	0.00		4.17
37X-1, 44–46	347.94	355.70	10.90	0.72	1.61	0.28	45.95	0.00	0.00	0.13	80.20	82.00
38X-1, 28–30	357.38	365.14	31.21	0.57	1.09	0.25	34.55	0.51	0.01	0.06	60.83	61.65
38X-2, 63–66	359.23	366.99	86.66	0.35	0.55	0.06	4.60	0.00	0.00	0.00		8.21
38X-2, 133–136	359.93	367.69	82.42	0.29	0.24	0.07	7.25	0.00	0.00	0.00		12.93
39X-1, 40–42	367.20	374.96	36.92	0.46	1.92	0.16	29.87	0.65	0.02	0.06	52.87	53.31
40X-1, 41–43	376.81	384.57	10.73	0.41	0.90	0.21	45.87	0.00	0.00	0.16	83.42	81.85
41X-1, 43–47	386.53	394.29	15.53	0.47	2.11	0.12	43.05	0.00	0.00	0.11	75.63	76.83
42X-1, 45–47	396.25	404.01	20.43	0.38	1.51	0.12	41.68	0.00	0.00	0.07	72.67	74.38

$CaCO_3$ concentrations (wt%) measured by coulometry and estimated from the CaO concentration (see text).
LOI = loss on ignition.

Comparison of resistivity measurements to the geochemical logs makes it apparent that the interval of high Si, low Ca sediments is significantly larger than the chert interval (Fig. 58). High Si is found in the interval from 356 to 364.5 mbsf, and low Ca can be found between 357 and 363.5 mbsf. The low Ca, high Si interval is a poorly-laminated diatomaceous unit based upon core descriptions (see "Lithostratigraphy" section, this chapter). The chert layer at about 344 mbsf also occurs in a diatom-rich unit. In this hole, at least, the formation of chert is primarily controlled by lithology. Why other diatom-rich intervals didn't become chert has yet to be resolved.

Uranium Record and Natural Gamma-Ray Activity

The natural gamma-ray activity log from Hole 850B was marked by low-amplitude variations with wavelengths of several tens of meters. Most of the signal is due to uranium accumulation in the sediments and does not represent terrigenous detrital material. Figure 59 shows the natural gamma-ray activity plotted alongside the thorium and the uranium profiles for Hole 850B. Thorium in sediments is primarily associated with terrigenous detritus and gives an indication of the level of terrigenous contribution to the natural gamma ray activity in the sediments. Uranium has multiple sources, and can be enriched in sediments by the reduction and precipitation of seawater uranium in association with the degradation of organic carbon in the surface sediments. It can also be enriched in marine sediments by authigenic coprecipitation with ferromanganese oxides. For the latter to occur, however, there must be very low sedimentation rates and oxidizing conditions for high uranium contents to build up. There will also be a correlation between uranium and manganese content. Finally, there is a fraction of uranium associated with terrigenous detritus. In pelagic sediments, this fraction is a relatively small part of the total uranium content.

Because the sediments of Hole 850B are deposited relatively rapidly, most of the uranium has probably been fixed via reduction with organic carbon. We observe through the comparison in Figure 59 that the majority of the natural gamma-ray activity in Hole 850B is uranium-induced. There are distinct peaks we can identify associated with terrigenous deposition, shown by arrows on the figure, but the natural gamma-ray activity for the most part is correlated with uranium. Total natural gamma-ray activity cannot be used to estimate the terrigenous contribution to eastern equatorial Pacific sediments, unlike in other areas of the oceans.

The highest uranium activity in Hole 850B lies between 3.6 Ma (80 mbsf) and 5.1 Ma (159 mbsf), roughly when the site crosses the equator. The relationship between uranium and organic carbon deposition indicates that the element may prove useful in future paleoproductivity studies.

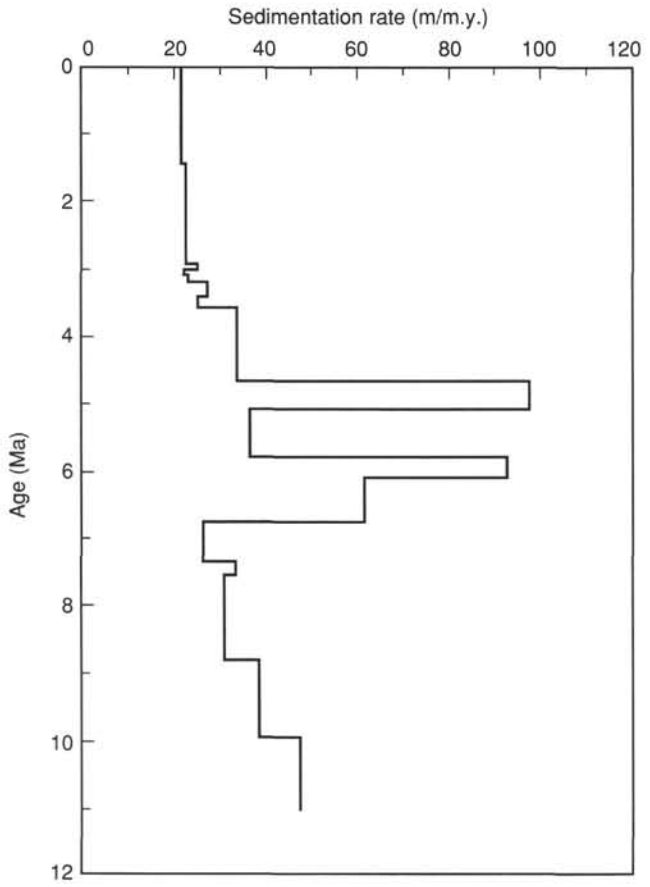

Figure 27. Linear sedimentation rate vs. age based on data in Table 10.

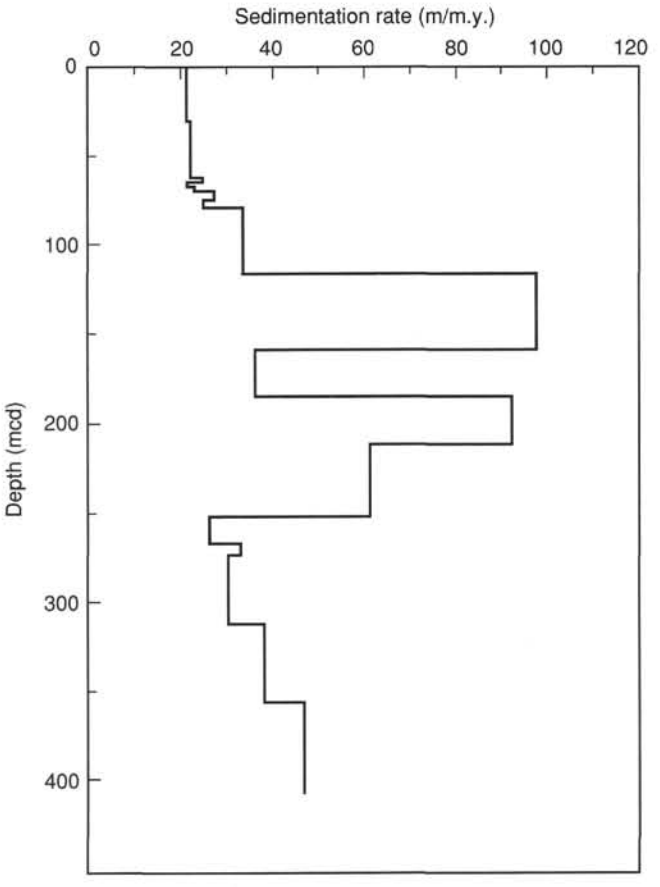

Figure 28. Linear sedimentation rate vs. composite depth based on data in Table 10.

Logs for Determining Coring Gaps in Hole 850B

Only one hole at Site 850 was drilled to basement (400 mbsf), and two APC sections were drilled to 74 and 96 mbsf, respectively. Without information from the logs, it was impossible to determine the continuity of the deeper sedimentary section. Figure 60 demonstrates that comparisons between GRAPE shipboard measurements and logging data can determine where overlaps and missing sections are located in the recovered core.

Figure 60A shows the GRAPE data and the density log plotted against the ODP-mbsf depth. Only a brief examination of the plot will convince one that the records are distorted with respect to the other. Figure 60B shows the same data shifted by appropriate intervals between cores to maximize the match between the records. The amount of shift is shown as an addition or subtraction after the core number. Most of the distortion between the two records can be removed by simple depth shifts of the cores. Little distortion occurs within cores, at least in this interval. Based on these shifts there are four gaps of 40–80 cm and three overlaps of 10–110 cm at the seven core breaks shown in the figure.

These offsets are similar in size to those found where the section could be spliced, above 74 mbsf. While it is impossible with a single core to ever sample these missing intervals the logs do provide the means to assess how much material has been lost and to build a gappy but continuous time series for XCB-cored Miocene and older sections.

SEISMIC STRATIGRAPHY

Modeling Procedure

Synthetic seismograms were generated from velocity and density models for Site 850 in order to correlate reflectors in the seismic section to stratigraphic changes.

The density model was created by merging laboratory density to *in-situ* logging density. To adjust the log-depth scale to core depths so ages can be assigned to reflectors found in the seismic record, density variations in Hole 850B GRAPE density over the interval 60.0–399.5 and logging density over the interval from 68.7 to 391.8 m were compared using the program CORPAC (Martinson et al., 1982). Over these intervals, a correlation of 0.72 was achieved and, ultimately, depth-shifted log density (by correlation with the Hole 850B GRAPE density) was used over the interval 70.2–391.4 m (70.9–391.4 mbsf) (see "Downhole Measurements" section, this chapter) for the composite model. Over the interval from 4.6 to 70.9 mbsf, a 10-point boxcar-filtered GRAPE density from Hole 850B was merged with the depth-shifted log density. Beyond 390.8 mbsf to the depth of basement (399.8 mbsf), a constant density of 1.63 g/cm^3 was used.

The velocity model was created in a similar manner as above. From 71.2 to 376.0 mbsf, depth-shifted logging velocities were used. To fill the gap in the upper part of the section, laboratory velocities collected with the DSV were corrected to *in-situ* conditions for changes of sound speed as a function of temperature and pressure. Because of problems in the temperature log, the temperature gradient of 7.8°C/km and bottom water temperature of 1.53°C determined for Site 849 were used. From 376.0 to 399.8 mbsf, a constant velocity of 1700 m/s was used.

The accuracy of the traveltime-to-depth conversion was evaluated by the generation of synthetic seismograms and the subsequent comparison to the seismic record collected over the site. Synthetic seismograms were generated using the merged velocity and density data described above. These data were resampled at a 1-ms sample interval (approximately 60 cm) and then used to calculate acoustic impedance and reflection coefficients and finally, a synthetic seismogram. Density and velocity values typical of basalt (2.5 g/cm^3 and 3000 m/s, respectively) were added at the basement depth to generate a base-

Table 14. Accumulation rates of SiO_2, Al_2O_3, Fe_2O_3, MnO, P_2O_5 and biogenic silica (opal).

Core, section, interval (cm)	Depth (mbsf) top	Depth (mcd) midpoint	Age (m.y.) midpoint	SiO_2 (mg/cm^2/k.y.)	Al_2O_3 (mg/cm^2/k.y.)	Fe_2O_3 (mg/cm^2/k.y.)	MnO (mg/cm^2/k.y.)	P_2O_5 (mg/cm^2/k.y.)	Opal (mg/cm^2/k.y.)
1H-1, 0–150	0.00	0.75	0.04	145	7	5	2.1	0.8	123
1H-1, 0–150	3.00	3.75	0.18	231	11	14	3.4	1.4	198
2H-1, 0–150	7.70	10.00	0.47	252	13	8	1.6	1.0	214
3H-1, 0–150	17.20	19.60	0.92	105	9	7	1.3	1.0	79
4H-1, 0–150	26.70	30.45	1.43	174	9	8	1.5	1.0	147
5H-1, 0–150	36.20	40.75	1.89	184	11	10	2.2	1.0	150
6H-1, 0–150	45.70	52.20	2.41	246	10	10	2.1	0.9	216
7H-1, 0–150	55.20	63.30	2.90	151	9	12	3.0	1.1	123
8H-1, 0–150	64.70	74.45	3.36	237	14	19	4.6	1.6	194
9H-1, 0–150	69.50	78.00	3.49	171	13	17	4.5	1.3	132
10H-1, 0–150	88.50	97.00	4.07	628	11	10	2.8	1.3	595
11X-1, 0–150	98.00	106.50	4.36	224	11	10	2.1	1.6	192
14X-1, 0–150	126.80	135.30	4.85	1338	37	56	7.2	6.0	1228
17X-1, 0–150	155.70	164.20	5.23	322	10	12	3.7	1.8	292
18X-1, 0–150	165.00	173.50	5.48	492	10	14	2.1	1.7	461
19X-1, 0–150	174.20	182.70	5.74	310	10	12	3.6	2.6	279
20X-1, 0–150	183.80	192.30	5.88	1033	25	45	8.2	4.8	958
21X-1, 0–150	193.50	202.00	5.98	2541	21	24	3.0	2.2	2478
22X-1, 0–150	203.10	211.60	6.09	2428	20	24	3.4	2.1	2369
23X-1, 0–150	212.80	221.30	6.25	944	15	18	4.3	2.4	898
24X-1, 0–150	222.50	231.00	6.41	734	12	18	2.7	3.0	697
25X-1, 0–150	232.10	240.60	6.57	979	14	37	4.8	2.2	937
27X-1, 0–150	251.00	259.50	7.06	521	9	42	3.7	0.9	495
28X-1, 0–150	260.70	269.20	7.43	261	6	13	3.2	1.0	242
29X-1, 0–150	270.30	278.80	7.77	256	10	18	3.8	1.8	226
30X-1, 0–150	279.90	288.40	8.06	247	11	22	4.3	1.9	213
31X-1, 0–150	289.60	298.10	8.35	475	12	24	5.4	1.8	438
32X-1, 60–62	299.80	307.56	8.64	343	16	32	4.3	2.5	295
33X-1, 81–83	309.71	317.47	8.92	821	12	20	4.4	1.1	784
34X-1, 127–129	319.87	327.63	9.18	742	20	50	6.7	2.6	683
35X-1, 86–88	329.06	336.82	9.42	493	13	35	6.2	2.6	454
36X-1, 60–62	338.40	346.16	9.67	1504	11	25	3.6	0.6	1470
36X-1, 70–72	338.50	346.26	9.67	2117	8	6	1.1	0.0	2093
37X-1, 44–46	347.94	355.70	9.92	253	17	37	6.5	3.1	203
38X-1, 28–30	357.38	365.14	10.12	1040	19	36	8.3	2.1	982
38X-1, 63–66	359.23	366.99	10.16	2887	12	18	2.1	0.0	2852
38X-1, 133–136	359.93	367.69	10.18	2746	10	8	2.3	0.0	2717
39X-1, 40–42	367.20	374.96	10.33	1230	15	64	5.3	1.9	1184
40X-1, 41–43	376.81	384.57	10.53	357	14	30	7.1	5.3	316
41X-1, 43–47	386.53	394.29	10.74	517	16	70	4.0	3.8	471
42X-1, 45–47	396.25	404.01	10.95	680	13	50	4.1	2.4	642

ment reflector in the synthetic. As before, the model used to generate the synthetic seismogram assumes plane waves, no multiples, and no signal attenuation; the model is described in Mayer et al. (1985). The final synthetic seismogram was filtered from 70 to 250 Hz., the same filter parameters as the field record collected on the 850 site survey.

Results

A comparison of the synthetic seismogram with the seismic profile collected at Site 850 shows a good match between the two (Fig. 61). A nearly one-to-one correspondence exists between reflectors with an excellent match at basement. This suggests that the traveltime-to-depth conversion is accurate.

Given an acceptable velocity model, the origin of some of the reflectors at Site 850 can be analyzed. We emphasize that these are preliminary results that will undoubtedly be modified after more careful analysis. Nineteen major reflectors or reflector packages were identified. These reflectors were selected on the basis of amplitude and lateral coherency in the seismic record in the immediate area of Site 850. The two-way traveltime on the synthetic seismogram of the top and bottom of each reflector was measured, and by using the assumed velocity model, the depth range of each reflector was determined.

The velocity, density, and acoustic impedance models were compared to the depth ranges calculated from the traveltime to determine the changes in physical properties causing the selected seismic reflectors. In general, within 2 m of each calculated depth range, a large change in density and/or velocity can be associated with each reflector (Fig. 62). Reflectors for the upper 95 m (reflectors 1–5) are solely related to large changes in density. Beyond 95 m, the reflectors are due to synchronous, large fluctuations in velocity and density, although the amplitude of the density fluctuations was generally larger. The depths (synthetic, mbsf, and mcd) and ages (based on magnetostratigraphy and biostratigraphy of Site 850; see 'Sedimentation Rates' section, this chapter) of these reflectors are presented in Table 24. A detailed understanding of the lithological, biostratigraphic and, ultimately, the paleoceanographic significance of these events must await shore-based studies at this time.

SUMMARY AND CONCLUSIONS

Built into any drilling plan must be contingency time to allow for bad weather and equipment failure. We were fortunate during Leg 138 to have neither equipment nor weather problems and this fact, combined with the skill and hard work of the SEDCO and ODP crews, enabled us to drill a complete extra site. Site 850 was chosen as the extra site because of its location just north of the Equator and its position halfway between Sites 849 and 851. Recent physical and biological oceanographic studies have demonstrated that the equatorial divergence zone has very steep and strong gradients, particularly in surface productivity. Given the success we have had at previous sites in correlating the high-resolution

Table 15. Averages values of sedimentary parameters calculated over time intervals defined by chronostratigraphic levels.

Composite depth (mcd)	Age (Ma)	Mean $CaCO_3$ (%)	Mean C_{org} (%)	Sed. Rate (m/m.y.)	Mean DBD (g/cm^3)	Mean Bulk MAR ($g/cm^2/k.y.$)	Mean $CaCO_3$ MAR ($g/cm^2/k.y.$)	Mean Non-$CaCO_3$ MAR ($g/cm^2/k.y.$)	Mean C_{org} MAR ($mg/cm^2/k.y.$)
0.00	0.00								
30.94	1.45	76.10	0.13	21.34	0.59	1.27	0.97	0.30	1.68
63.66	2.92	72.58	0.15	22.26	0.57	1.26	0.91	0.35	1.93
65.40	2.99	60.86	0.23	24.86	0.50	1.23	0.75	0.48	2.77
67.36	3.08	65.88		21.78	0.51	1.11	0.73	0.38	
69.65	3.18	79.70		22.90	0.50	1.13	0.90	0.23	
75.67	3.40	69.63	0.19	27.36	0.61	1.66	1.16	0.50	3.12
80.00	3.56	71.56	0.26	27.06	0.60	1.62	1.16	0.46	4.22
116.65	4.66	71.19	0.16	33.32	0.67	2.24	1.60	0.65	3.65
159.65	5.10	68.12	0.14	97.73	0.67	6.57	4.48	2.09	9.23
185.00	5.80	74.82	0.10	36.21	0.76	2.74	2.05	0.69	2.64
212.78	6.10	61.47	0.09	92.60	0.63	5.86	3.60	2.26	5.04
250.90	6.75	70.55	0.12	58.65	0.73	4.28	3.02	1.26	4.94
267.40	7.35	71.85	0.10	27.50	0.76	2.09	1.50	0.59	1.99
271.68	7.55	72.16	0.09	21.40	0.75	1.61	1.16	0.45	1.49
313.00	8.80	71.70	0.10	33.06	0.77	2.55	1.83	0.72	2.66
356.60	9.94	50.20	0.11	38.25	0.61	2.32	1.16	1.16	2.63
387.70	10.60	58.98	0.15	47.12	0.71	3.33	1.96	1.37	4.93

DBD = Dry bulk density; MAR = Mass accumulation rate.

Note: After this table was constructed onboard, changes were made to the depths of the age control points (see "Sedimentation Rates" section, this chapter, for the final selection of age control points). These depth changes are often minor (less than 5m). None of these changes have been incorporated in this table nor in the accompanying Figures 42, 43, and 44.

For a discussion, see "Sedimentation Rates" section, this chapter. The parameters are $\%CaCO_3$, $\%C_{org}$, DBD, LSR, Bulk MAR, $CaCO_3$, MAR, non-$CaCO_3$ MAR (calculated as 100%– $\%CaCO_3$) and C_{org} MAR.

continuous core logs collected on board the ship (GRAPE density, susceptibility, and color reflectance), we felt that it would be possible to evaluate, with sufficient resolution, the spatial and temporal history of these steep equatorial gradients.

Site 850 is located about 900 km west of the East Pacific Rise on crust generated about 11–12 Ma. The backtrack path of the site is straightforward, constrained by the movement of the Pacific Plate, as reconstructed from traces of hot spots and distribution of sediments (van Andel et al., 1975; see Fig. 2), although some controversy does exist over the appropriate pole of rotation. From an original ridge-crest depth of approximately 2800 m, the site has subsided to its present depth of 3800 m. The backtrack path of van Andel et al. (1975) would suggest that Site 850 crossed under the narrow equatorial divergence zone approximately 4 Ma, while that of Duncan and Clague (1985) suggests an equatorial crossing at about 6 Ma.

The time available for drilling Site 850 permitted only double APC-coring to 74 mbsf; the rest of the section (74–399.8 m) was single APC- and XCB-cored. The section is predominantly diatom nannofossil ooze with varying proportions of other microfossil constituents. Because much of the section was sampled with only single APC- or XCB-cored, it is inevitable that minor gaps occur in the section recovered. However, a complete suite of logs was collected and between the downhole logs and the laboratory core measurements (GRAPE, color, and susceptibility) collected at nearby sites, we hope to estimate the extent of the missing intervals and, if possible, to fill these gaps (with downhole logging data).

Site 850 is only 100 km north of Site 849; thus, its sedimentation history generally is similar to that of Site 849. The temporal and spatial differences, however, are what provide information about the history of the divergence-driven gradients. The first sediment to accumulate above the newly formed basement at Site 850 was a nannofossil ooze containing a substantial component of iron oxides and clays. Initial sedimentation rates at the site are around 50 m/m.y. As with many sites in the equatorial region, sedimentation rates decrease after 10 Ma, in part reflecting the subsidence of the site away from the ridge crest (Fig. 63A). Between 10.5 and 9.5 Ma, sedimentation was characterized by generally high carbonate, noncarbonate, and organic carbon accumulation and sedimentation rates of approximately 40 m/m.y. The sediments in this interval are radiolarian and diatom nannofossil oozes, with several distinctive layers of laminated diatom ooze and thinly bedded chert. These thin chert layers were clearly imaged on the FMS log, which indicated that four very thin (centimeter scale) chert horizons existed. Three of these were recovered in place with the XCB.

The chert layers appear to have a dramatic effect on the interstitial water chemistry, dividing the section into two distinct zones. Above the cherts, microbial degradation of organic matter consumes sulfate, generating concave-downward and concave-upward profiles of sulfate and alkalinity, respectively. Below the chert, both sulfate and alkalinity return to seawater values. Ammonia decreases 22-fold across this boundary while potassium is invariant. Magnesium and calcium decrease downhole and silica increases with depth, consistent with reaction with biogenic silica. The silica trend reverses below the chert boundary, decreasing into basement but without a dramatic shift within the chert zone. The absence of a pore water signal associated with the chert suggests that these chert layers are relict. Analysis of methane gas concentration shows that an abrupt increase occurs at about 130 mbsf, below which concentrations increase by a factor of three. This decrease in gas concentration was not mirrored by a change in organic carbon content of the sediment, but interestingly, was found in the part of the sediment section deposited after the site migrated away from the Equator. Understanding of this coincidence will require future research.

Between about 9.5 and 8.5 Ma, an interval of relatively constant sedimentation rate, carbonate and organic carbon accumulation rates are relatively low. Noncarbonate accumulation rates, however, are relatively high, suggesting increased influx of clay. Elevated susceptibility values (Fig. 63B) and decreased carbonate content support the suggestion of increased clay flux. Sedimentation rates slowly decrease between about 9 and 7 Ma, after which a large increase occurs in sedimentation (to more than 90 m/m.y.) and accumulation rates (Fig. 63A). During this time interval, the noncarbonate accumulation rate, which was dominated by biogenic silica, increased proportionally more than the carbonate accumulation rate and the carbonate content decreased sharply, implying a productivity event with the associated dilution and enhanced dissolution of carbonate. Each of the previous western transect sites (848 and 849) showed a similar increase in sedimentation and accumulation rates at this time.

A sharp decrease in sedimentation and accumulation rates occurred between 6 and 5 Ma (a feature shared with Site 849 but not

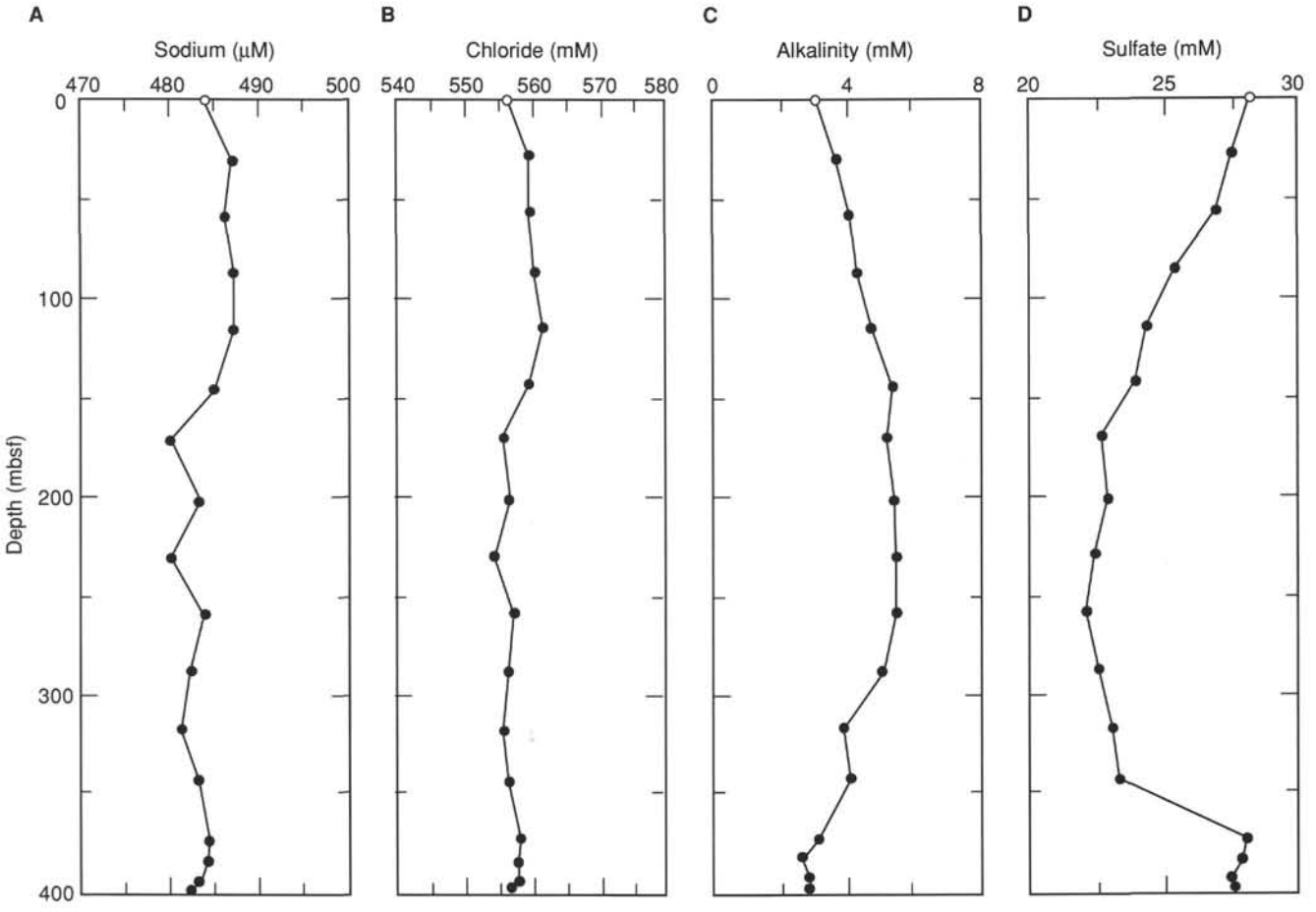

Figure 29. Interstitial-water geochemical data with sub-bottom depths (mbsf) for Holes 850A (open circle) and 850B (solid circles). **A.** Sodium. **B.** Chloride. **C.** Alkalinity. **D.** Sulfate.

Site 848) and then another increase to sedimentation rates as high as 100 m/m.y. between 5 and 4.5 Ma. Noncarbonate accumulation rates, again presumably reflecting biogenic silica, also increased during this interval, but not to the levels observed at 7 Ma. Carbonate accumulation rates over the interval are high, but when viewed at extremely high resolution, the carbonate curve can be seen to fluctuate rapidly between about 50% and 90% carbonate (Fig. 63C). Sedimentation rates decrease to about 30 m/m.y. at 4 Ma, the time at which Site 850 has been estimated to be directly under the equatorial divergence. While a decline in sedimentation rate coincident with the equatorial crossing may seem surprising, when viewed in a regional and temporal context, it is clear that temporal fluctuations in sediment accumulation far outweigh the influence on sediment accumulation of the passage of the site under the Equator. In addition, the evaluation of how the equatorial divergence affects sedimentation along this transect is complicated by two factors: (1) the resolution of the sedimentation rate curves, based on initial biostratigraphy, is much lower than can be achieved using stratigraphies based on high-resolution data sets (e.g., GRAPE sediment densities) that were collected during the cruise. A more detailed pattern of spatial and temporal sedimentation will emerge as part of post-cruise studies, and (2) uncertainty as to the appropriate pole of rotation to use for the Pacific Plate still exists. The van Andel et al. (1975) rotation pole (Table 25) is based on low-resolution stratigraphic determination of the zone of maximum sediment accumulation, while more recent poles, such as that of Duncan and Claque (1985), have been based on hot-spot reference frames. These poles differ as to the time when the sites along the 110°W transect crossed the equatorial zone by as much as 2 m.y. More importantly, however, the gradient between Sites 850 and 849 is apparent in the available data, suggesting that, indeed, the geologic record does record the high gradients of the equatorial Pacific Ocean.

As at most high-sedimentation-rate, pelagic, equatorial sites, the paleomagnetic signal at Site 850 was, for the most part, too weak to produce a measurable stratigraphy. Surprisingly, a brief interval (3.4–2.9 Ma) showed a strong and coherent pattern, with five reversals spanning the Kaena subchron to the Gauss/Gilbert boundary. The origin of this strong magnetic signal is, at present, not understood. Unlike other sites that have shown strong magnetic signals, neither anomalous sedimentation rates nor a change in redox conditions are associated with this interval at Site 850.

Site 850 was an "extra" site drilled in an attempt to delineate the spatial and temporal variations in the narrow high-productivity zone associated with divergence on the Equator. The ultimate success of this experiment must await both high-resolution stratigraphic studies as well as studies of the biologic response to these gradients as recorded in the planktonic fossils preserved in the pelagic sediments of the equatorial region.

REFERENCES

Baker, P. A., 1986. Pore water chemistry of carbonate-rich sediments, Lord Howe Rise, Southwest Pacific Ocean. *In* Kennett, J. P., von der Borch, C. C., et al., *Init. Repts. DSDP*, 90: Washington (U.S. Govt. Printing Office), 1249–1256.

Baker, P. A., Gieskes, J. M., and Elderfield, H., 1982. Diagenesis of carbonates in deep-sea sediments-evidence from Sr/Ca ratios and interstitial dissolved Sr^{2+} data. *J. Sediment. Petrol.*, 52:71–82.

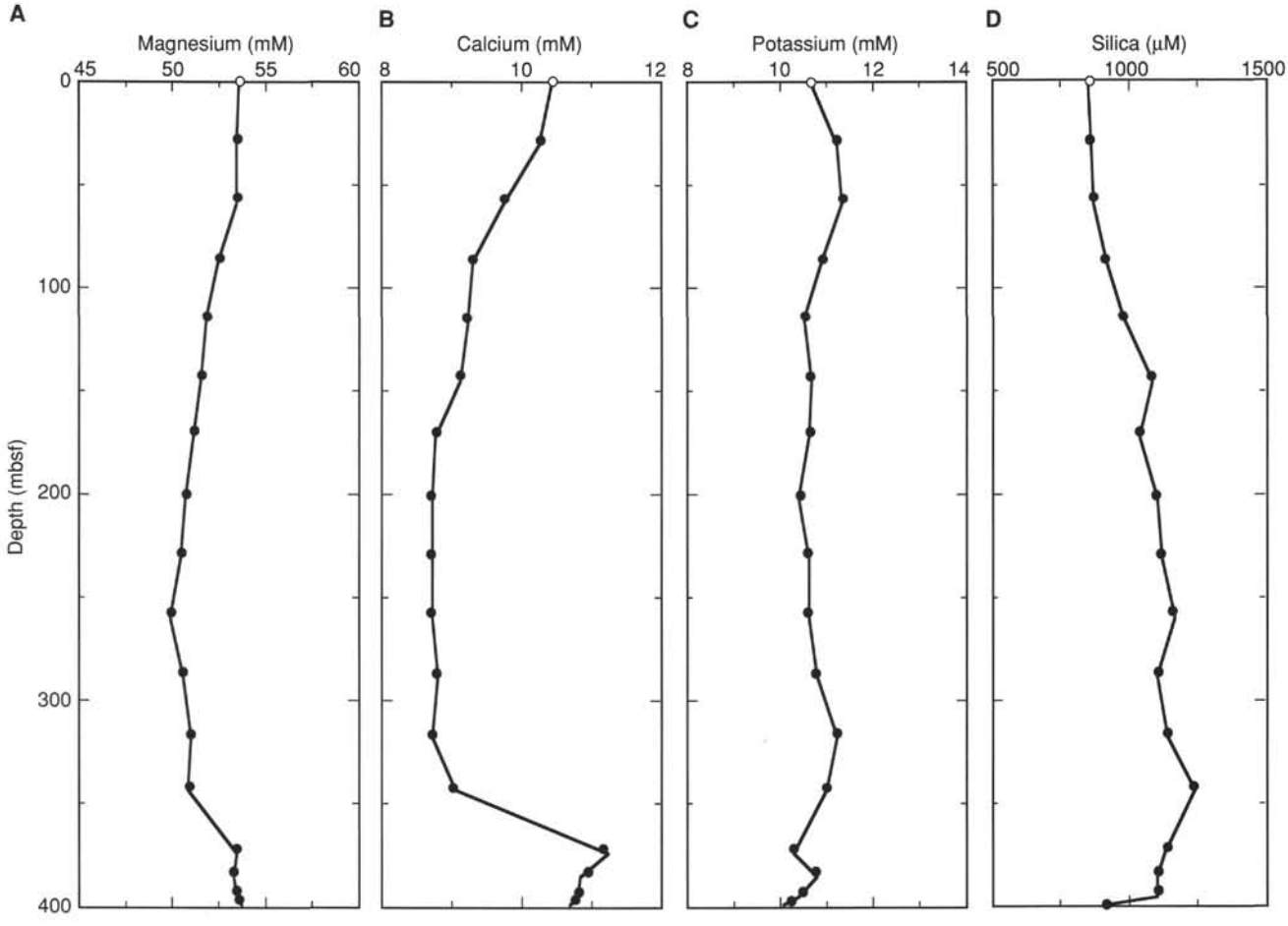

Figure 30. Interstitial-water geochemical data with sub-bottom depths (mbsf) for Holes 850A (open circle) and 850B (solid circles). **A.** Magnesium. **B.** Calcium. **C.** Potassium. **D.** Silica.

Baas Becking, L.G.M., and Moore, D., 1959. Density distribution in sediments. *J. Sediment. Petrol.,* 29:45–55.

Brocker, W. S., and Peng, T. H., 1982. *Tracers in the Sea:* Palisades, NY (Eldigio Press).

Bullard, E. C., 1963. The flow of heat through the floor of the ocean. *In* Hill, M. N. (Ed.), *The Sea* (Vol. 3): New York (Wiley), 218–232.

Chavez, F. P., and Barber, R. T., 1987. An estimate of new production in the equatorial Pacific. *Deep-Sea Res. Part A,* 34:1229–1243.

Claypool, G. E., and Kaplan, I. R., 1974. The origin and distribution of methane in marine sediments. *In* Kaplan, I. R. (Ed.), *Natural Gases in Marine Sediments.* Mar. Sci., 3:99–140.

Duncan, R., and Claque, D., 1985. Pacific plate motion is recorded by linear volcanic chains. *In* Nairn, A.E.M., Stehli, F. G., and Uyeda, S. (Eds.), *The Ocean Basins and Margins* (Vol. 7A): *The Pacific Ocean:* New York (Plenum), 89–121.

Dymond, J., 1981. The geochemistry of Nazca Plate sediments: an evaluation of hydrothermal, biogenic, detrital, and hydrogenous sources. *In* Kulm, L. D., Dymond, J., Dasch, D. M., and Hussong, D. M. (Eds.), *Nazca Plate: Crustal Formation and Andean Convergence.* Mem.—Geol. Soc. Am., 154:133–174.

Elderfield, H., and Gieskes J. M., 1982. Sr isotopes in interstitial waters of marine sediments from Deep Sea Drilling Project cores. *Nature,* 333:493–497.

Froelich, P. N., Bender, M. L., and Heath, G. R., 1977. Phosphorus accumulation rates in metalliferous sediments on the East Pacific Rise. *Earth Planet Sci. Lett.,* 34:351–359.

Gieskes, J. M., 1974. Chemistry of interstitial waters of marine sediments. *Annu. Rev. Earth Planet. Sci.,* 3:433–394.

———, 1983. The chemistry of interstitial waters of deep sea sediments: interpretation of deep sea drilling data. *In* Riley, J. P., and Chester, R. (Eds.), *Chemical Oceanography* (Vol.8): London (Academic Press), 221–269.

Gieskes, J. M., Elderfield, H., and Palmer, M. R., 1986. Strontium and its isotopic composition in interstitial waters of marine carbonate sediments. *Earth Planet. Sci. Lett.,* 77:229–235.

Harrison, W. E., Hesse, R., and Gieskes, J. M., 1982. Relationship between sedimentary facies and interstitial water chemistry of slope, trench, and Cocos Plate sites from the Middle America Trench transect, active margin off Guatemala, Deep Sea Drilling Project Leg 67. *In* Aubouin, J., von Huene, R., et al., *Init. Repts. DSDP,* 67: Washington (U.S. Govt. Printing Office), 603–613.

Heath, G. R., and Dymond, J., 1977. Genesis and transformation of metalliferous sediments from the East Pacific Rise, Bauer Deep and Central Basin, Northwest Nazca Plate. *Geol. Soc. Am. Bull.,* 88:723–733.

Hill, P. R., and Marsters, J. C., 1990. Controls on physical properties of Peru continental margin sediments and their relationship to deformation styles. *In* Suess, E., von Huene, R., et al., *Proc. ODP, Sci. Results,* 112: College Station, TX (Ocean Drilling Program), 623–632.

Isern, A. R., 1991. Calcium carbonate and organic carbon accumulation in the central equatorial Pacific [M.S. thesis]. Univ. of Rhode Island.

JGOFS, 1991. Report of a workshop on equatorial Pacific process studies, Tokyo. *JGOFS, SCOR,* Rep. 8.

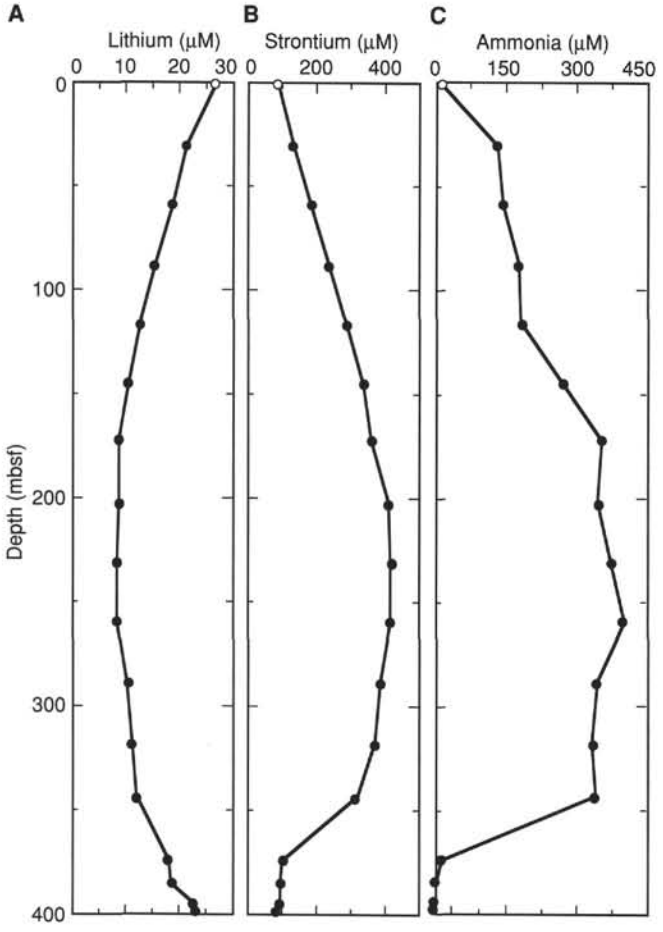

Figure 31. Interstitial-water geochemical data with sub-bottom depths (mbsf) for Holes 850A (open circle) and 850B (solid circles). **A.** Lithium. **B.** Strontium. **C.** Ammonia.

Johnson, D. A., and Nigrini, C. A., 1985. Synchronous and time-transgressive Neogene radiolarian datum levels in the equatorial Indian and Pacific Oceans. *Mar. Micropaleontol.*, 9:489–523.

Kastner, M., 1981. Authigenic silicates in deep-sea sediments: formation and diagenesis. *In* Emiliani, C. (Ed.) *The Sea* (Vol.7): *The Oceanic Lithosphere:* New York (Wiley), 915–980.

Leinen, M., 1977. A normative calculation technique for determining opal in deep-sea sediments. *Geochim. Cosmochim. Acta,* 41:671–676.

————, 1979. Biogenetic silica accumulation in the central equatorial Pacific and its implications for Cenozoic Paleoceanography. *Geol. Soc. Am. Bull.,* 90 (Pt. 2): 1310–1376.

Leinen, M., and Stakes, D., 1979. Metal accumulation rates in Cenozoic sediments from the central equatorial Pacific. *Geol. Soc. Am. Bull.,* 90:357–275.

Lyle, M., 1986. Major element composition of Leg 92 sediments. *In* Leinen, M., Rea, D. K., et al., *Init. Repts. DSDP,* 92: Washington (U.S. Govt. Printing Office), 355–370.

Mammerickx, J., 1989. The Eastern Pacific Ocean and Hawaii. *In* Winterer, E. L., et al. (Eds.), *The Geology of North America* (Vol. N). Geol. Soc. Am.

Martini, E., 1971. Standard Tertiary and Quaternary calcareous nannoplankton zonation. *Proc. 2nd Planktonic Conf. Roma.* Rome (Ed. Tecnosci.), 739–785.

Martinson, D. G., Menke, W., and Stoffa, P., 1982. An inverse approach to signal correlation. *J. Geophys. Res.,* 87:4807–4818.

Mayer, L., 1991. Extraction of high-resolution carbonate data for paleoclimate reconstruction. *Nature,* 352:148–151.

Mayer, L. A., 1979. The origin of fine scale acoustic stratigraphy in deep-sea carbonates. *J. Geophys. Res.,* 84:6177–6184.

Mayer, L. A., Shipley, T. H., Theyer, F., Wilkens, R. W., and Winterer, E. L., 1985. Seismic modelling and paleoceanography at DSDP Site 574. *In* Mayer, L. A., Theyer, F., Thomas, E., et al., *Init. Repts. DSDP,* 85: Washington (U.S. Govt. Printing Office), 947–970.

McDuff, R. E., 1981. Major cation gradients in DSDP interstitial waters: the role of diffusive exchange between seawater and the upper ocean crust. *Geochim. Cosmochim. Acta,* 45:1705–1713.

Okada, H., and Bukry, D., 1980. Supplementary modification and introduction of code numbers to the low-latitude coccolith biostratigraphic zonation (Bukry, 1973; 1975). *Mar. Micropaleontol.,* 5:321–325.

Stout, P. M., 1985. Interstitial water chemistry and diagenesis of biogenic sediments from the eastern equatorial Pacific, Deep Sea Drilling Project Leg 85. *In* Mayer, L., Theyer, F., Thomas, E., et al., *Init. Repts. DSDP,* 85: Washington (U.S. Govt. Printing Office), 805–820.

van Andel, T. J., Heath, G. R., and Moore, T. C., Jr., 1975. Cenozoic tectonics, sedimentation, and paleoceanography of the central equatorial Pacific. *Mem.—Geol. Soc. Am.,* 143.

Ms 138A-115

NOTE: For all sites drilled, core description forms ("barrel sheets") and core photographs have been reproduced on coated paper and can be found in Section 8, beginning on page 1099. Forms containing smear-slide data can be found in Section 9, beginning on page 1435.

Formation microscanner images for this site are presented on microfiche in the back of Part 2.

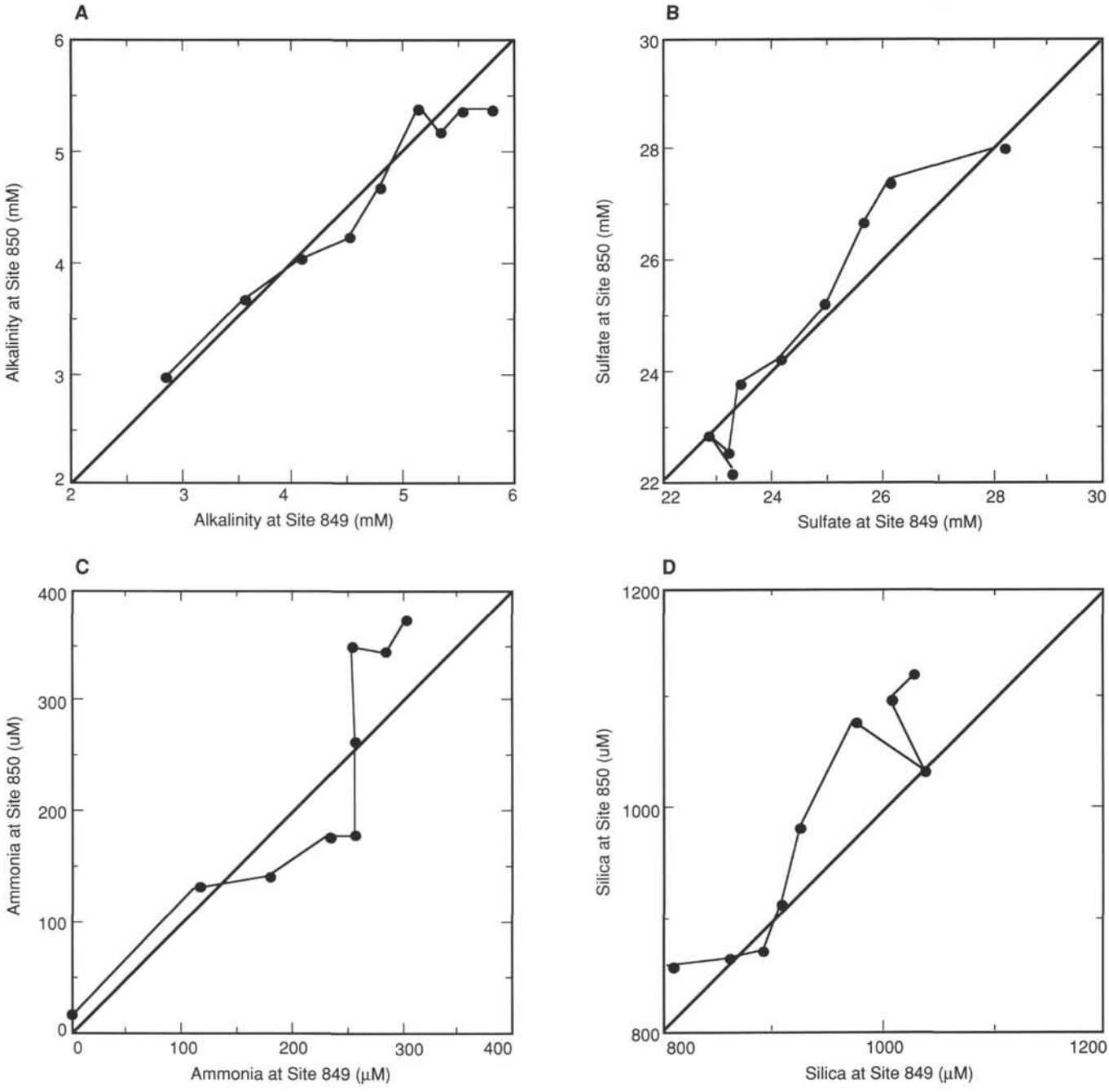

Figure 32. Concentrations of interstitial water from Site 850 plotted vs. results from Site 849. Diagonal line represents a 1:1 correlation. **A.** Alkalinity. **B.** Sulfate. **C.** Ammonia. **D.** Silica.

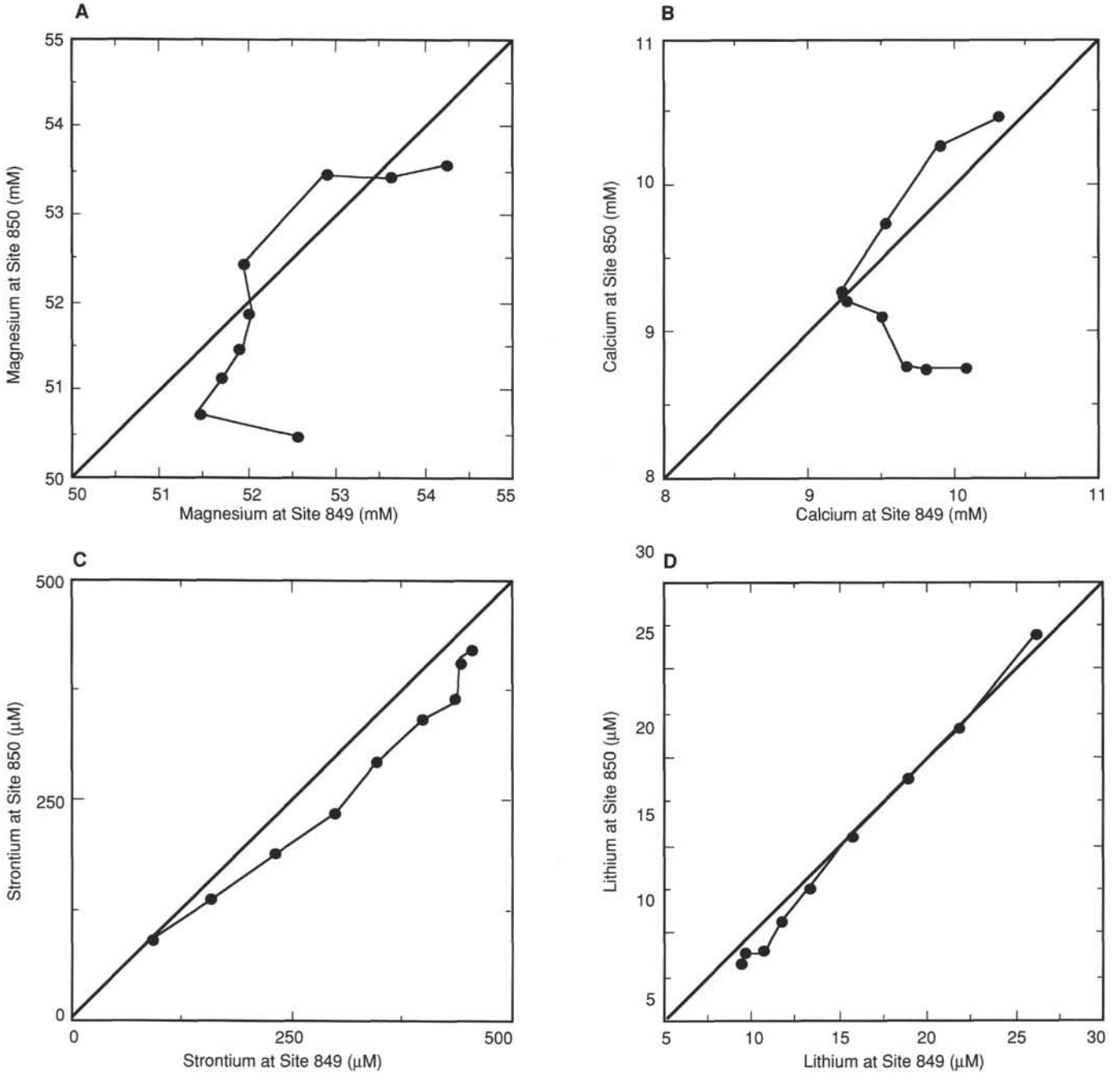

Figure 33. Concentrations of interstitial water from Site 850 plotted vs. results from Site 849. Diagonal line represents a 1:1 correlation. **A.** Magnesium. **B.** Calcium. **C.** Strontium. **D.** Lithium.

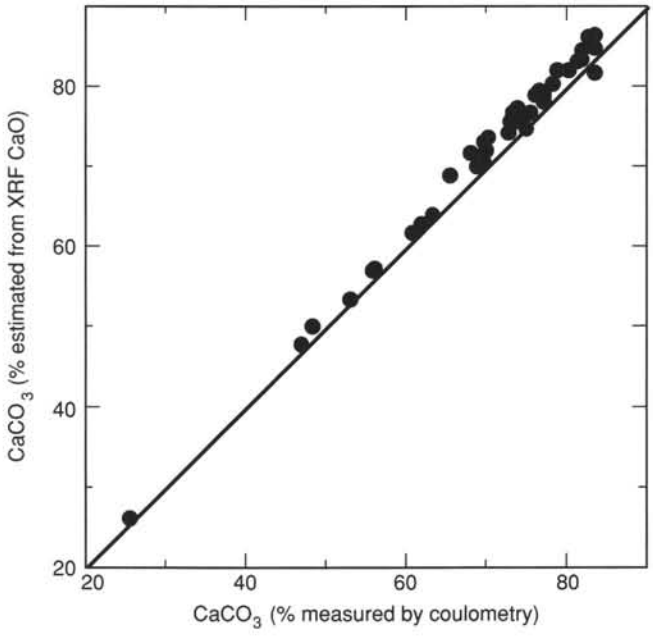

Figure 34. Concentration of $CaCO_3$ estimated from XRF CaO concentrations vs. $CaCO_3$ measured by coulometry.

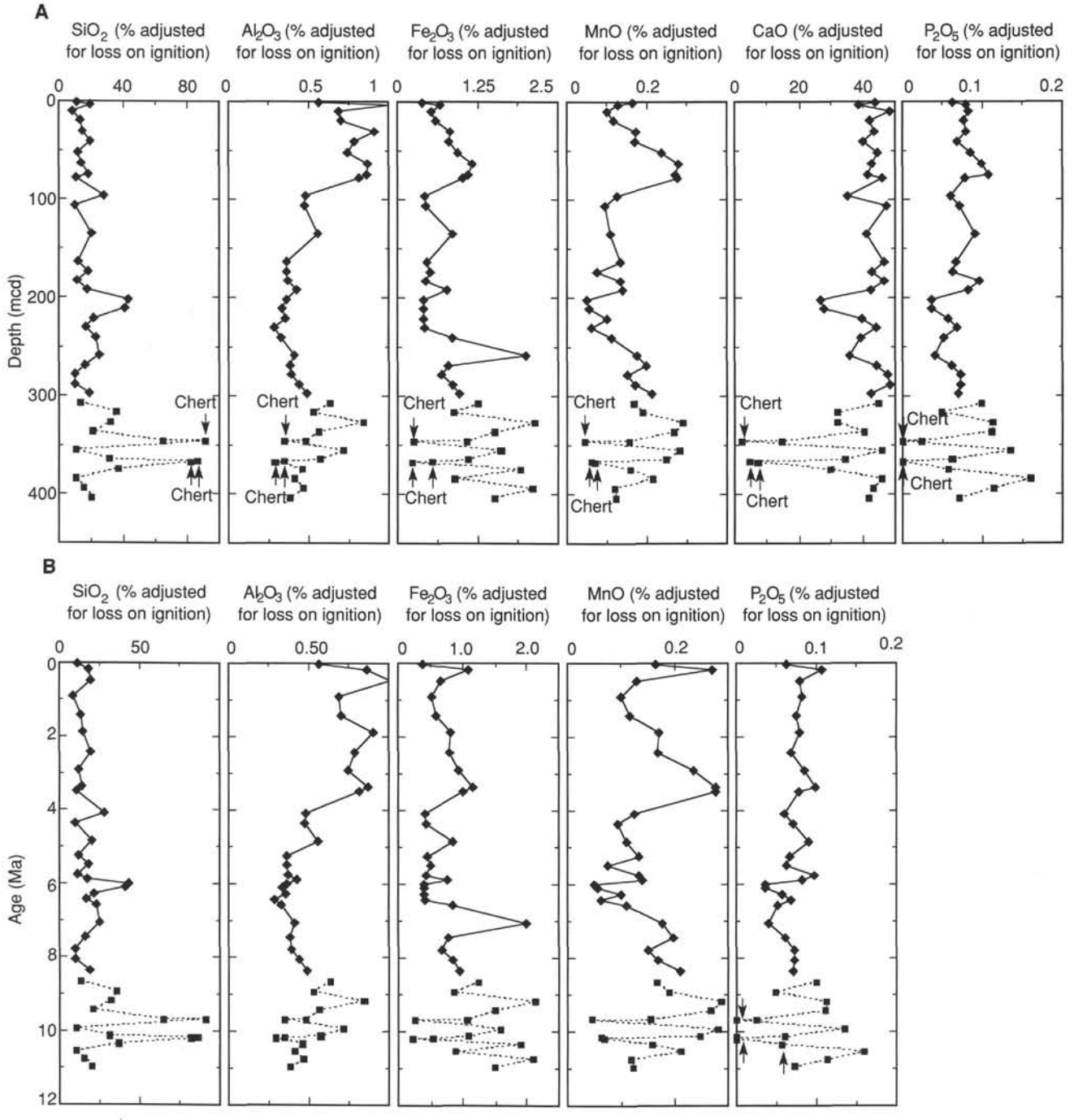

Figure 35. **A.** Weight percent SiO_2, Al_2O_3, Fe_2O_3, MnO, CaO and P_2O_5 in bulk sediment from Site 850 calculated assuming that all loss on ignition is a result of loss of CO_2 from carbonate. Concentrations are plotted vs. composite depth (mcd) to combine data from Hole 850A with those from Hole 850B. **B.** Weight percent SiO_2, Al_2O_3, Fe_2O_3, MnO, and P_2O_5 in bulk sediment from Site 850 calculated assuming that all loss on ignition is caused by loss of CO_2 from carbonate plotted as a function of age (Ma).

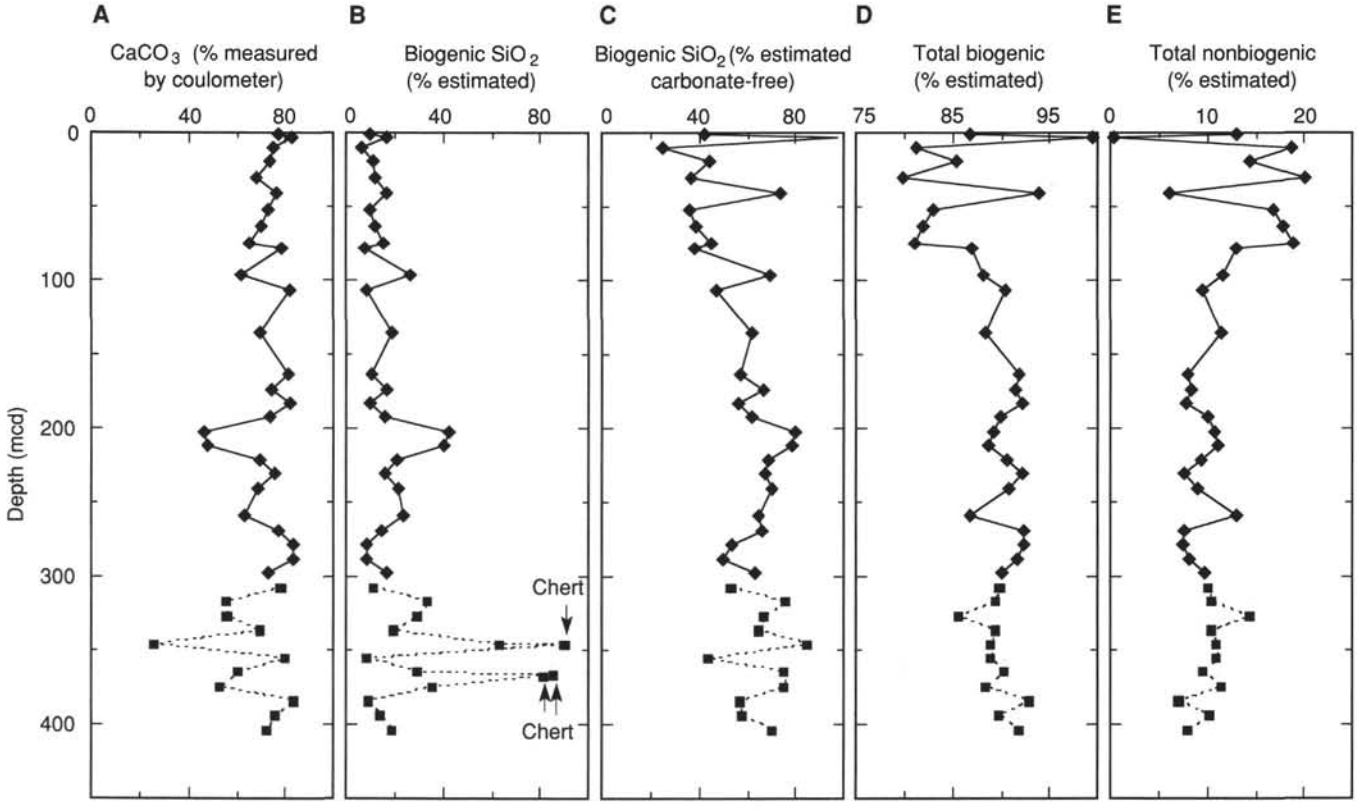

Figure 36. **A.** Weight percent of $CaCO_3$ measured by coulometry. **B.** Estimated concentration of biogenic SiO_2 (wt%) assuming a terrigenous SiO_2/Al_2O_3 of 3.0. **C.** Biogenic SiO_2 (wt%) calculated on a calcium carbonate-free basis. **D.** Total of biogenic components (= estimated wt% $CaCO_3$ + estimated wt% biogenic SiO_2). **E.** Nonbiogenic components (wt%). Note: no $CaCO_3$ data were available for the cherts. They are not included in this figure.

Table 23. Well log data, Hole 850B.[a]

Log type	Depth (mbsf)
Resistivity	77.8–401.0
Bulk density	70.3–393.1
Sonic velocity	58.6–381.1
Sonic waveforms	58.6–381.1
Gamma ray/U-Th-K	00.0–388.5
Aluminum	00.0–390.3
Geochemistry	00.0–398.1
Caliper	88.5–395.7
Formation microscanner	88.5–395.7
LDGO temperature	none

[a]Assumes seafloor at 3797.8 mbrf and with all logs correlated and depth shifted to GRAPE data on the cores (Geophys = +1.42 m; FMS = -0.86 m; Chem = -0.18 m).

Table 24. Summary of traveltimes, depths, and ages for Site 850 reflectors.

Reflector	Traveltime (s)	Synthetic depth (m)	Depth (mbsf)	Depth (mcd)	Age (Ma)
R1	0.062	46.80	46.50	50.95	2.35
	0.065	49.00	50.10	54.55	2.51
R2	0.074	55.80	57.80	63.25	2.90
	0.081	61.10	60.50	67.10	3.07
R3	0.090	68.00	67.60	74.20	3.35
	0.095	71.80	71.70	79.45	3.55
R5	0.123	93.10	91.00	98.75	4.13
	0.127	96.20	94.40	102.15	4.23
R6	0.133	100.80	98.00	105.75	4.34
	0.141	107.20	104.70	112.45	4.54
R7	0.143	108.80	110.20	117.95	4.67
	0.148	112.80	115.20	122.95	4.72
R11	0.182	187.70	138.40	146.15	4.96
	0.187	142.70	142.70	150.45	5.01
R13	0.207	158.50	157.10	164.85	5.24
	0.211	161.80	160.70	168.45	5.34
R14	0.228	175.80	176.00	183.75	5.77
	0.231	178.80	179.00	186.75	5.81
R16	0.245	189.60	189.50	197.25	5.90
	0.248	192.00	191.80	199.55	5.92
R19	0.267	207.10	212.80	220.55	6.09
	0.271	210.30	215.90	223.65	6.15
R21	0.283	220.20	217.00	224.75	6.17
	0.297	231.90	222.00	229.75	6.28
R22	0.308	241.00	240.00	247.75	6.68
	0.311	243.50	243.20	250.95	6.75
R24	0.333	261.80	261.00	268.75	7.39
	0.343	271.20	265.00	272.75	7.49
R27	0.363	287.30	286.20	293.95	8.18
	0.382	303.20	301.30	309.05	8.67
R29	0.391	310.70	310.80	318.55	8.94
	0.396	314.70	313.10	320.85	9.00
R31	0.407	323.70	325.00	332.75	9.32
	0.411	327.00	329.90	337.65	9.44
R34	0.436	347.30	345.80	353.55	9.86
	0.440	350.70	349.00	356.75	9.94
R38	0.471	376.70	374.60	382.35	10.49
	0.474	379.40	380.40	388.15	10.61

Table 25. Backtrack path for Site 850.

Age (Ma)	Latitude (-° S; +° N)	Longitude (° W)
1	0.75	109.24
2	0.50	108.48
3	0.26	107.71
4	0.01	106.95
5	-0.23	106.19
6	-0.46	105.42
7	-0.70	104.66
8	-0.93	103.89
9	-1.15	103.12
10	-1.38	102.35
11	-1.60	101.58
12	-1.82	100.81
13	-2.03	100.04
14	-2.24	99.26

Pole of rotation: 0–12 Ma; 67.0° N 59.0° W; Angular velocity: 0.84°/m.y. (van Andel et al., 1975)

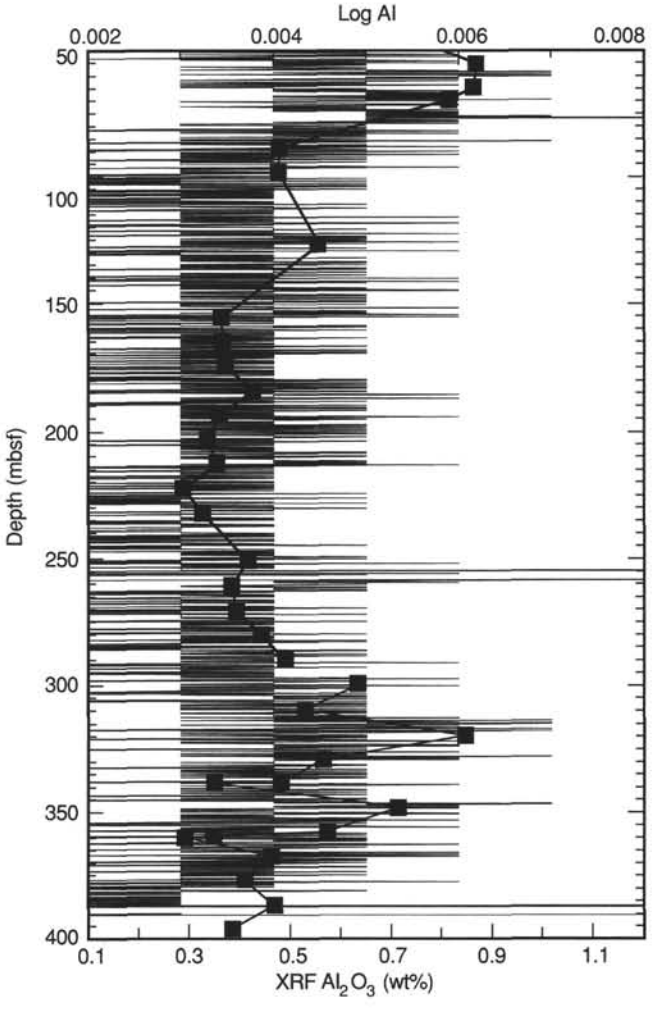

Figure 37. Comparison of weight percent Al_2O_3 measured by XRF (thick solid line with filled squares) with weight fraction of Al measured by geochemical logs (thin solid line). Logging tool was in pipe for the upper 50 m of the hole; data above that depth are not comparable.

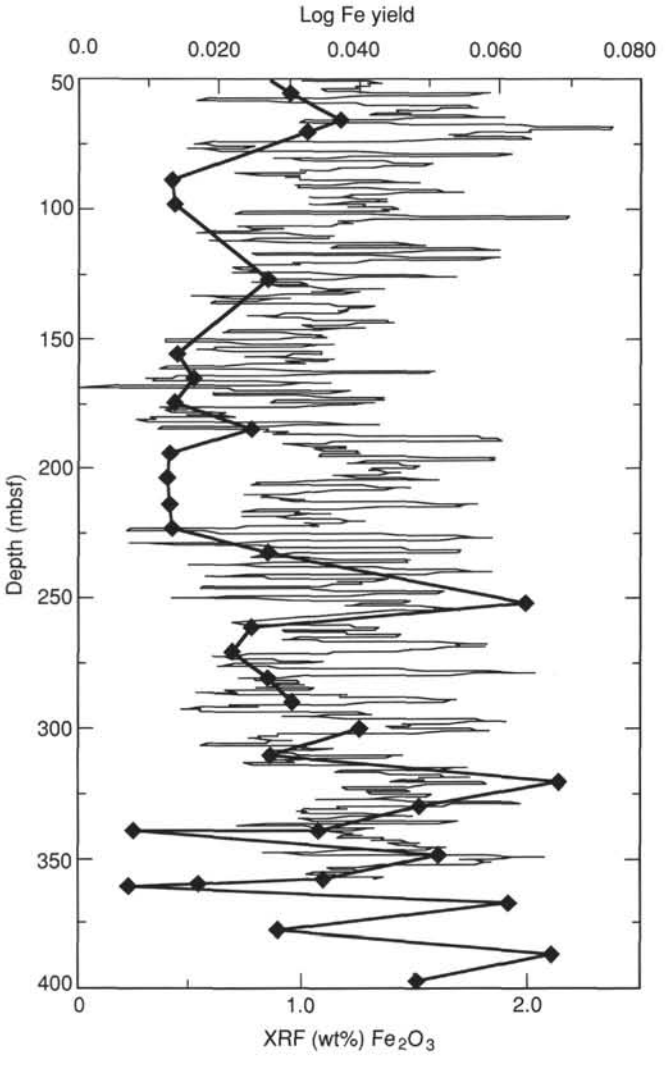

Figure 38. Comparison of weight percent Fe_2O_3 measured by XRF (thick line with filled diamonds) with Fe yield from the geochemical logging tool (thin solid line). Logging tool was in the drill pipe above 50 m; data above that depth are not comparable.

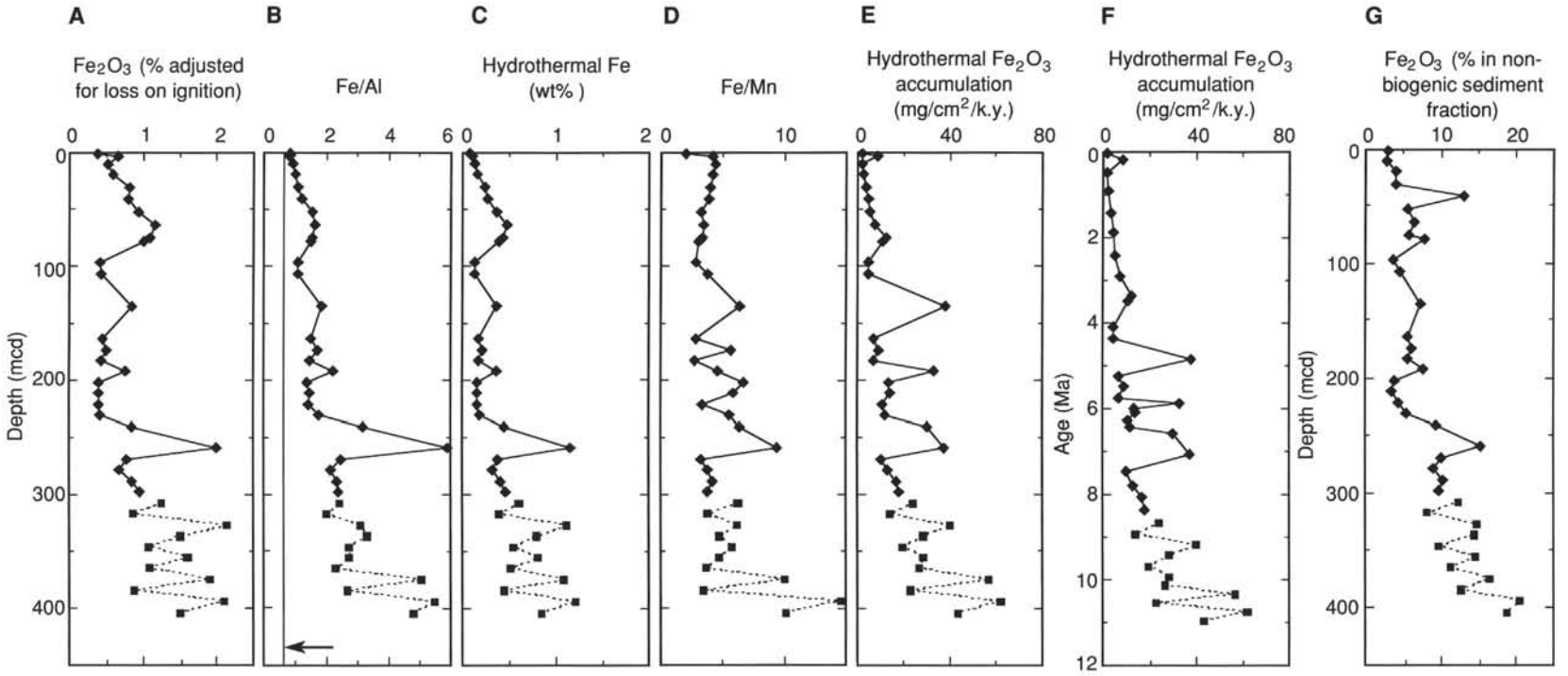

Figure 39. Hydrothermal indicators. **A.** Weight percent Fe_2O_3. **B.** Fe/Al. **C.** Weight percent hydrothermal Fe calculated (see text). **D.** Fe/Mn. **E.** Hydrothermal Fe accumulation rate (mg/cm^2/k.y.) vs. depth (mcd). **F.** Hydrothermal Fe accumulation rate (mg/cm^2/k.y.) vs. age (Ma). **G.** Weight percent Fe_2O_3 in nonbiogenic sediment fraction.

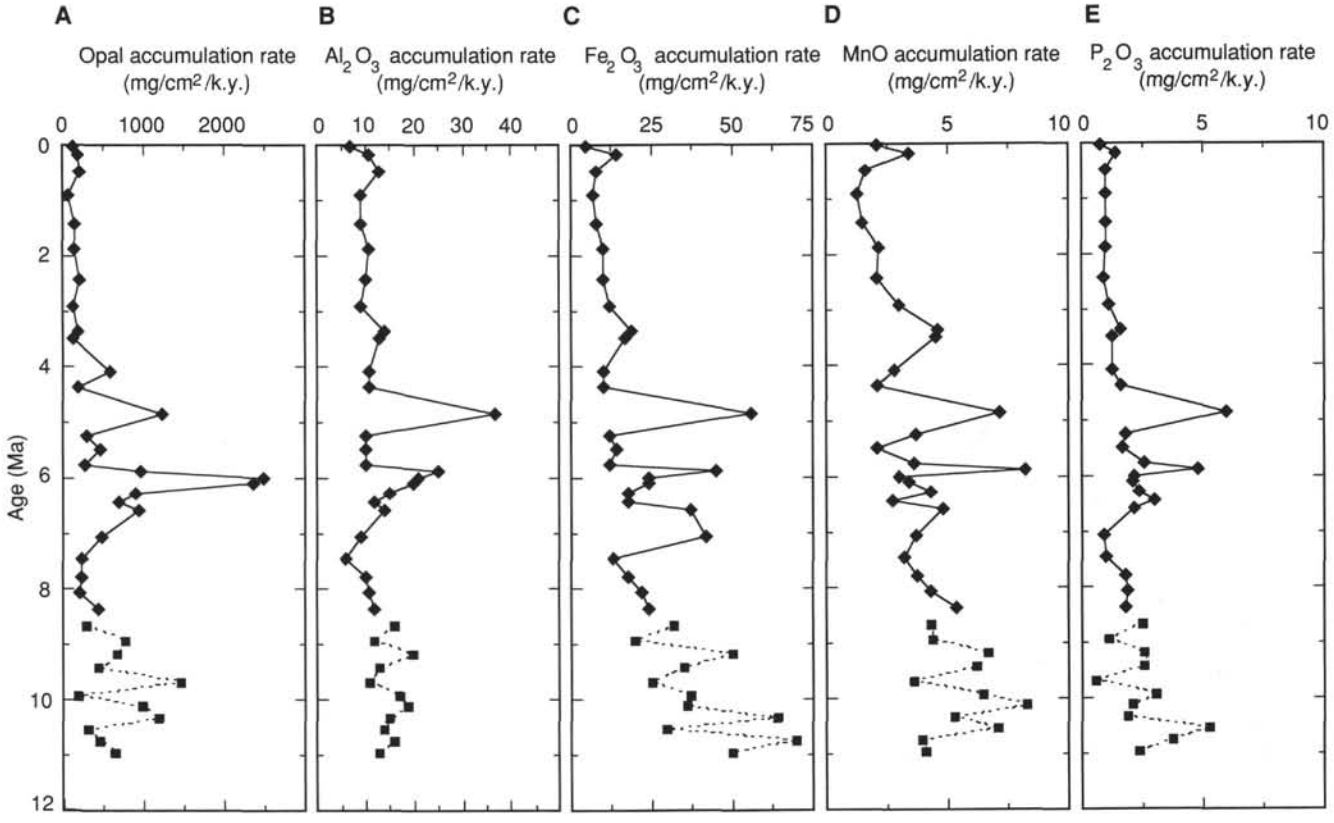

Figure 40. Accumulation rates of biogenic silica (opal), Al_2O_3, Fe_2O_3, MnO, and P_2O_5.

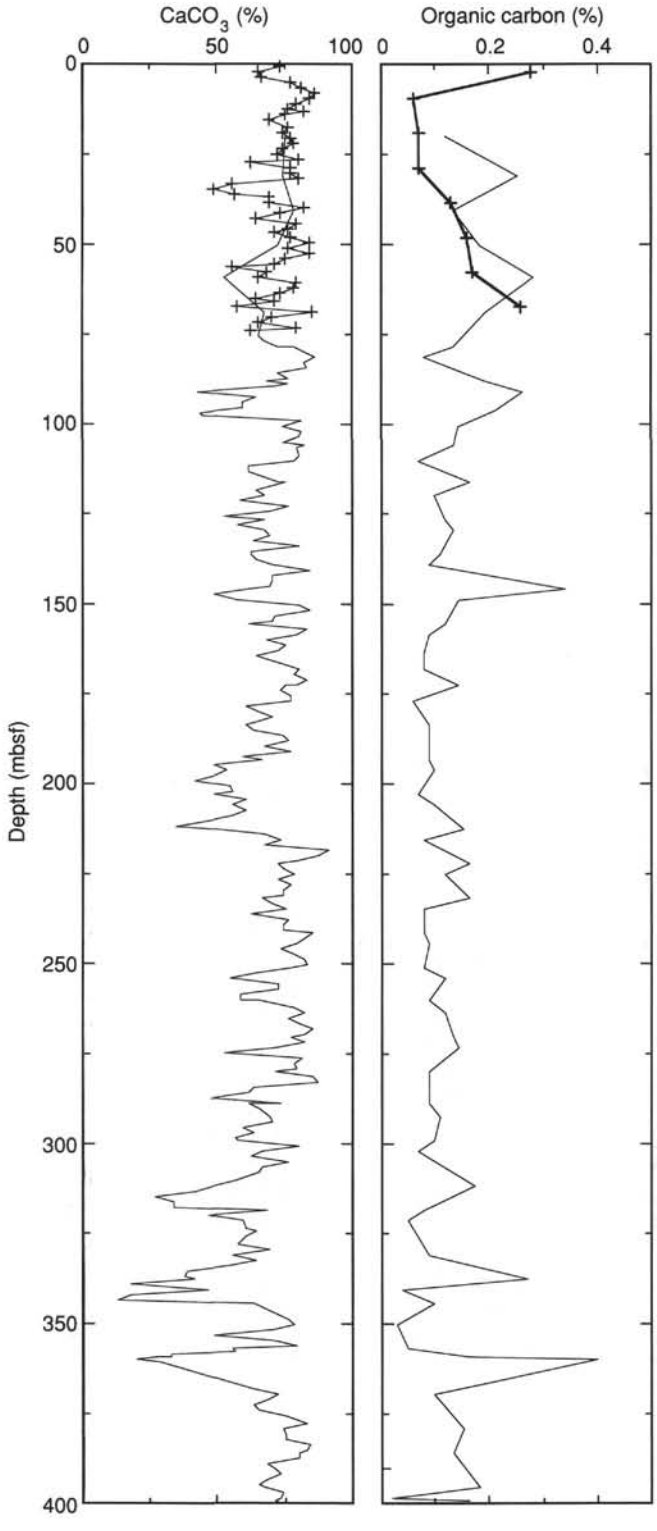

Figure 41. Downhole records of percentages of $CaCO_3$ and C_{org} vs. ODP depth for Holes 850A (crosses) and 850B (no symbols).

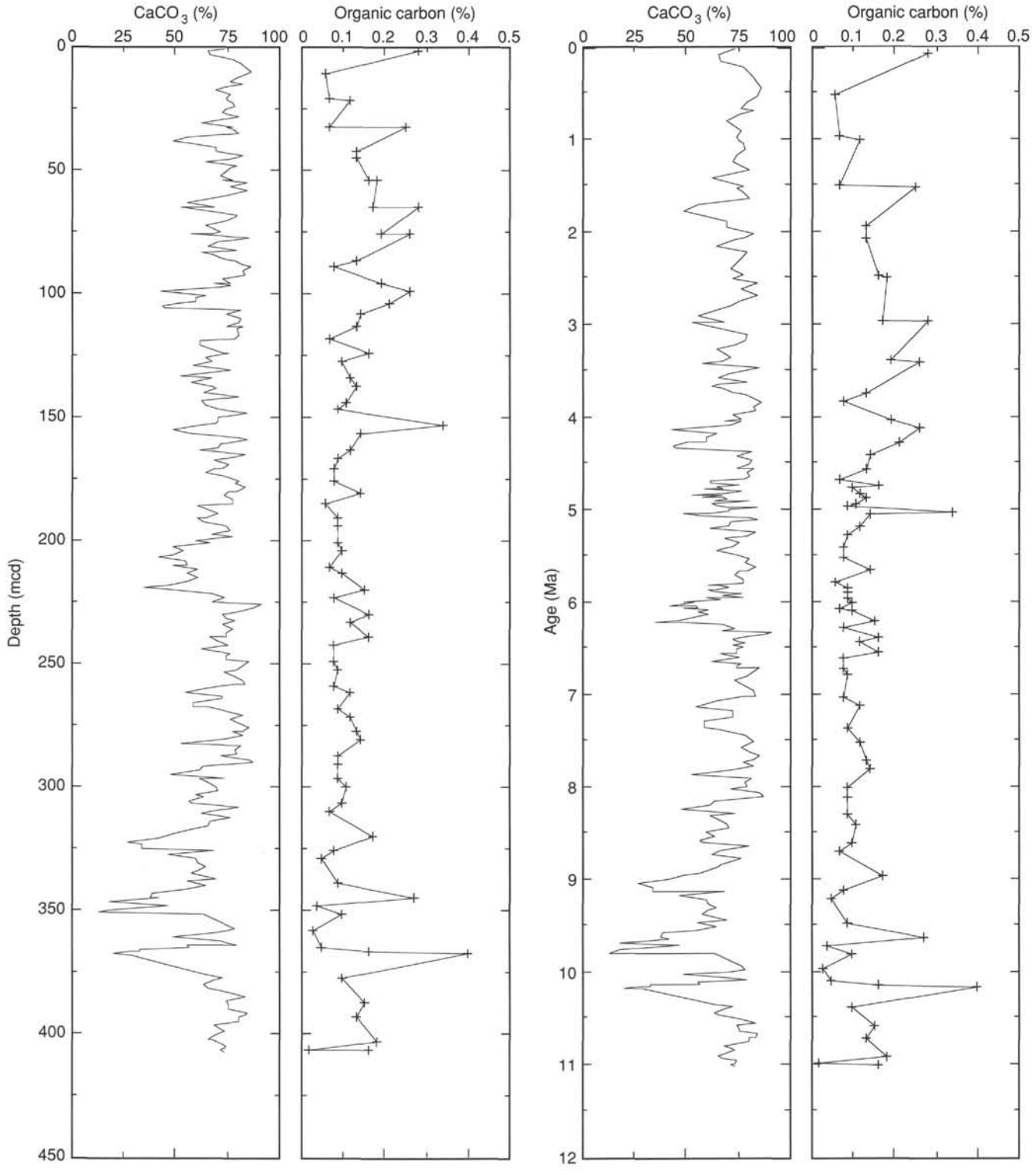

Figure 42. Plots of percentages of $CaCO_3$ and C_{org} vs. composite depth and age for Site 850.

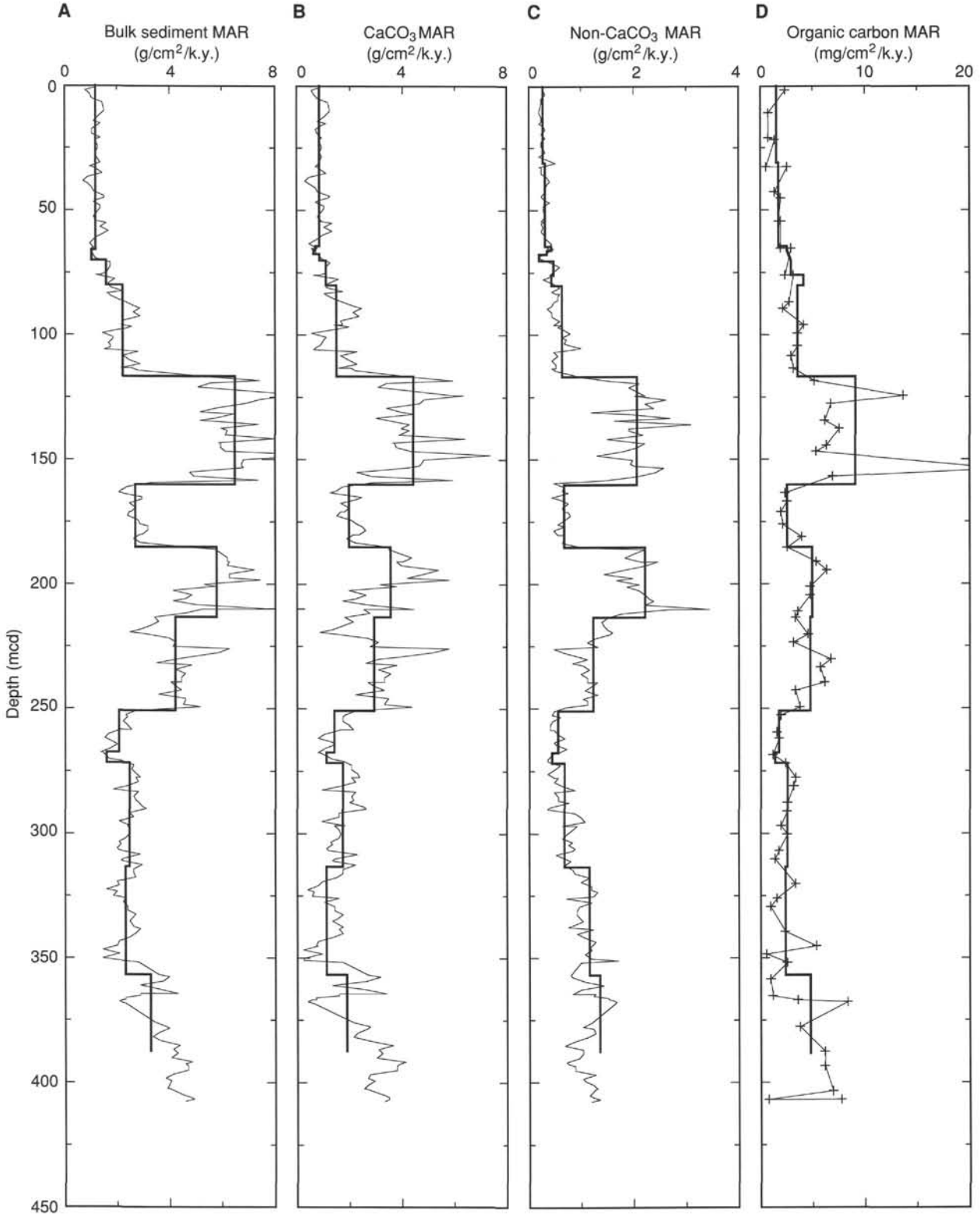

Figure 43. Mass accumulation rates of (**A**) bulk sediment, (**B**) $CaCO_3$, (**C**) non-$CaCO_3$ (1 – $CaCO_3$), and (**D**) C_{org} vs. composite depth at Site 850. Note different units for C_{org}. Thick line is mean value between each stratigraphic datum plane; thin line shows discrete accumulation rates calculated for each sample.

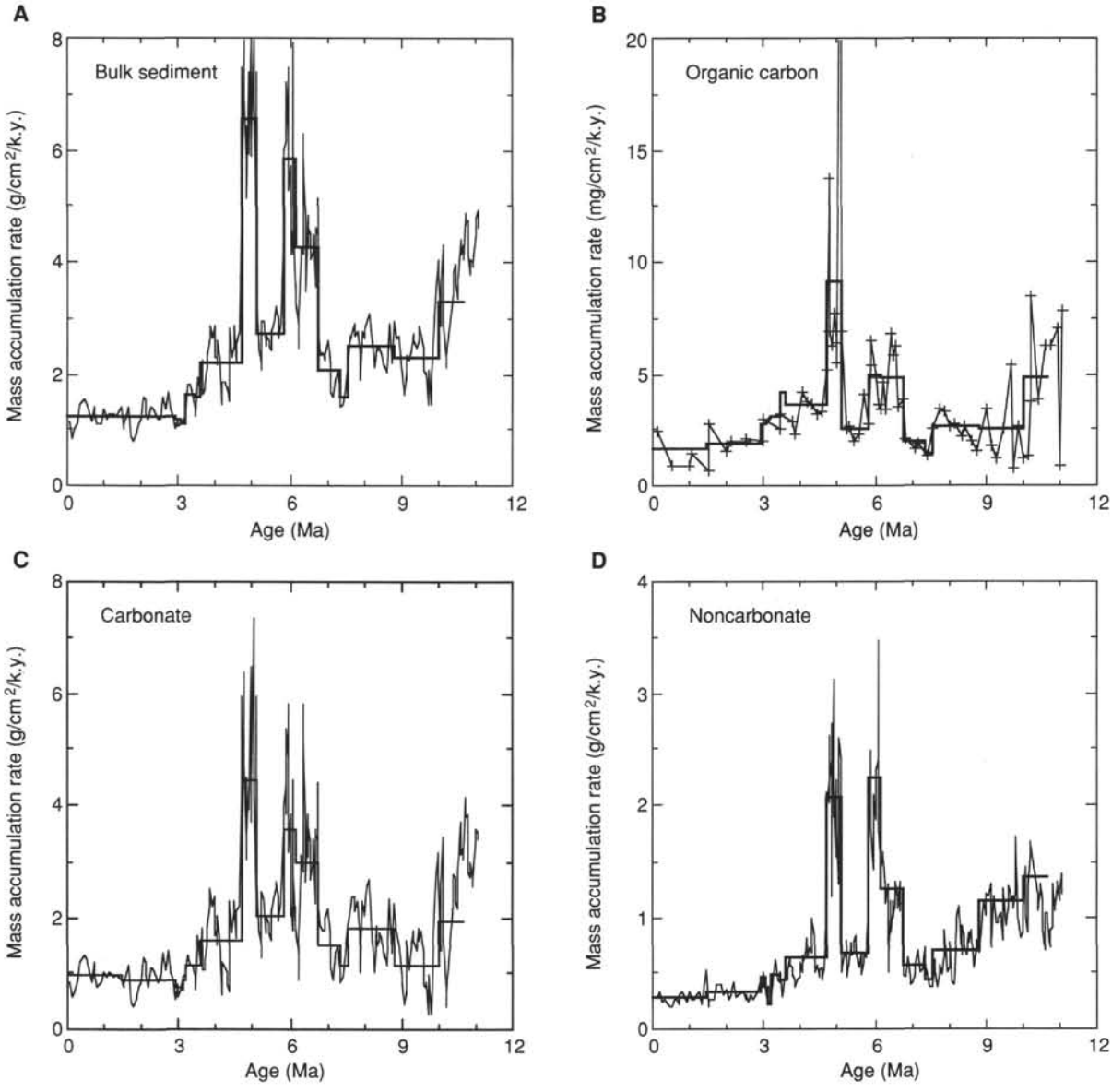

Figure 44. Mass accumulation rates of (**A**) bulk sediment, (**B**) C_{org}, (**C**) $CaCO_3$, and (**D**) non-$CaCO_3$ (1 – $CaCO_3$) vs. age in sediments from Site 850. Thick line = mean value between each stratigraphic datum plane; thin line = discrete accumulation rates calculated for each sample. Note different units for C_{org}.

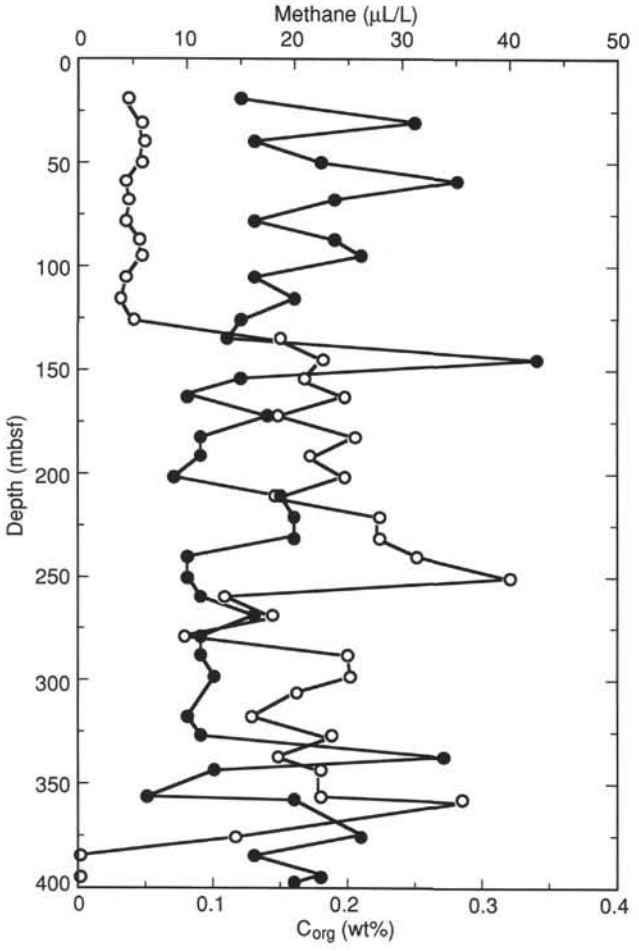

Figure 45. Concentrations of sorbed methane (open circles) and C_{org} (solid circles) vs. depth in Hole 850B.

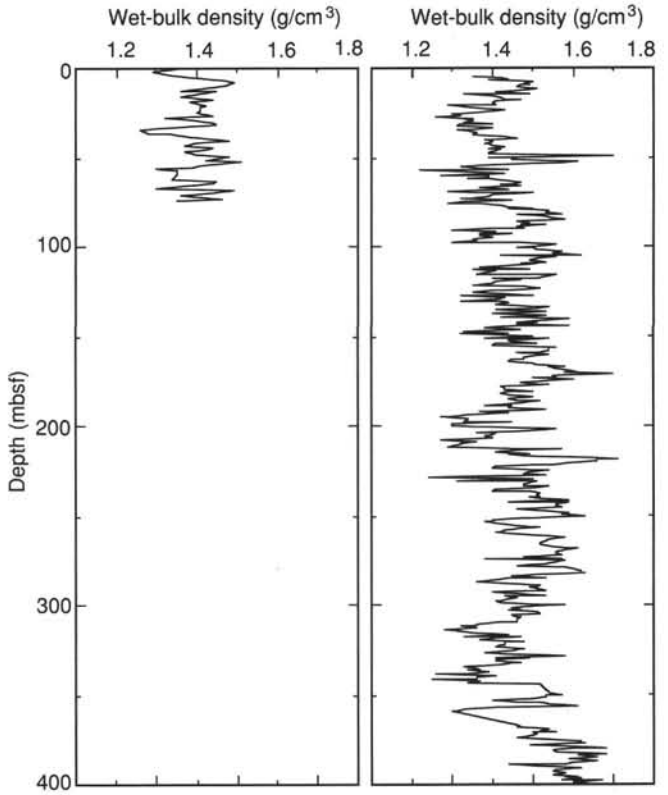

Figure 46. Wet-bulk density vs. depth, Holes 850A (left) and 850B (right).

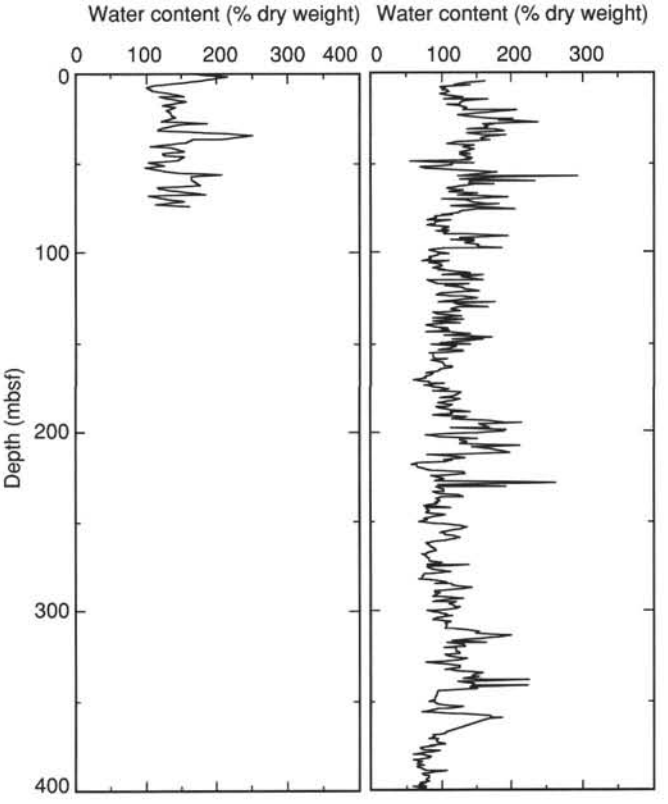

Figure 47. Water content (% dry weight) vs. depth, Holes 850A (left) and 850B (right).

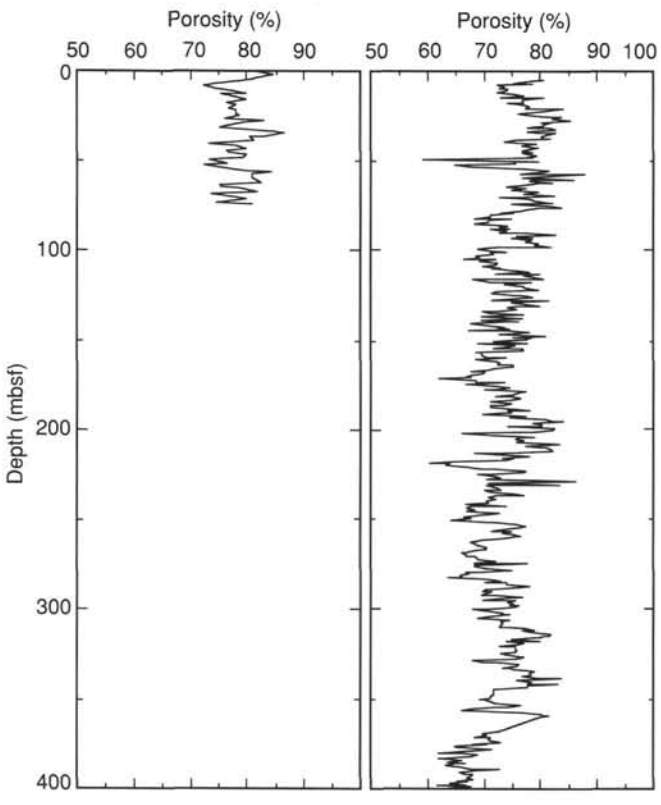

Figure 48. Porosity vs. depth, Holes 850A (left) and 850 (right).

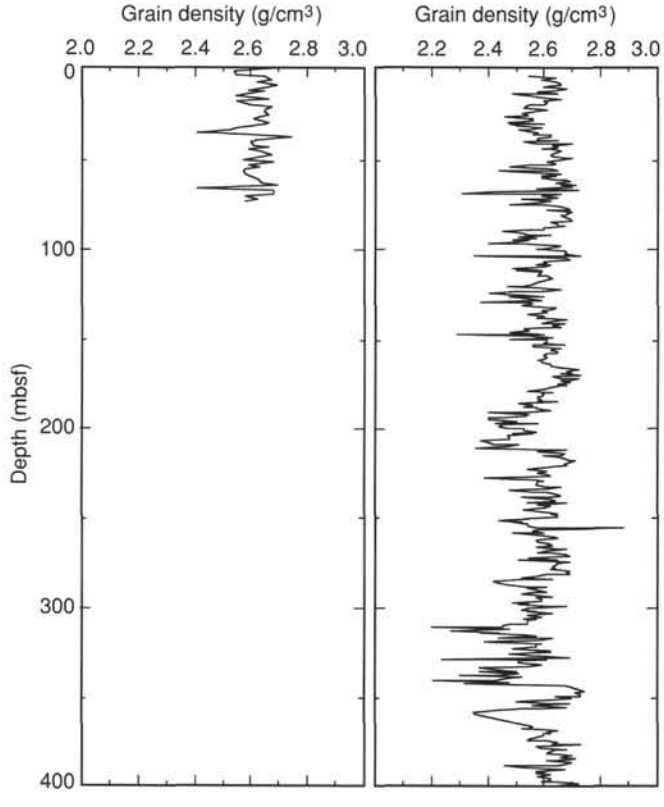

Figure 49. Grain density vs. depth, Holes 850A (left) and 850B (right).

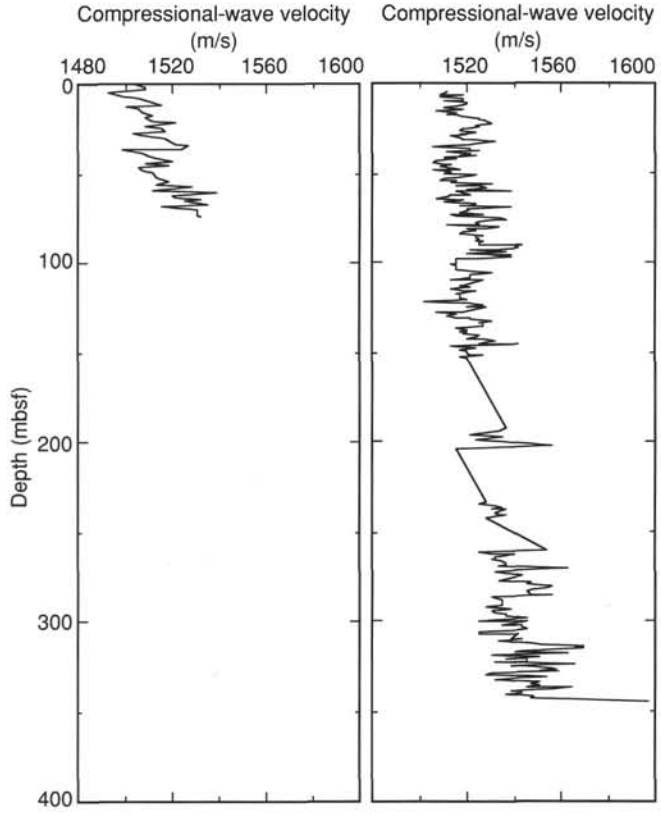

Figure 50. Compressional-wave velocity vs. depth, Holes 850A (left) and 850B (right).

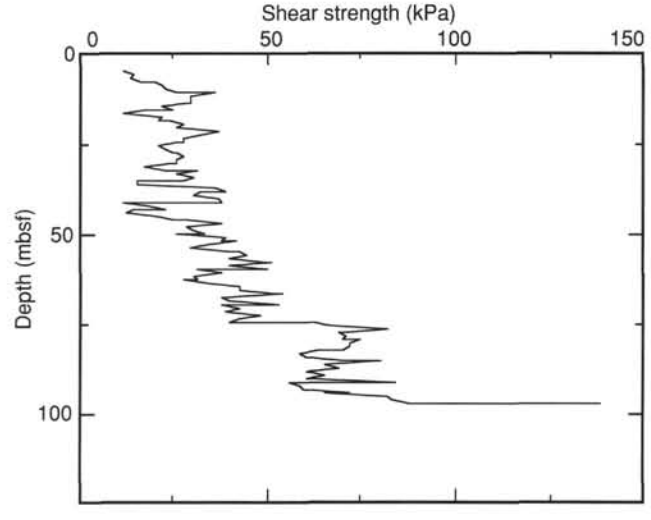

Figure 51. Undrained shear strength vs. depth, Hole 850B.

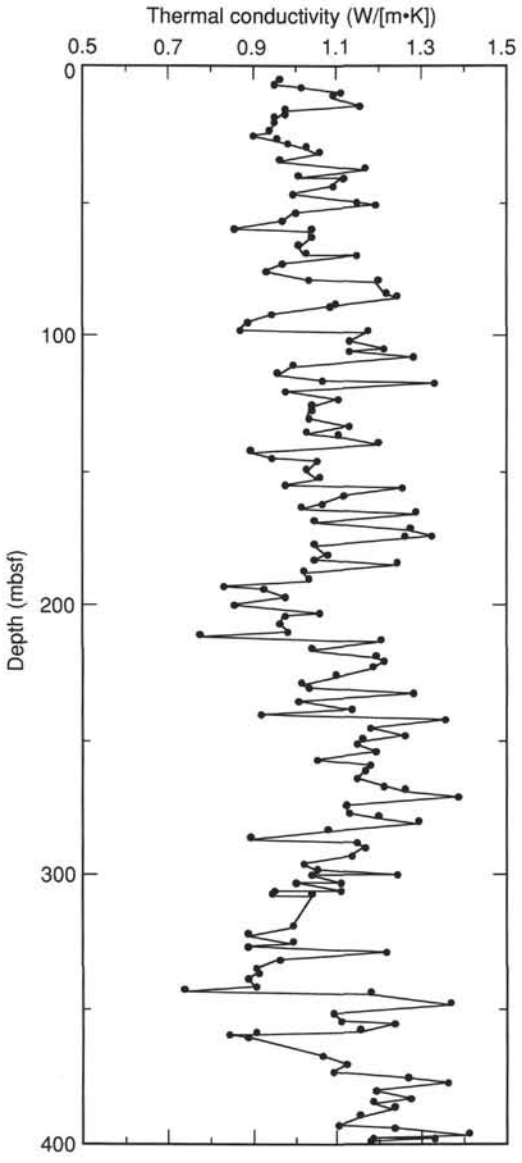

Figure 52. Thermal conductivity vs. depth, Hole 850B.

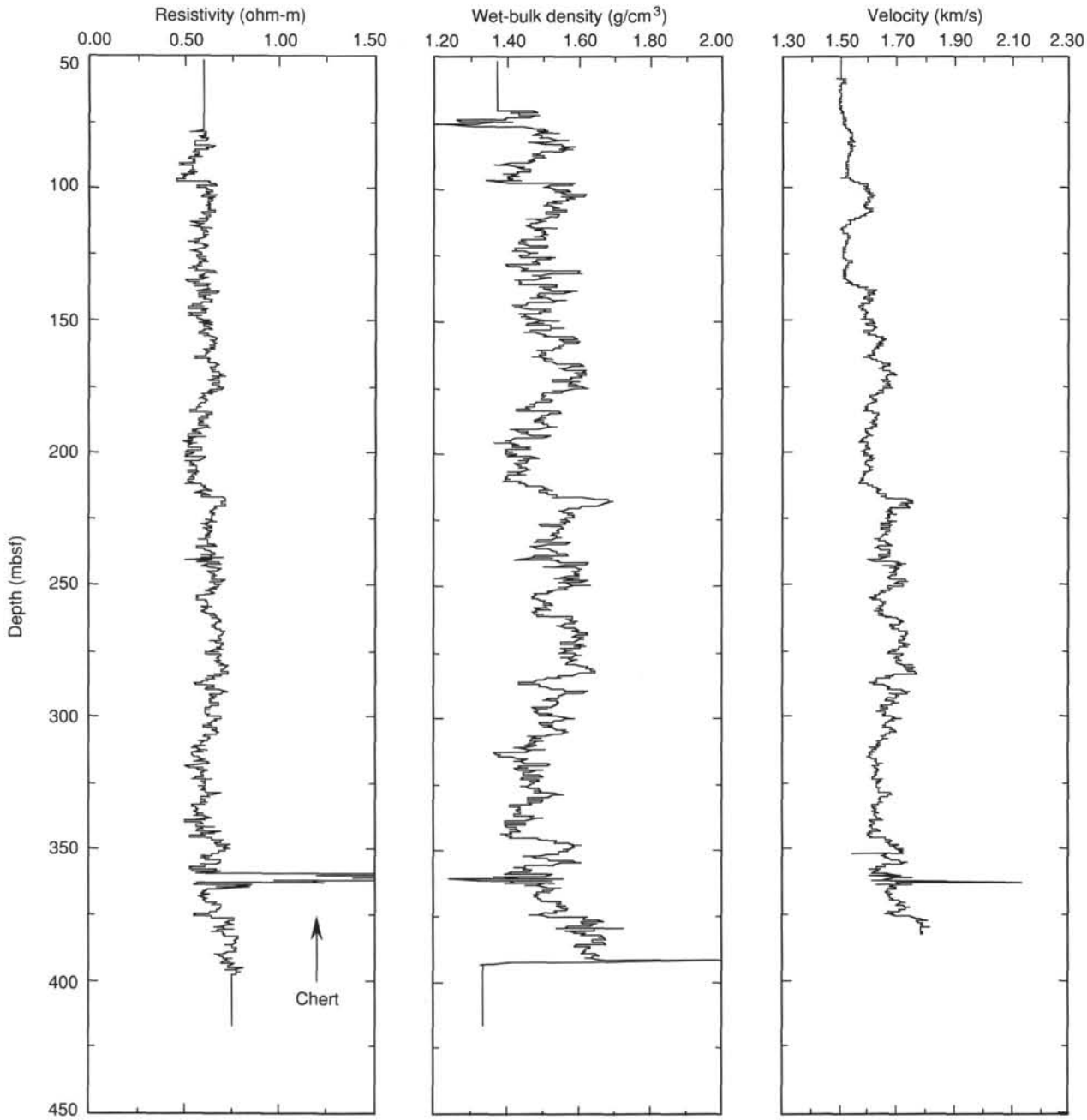

Figure 53. Variations of resistivity, wet-bulk density, and sonic velocity from Hole 850B. The entire sediment column is a single, log-derived stratigraphic unit.

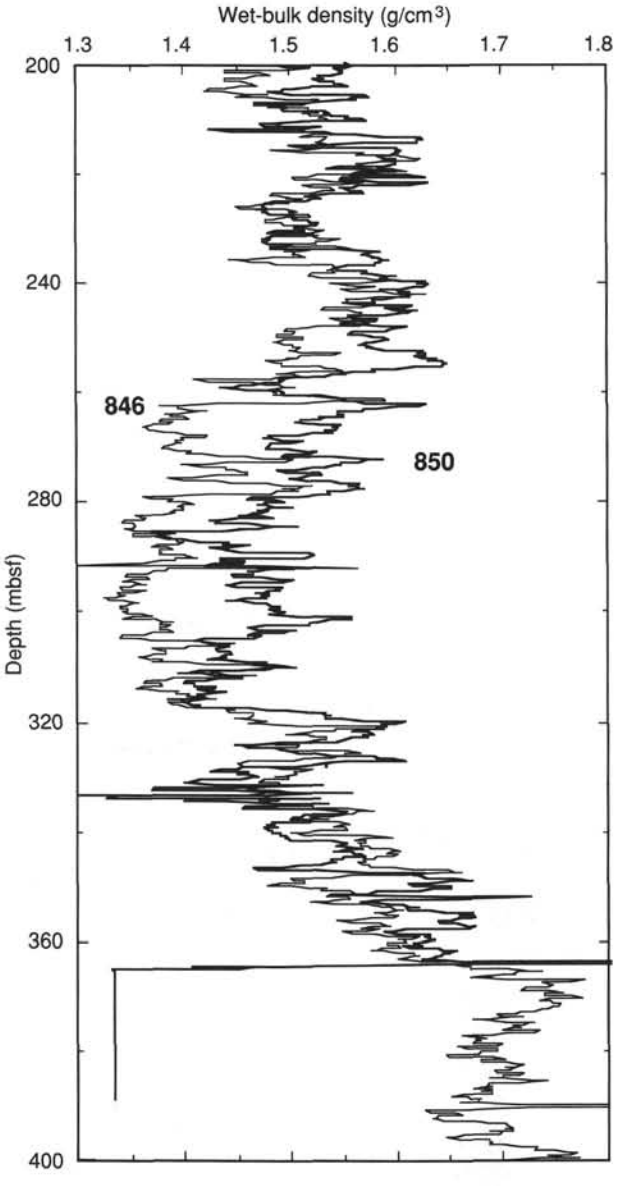

Figure 54. Comparison of log Unit 2 in Site 846 (260–320 mbsf; thin solid line) with equivalent sediments in Site 850 (thick solid line). Density log from Site 850 has been shifted upward by 28 m to match the two equivalent intervals.

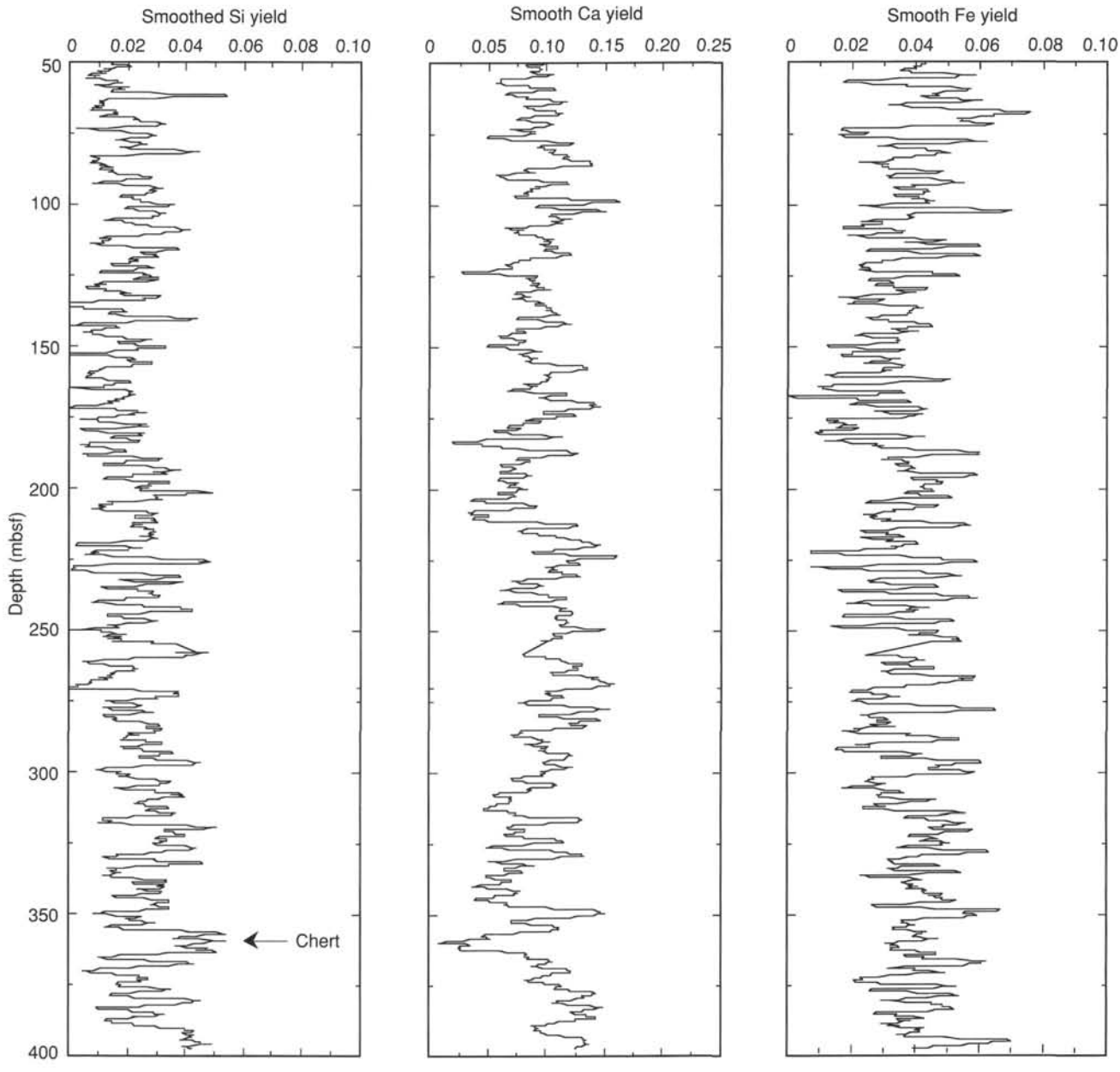

Figure 55. Variation in chemical composition downhole in Hole 850B, as recorded by the GST. Note the high Si and low Ca associated with a chert interval at 361 mbsf. Also note that little sign of basal metalliferous sediments is seen in the Fe log.

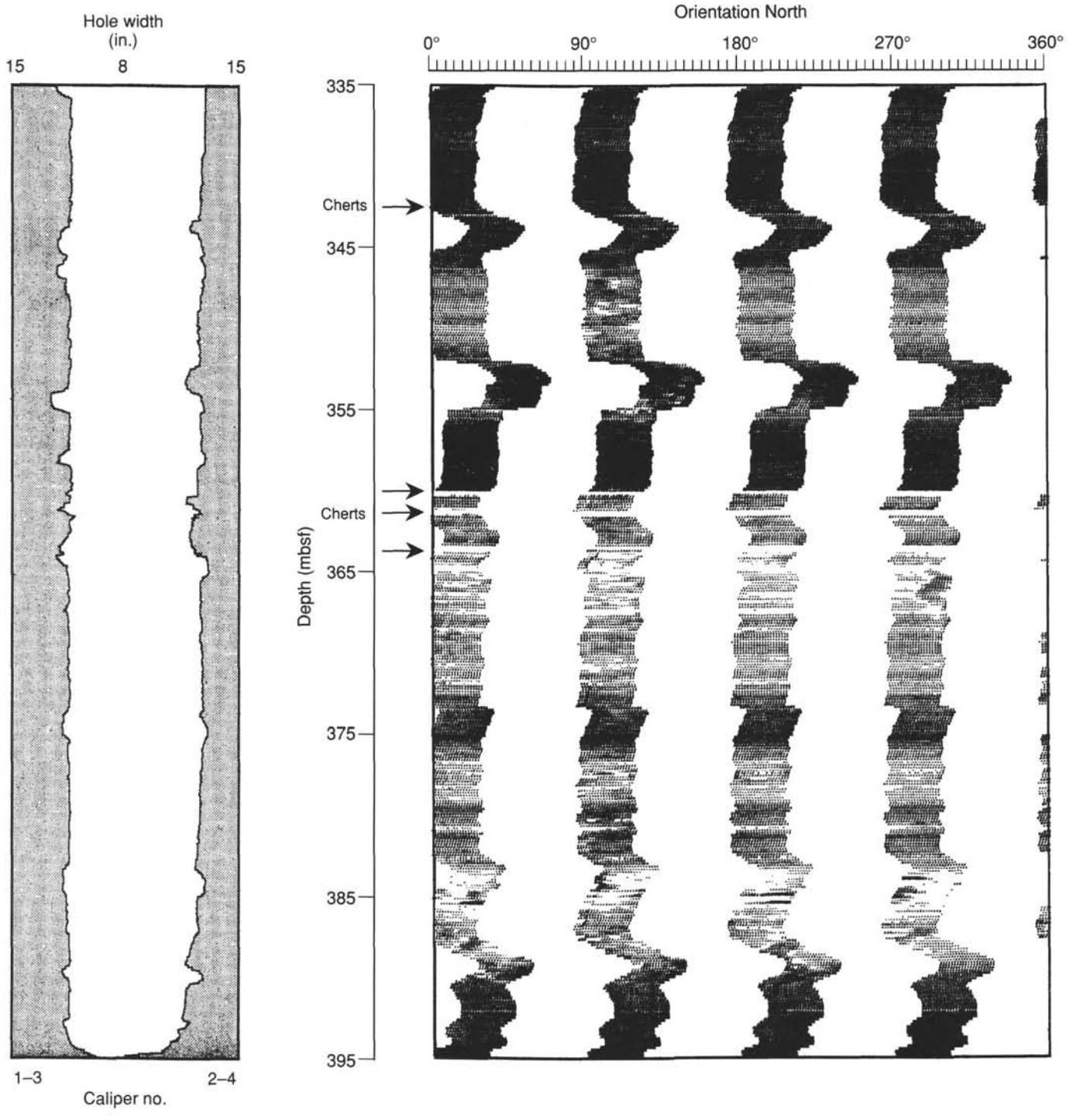

Figure 56. FMS image of the borehole and caliper log of Hole 850B from 335 to 395 mbsf. High-resistivity (low-porosity) intervals appear as light intervals. A thin chert band can be seen at about 344 mbsf, while the major chert interval in the core is found between 360 and 365 mbsf.

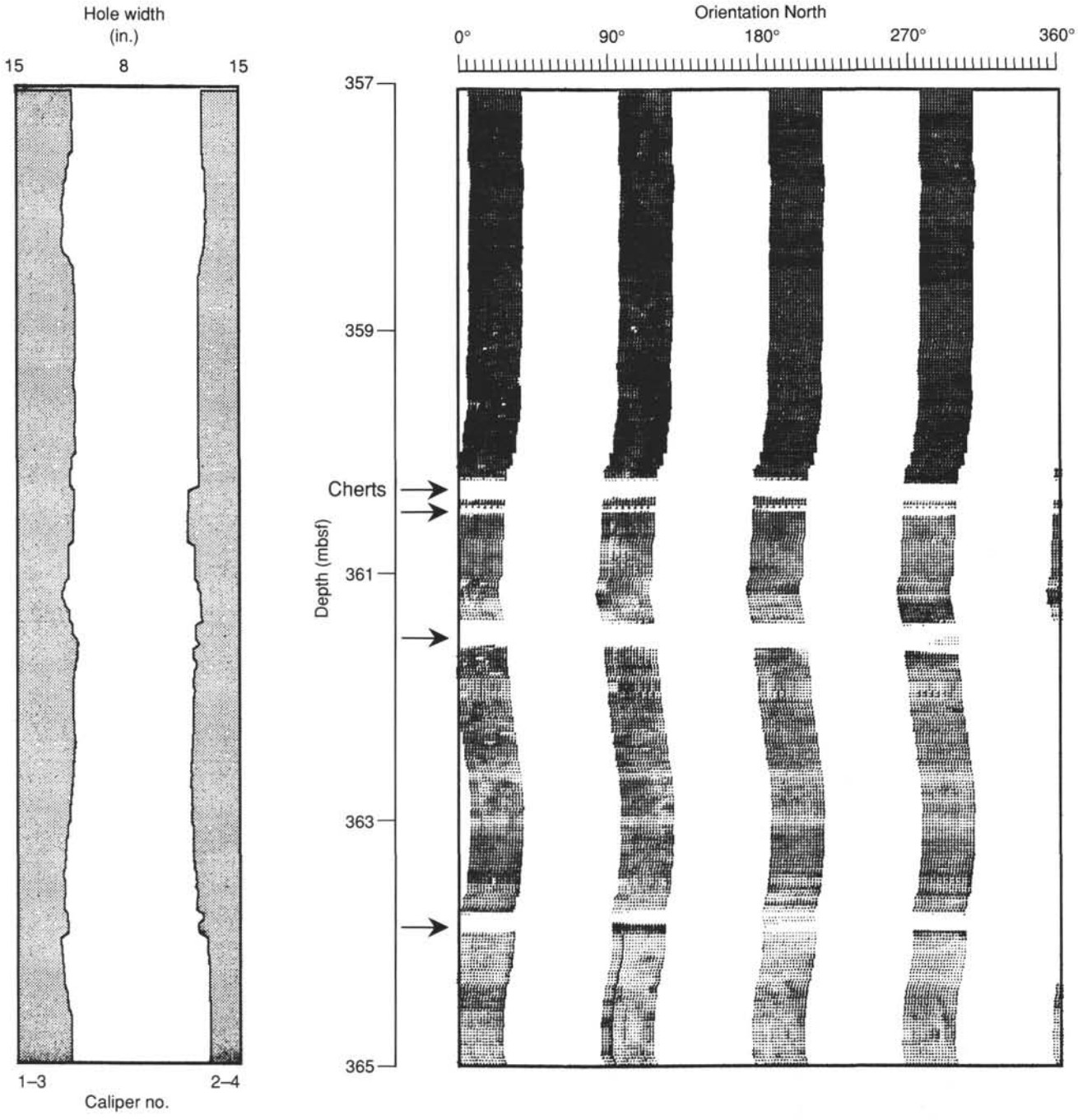

Figure 57. A more detailed FMS image and caliper log of the interval between 357 and 365 mbsf, showing four chert layers (arrows) between 360 and 364 mbsf. The top chert layer separates the high-resistivity diagenetically altered sediments from unaltered diatom oozes (Core 138-850A-38X; see "Lithostratigraphy" section, this chapter).

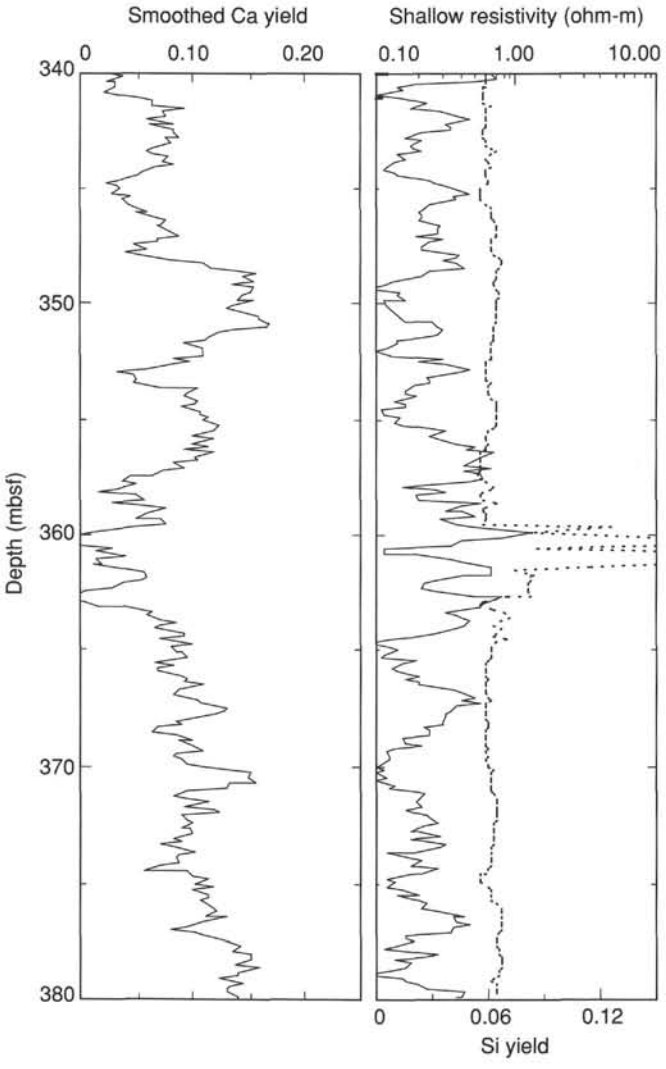

Figure 58. A comparison of the shallow resistivity log (dashed line; defines the chert interval) with Ca and Si logs from the geochemical tool string. Note that the interval of high Si and low Ca extends beyond the cherts. Core descriptions show that this interval is a diatom ooze.

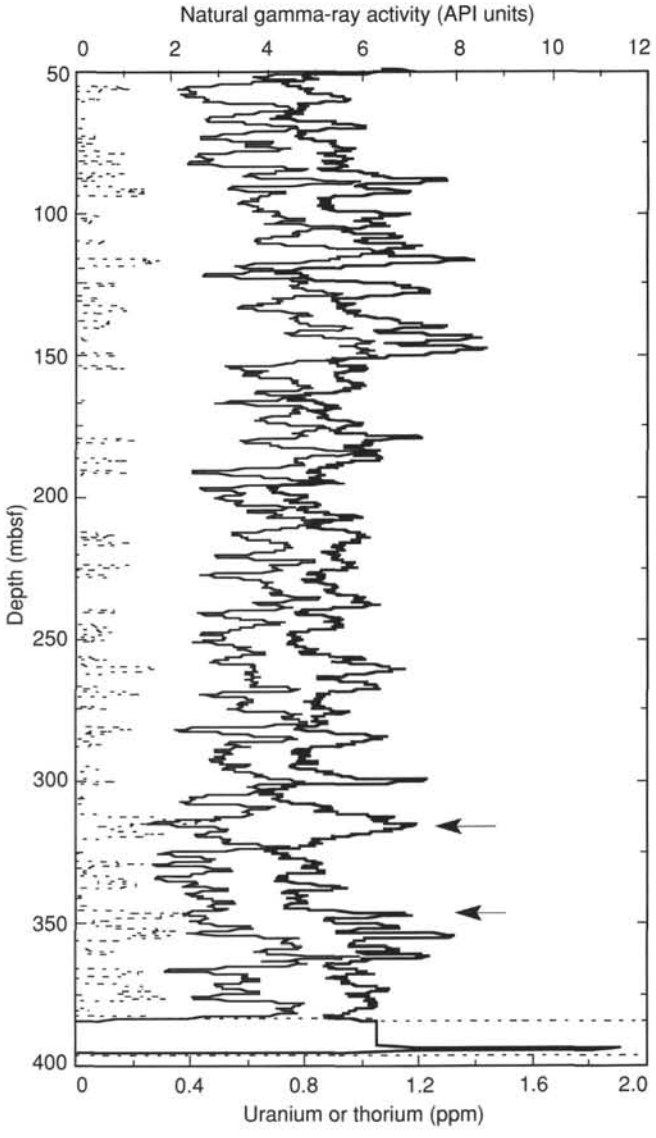

Figure 59. Profiles of natural gamma-ray activity (thick solid line), sedimentary uranium content (thin solid line), and thorium content (dotted line) in Hole 850B. Thorium is a measure of terrigenous content, while in Hole 850B, uranium probably reflects organic carbon deposition. Note that most of the natural gamma-ray activity is associated with uranium. Obvious exceptions are noted by two arrows, at 315 mbsf and 350 mbsf, where terrigenous deposition may have been an important contributor to natural gamma-ray activity. The highest uranium deposition occurs between 150 (5.1 Ma) and 80 mbsf (3.6 Ma), roughly when the site crosses the equator.

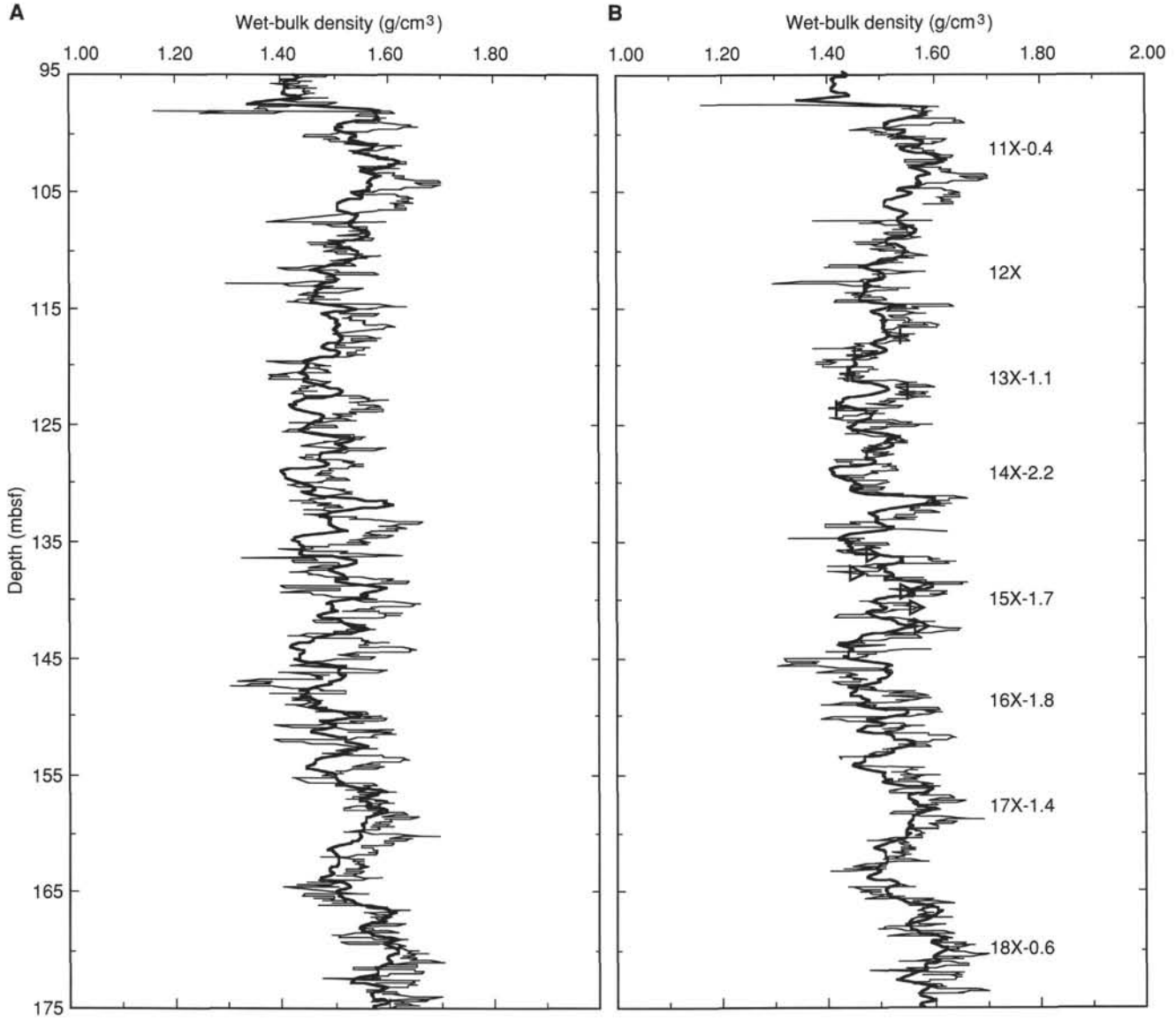

Figure 60. A comparison of unshifted (**A**) and shifted (**B**) GRAPE data (thin solid line) with density logs (thick solid line) recorded at Hole 850B. Individual cores were shifted by the number of meters shown after the core number in **B**. This figure illustrates that logs can be used to assess gaps or overlaps among cores, even when only a single XCB hole has been drilled.

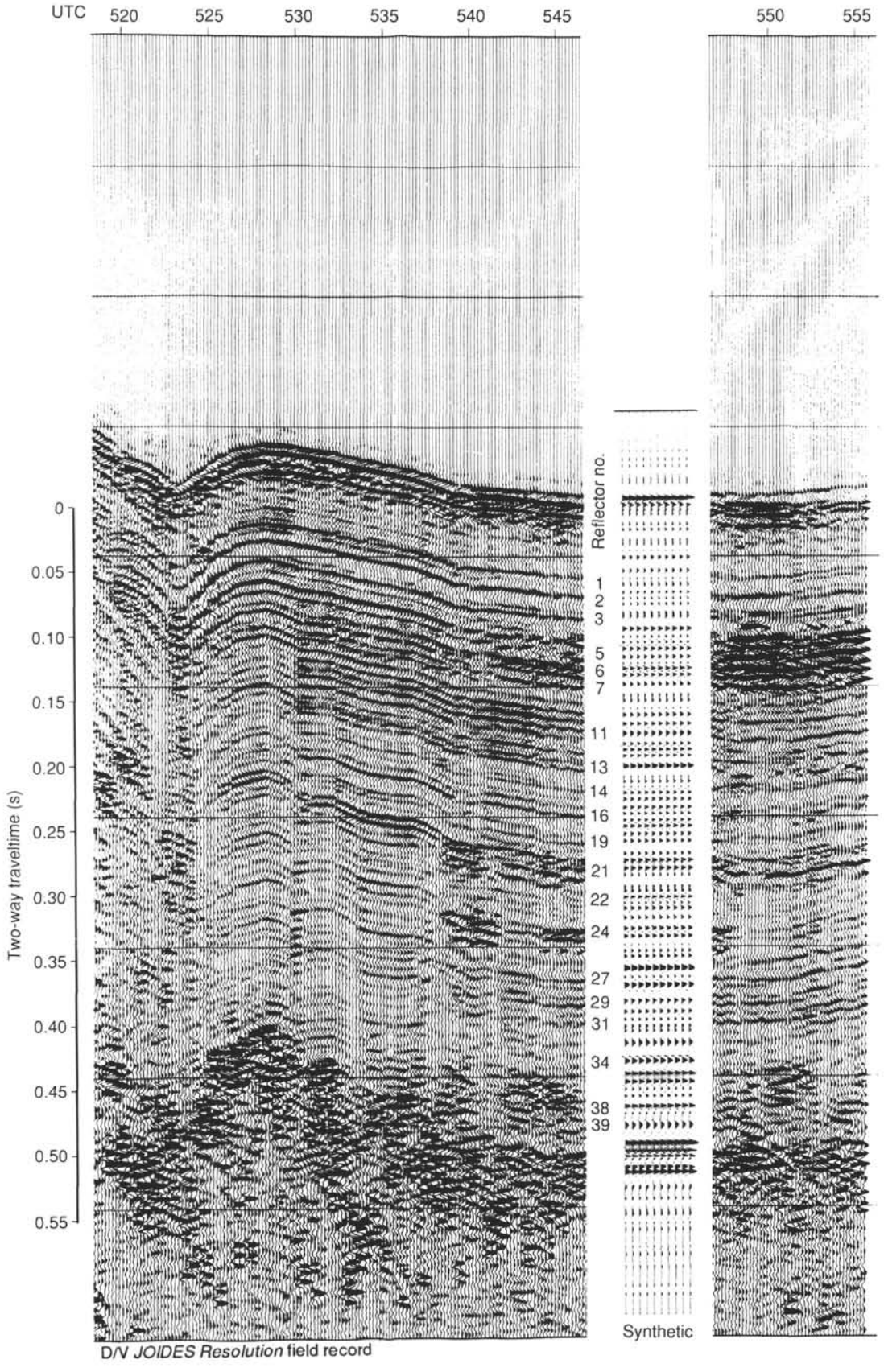

Figure 61. Comparison of synthetic seismogram and field record, Site 850.

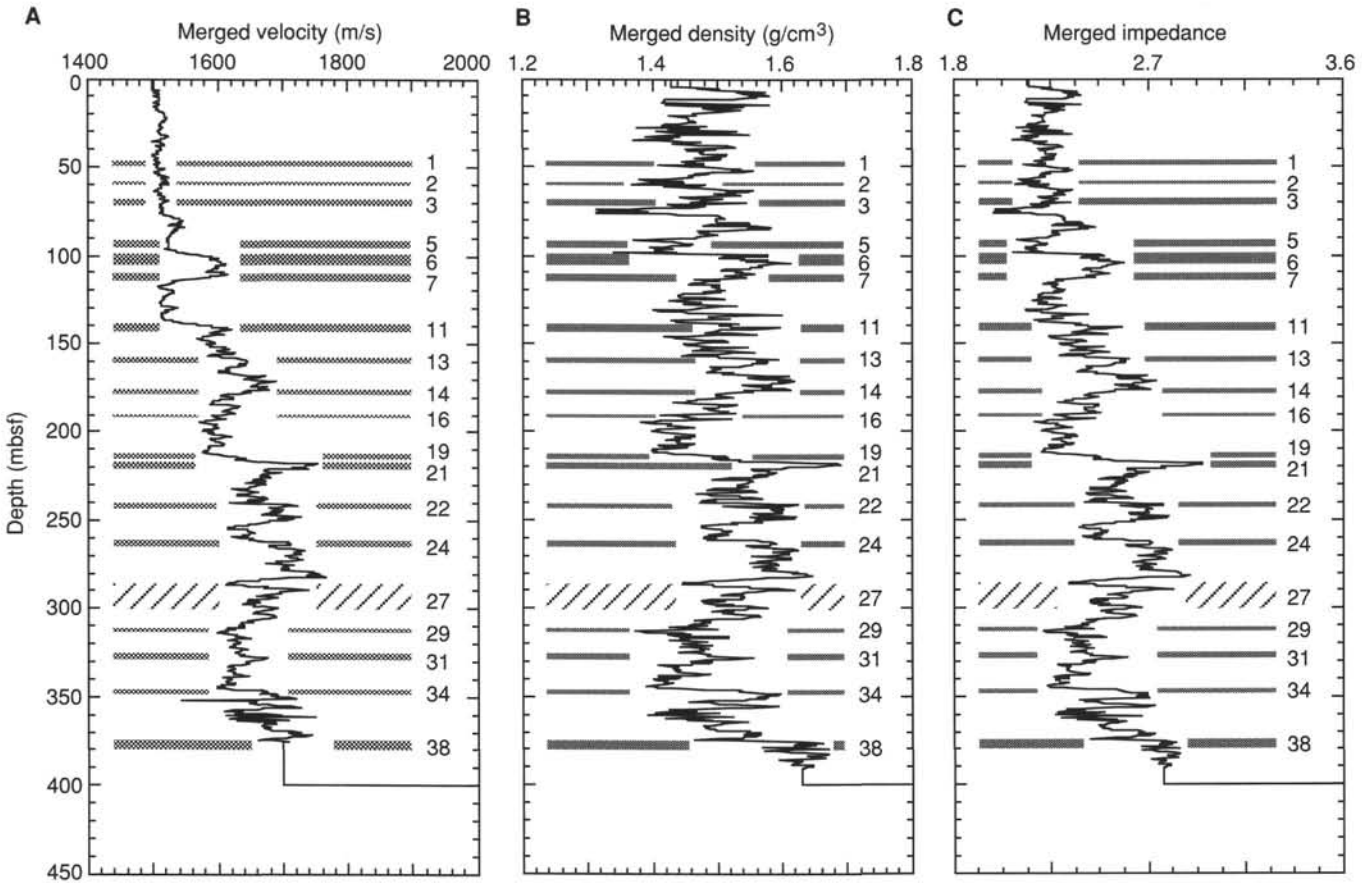

Figure 62. Velocity (**A**), density, (**B**), and acoustic impedance data (**C**) used for generating synthetic seismograms at Site 850. The 19 reflectors selected from the synthetic seismogram are shown for comparison.

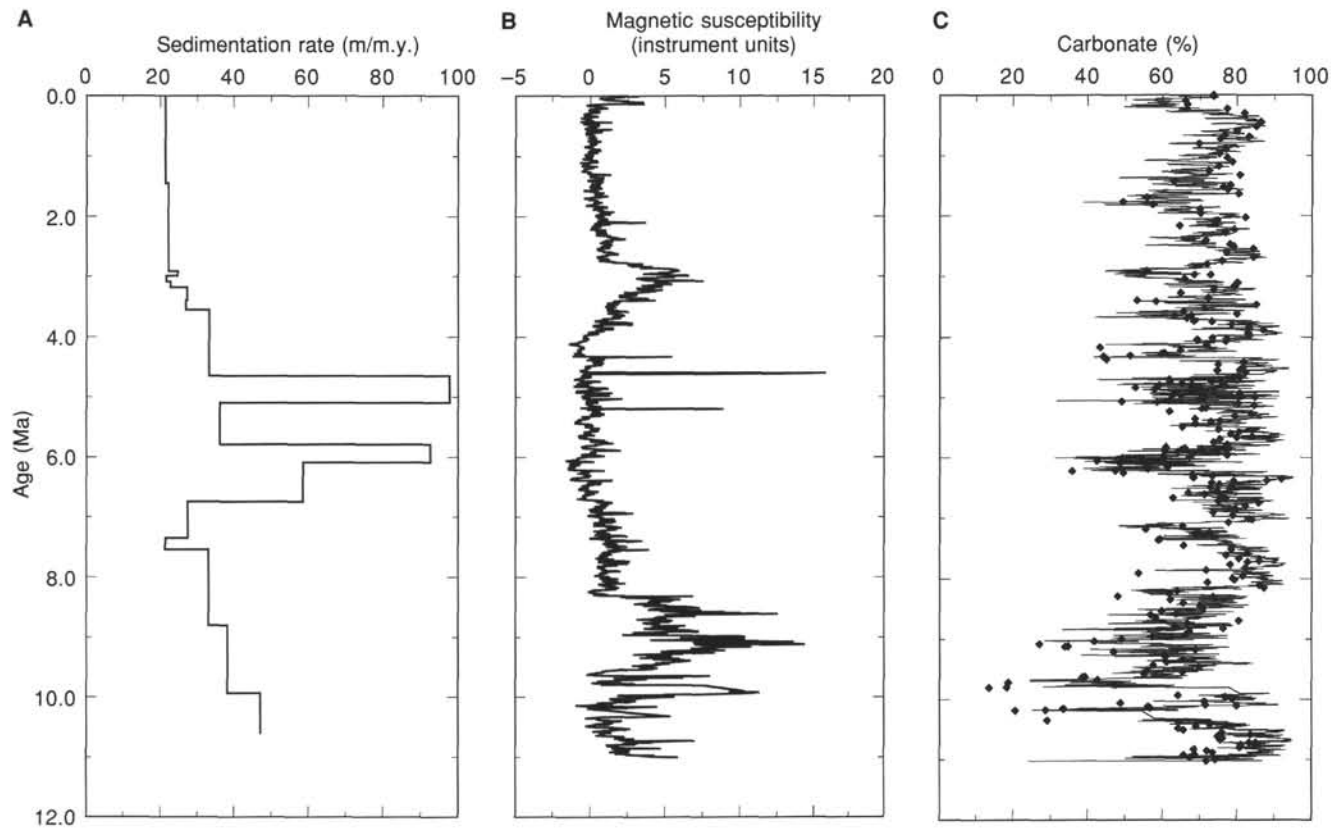

Figure 63. **A.** Sedimentation rate vs. age. **B.** magnetic susceptibility vs. age. **C.** Predicted (solid line) and measured carbonate content (diamonds) vs. age.

Hole 850B: Resistivity-Sonic-Natural Gamma Ray Log Summary

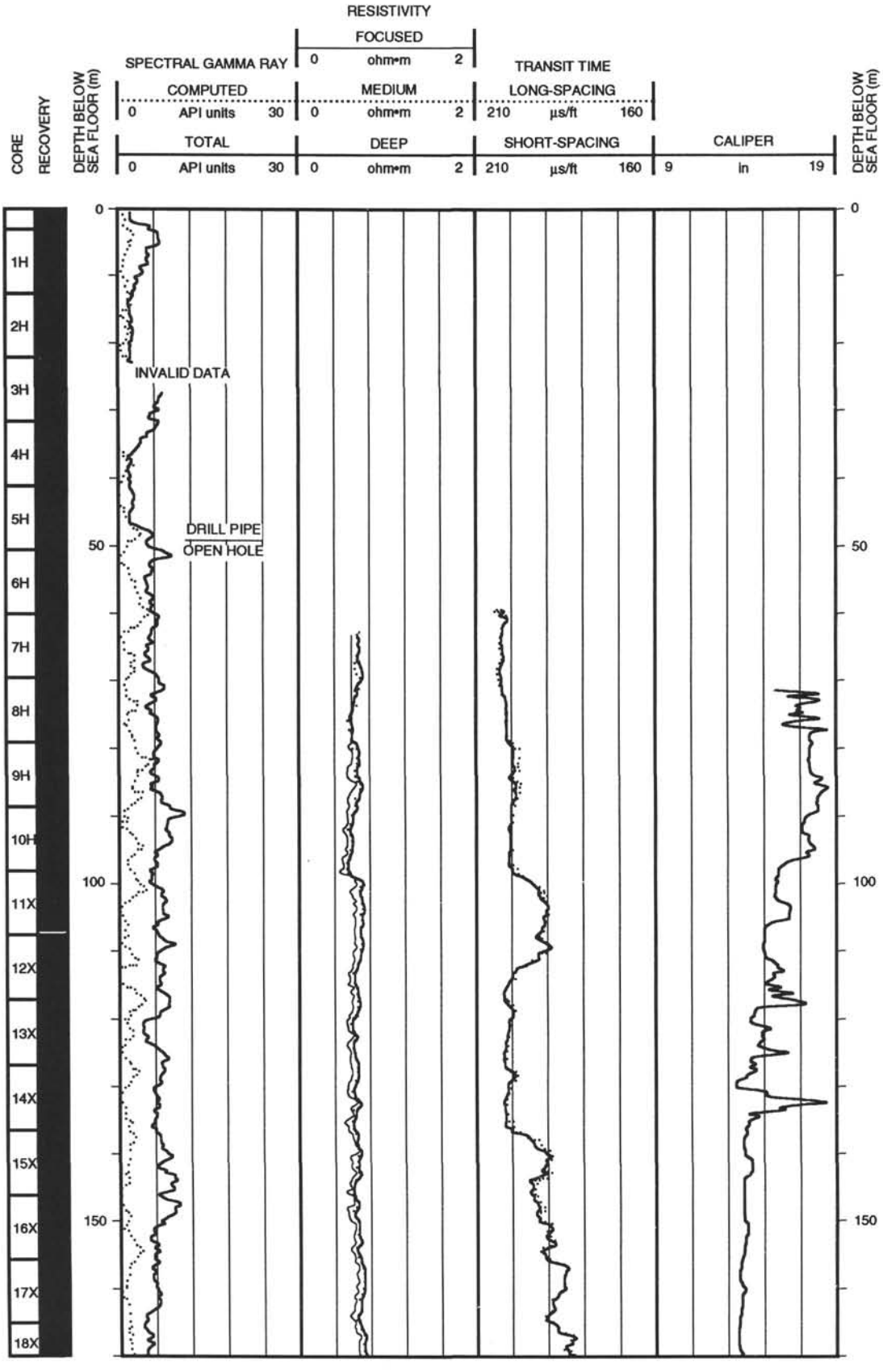

Hole 850B: Resistivity-Sonic-Natural Gamma Ray Log Summary (continued)

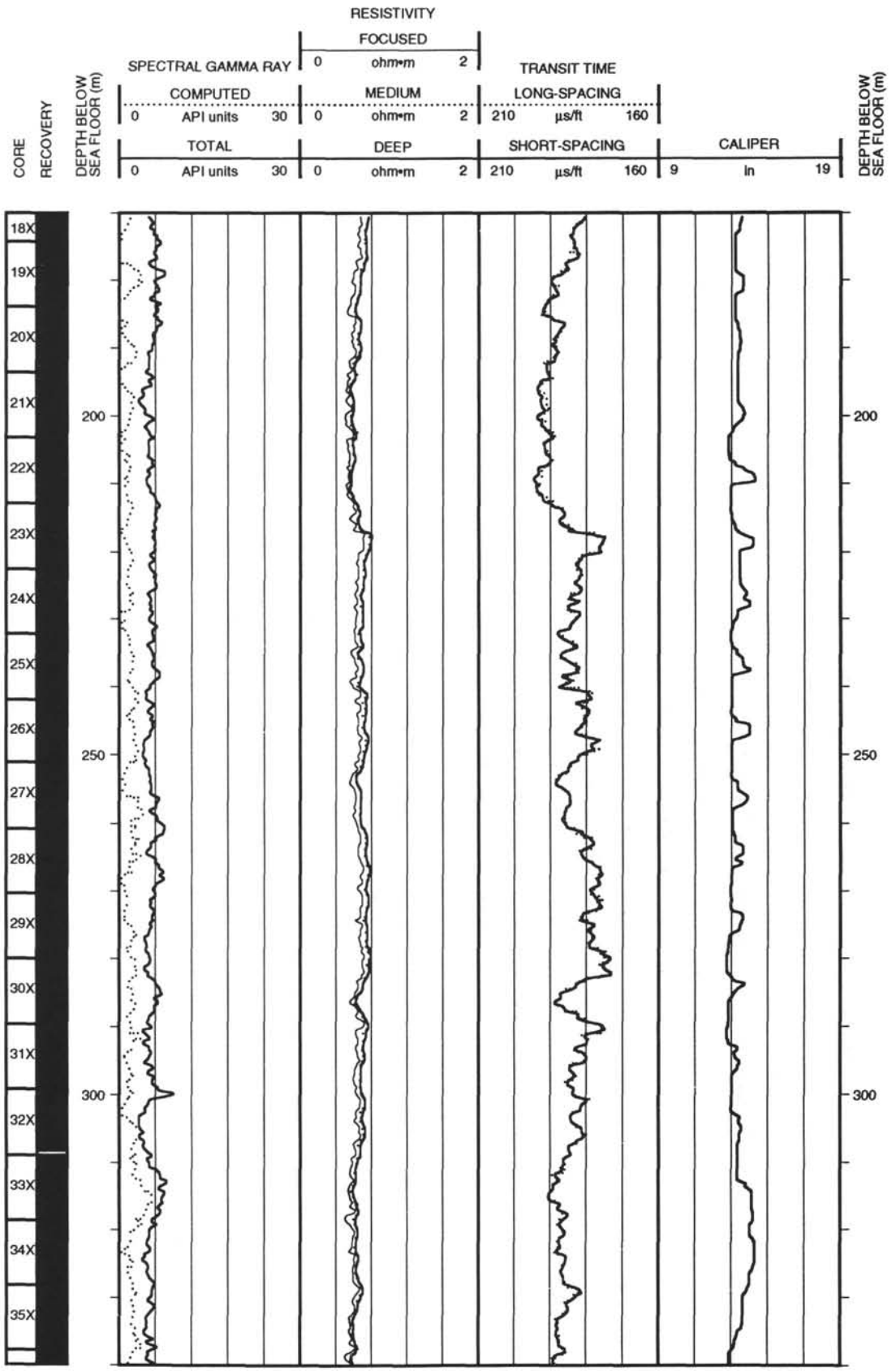

Hole 850B: Resistivity-Sonic-Natural Gamma Ray Log Summary (continued)

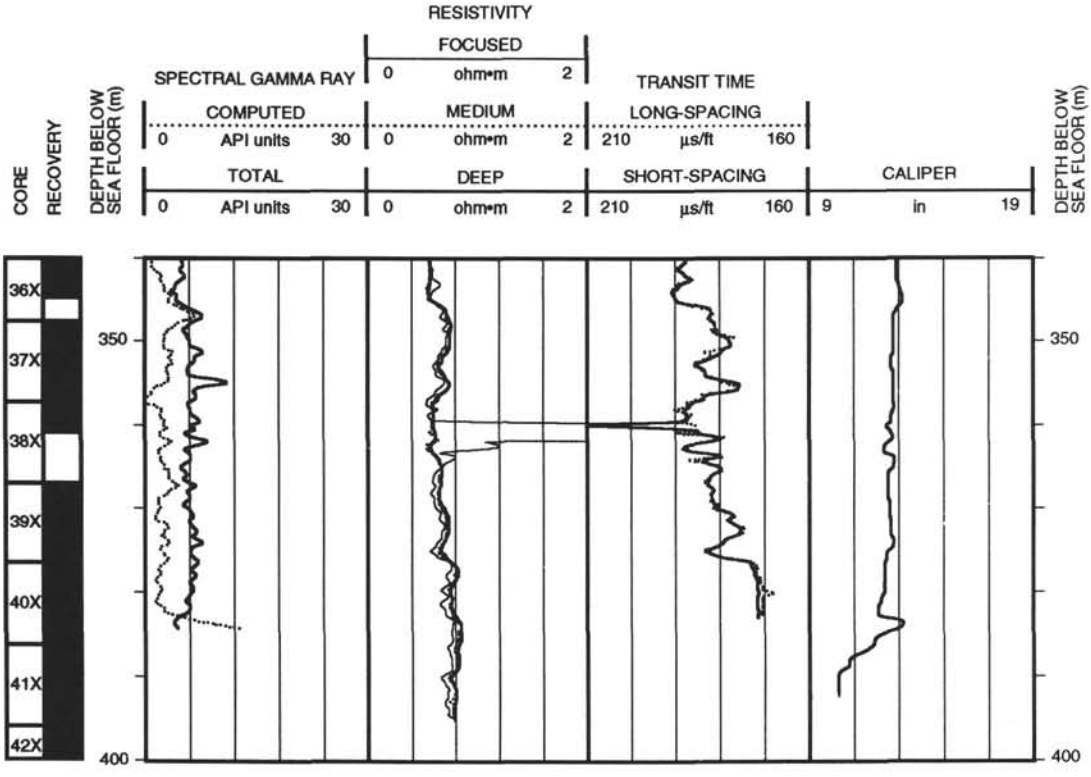

Hole 850B: Density-Natural Gamma Ray Log Summary

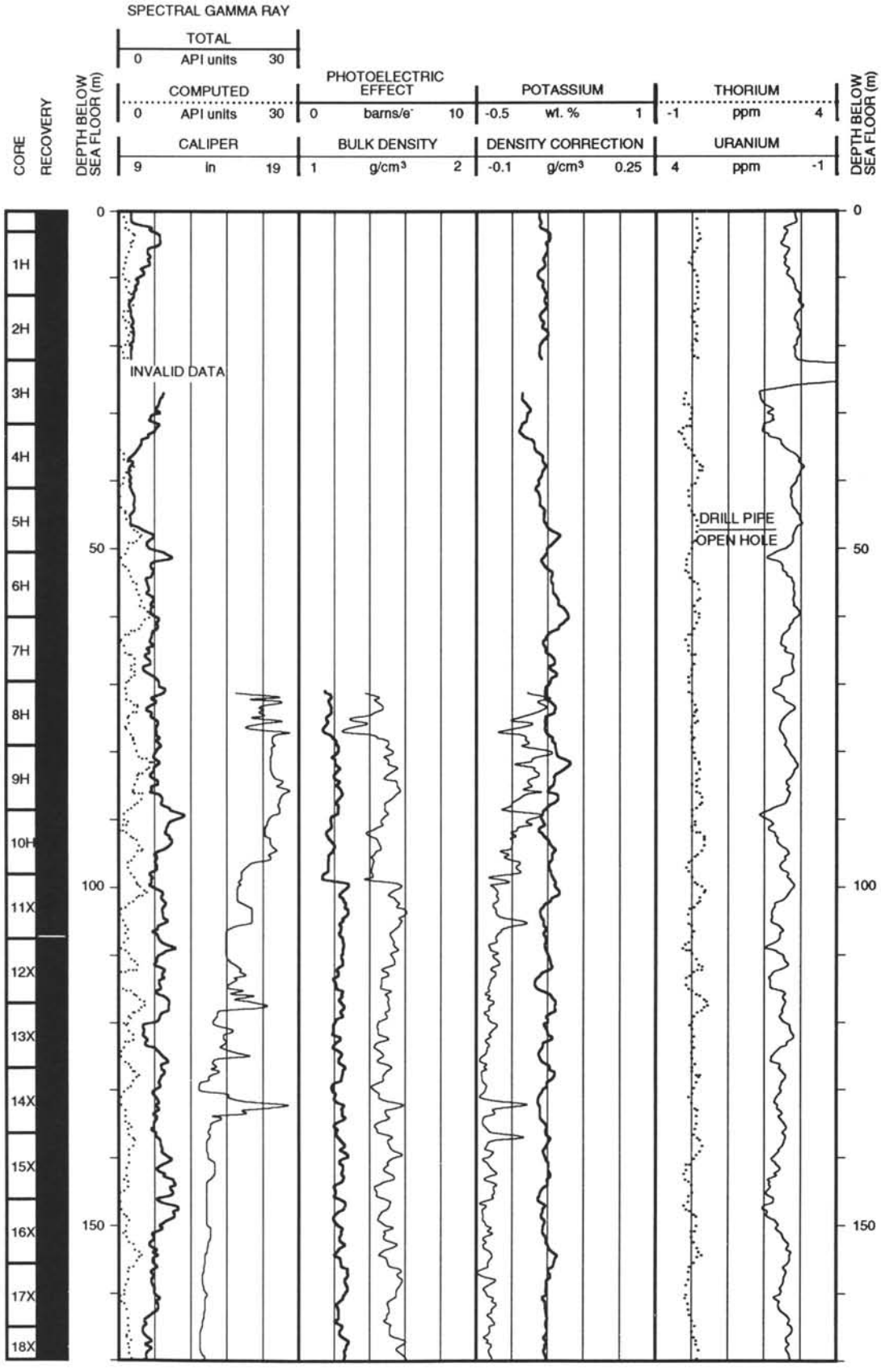

Hole 850B: Density-Natural Gamma Ray Log Summary (continued)

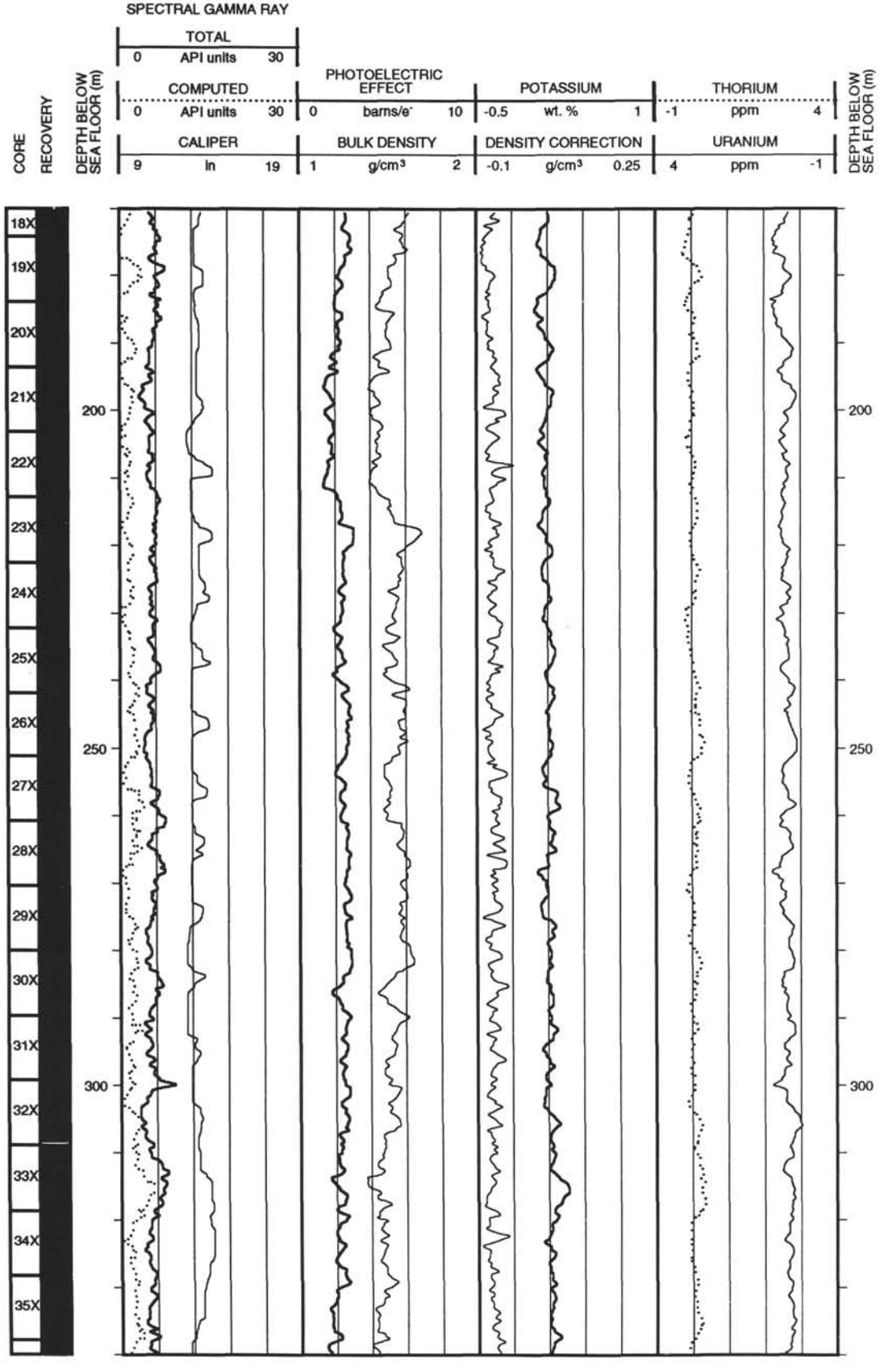

Hole 850B: Density-Natural Gamma Ray Log Summary (continued)

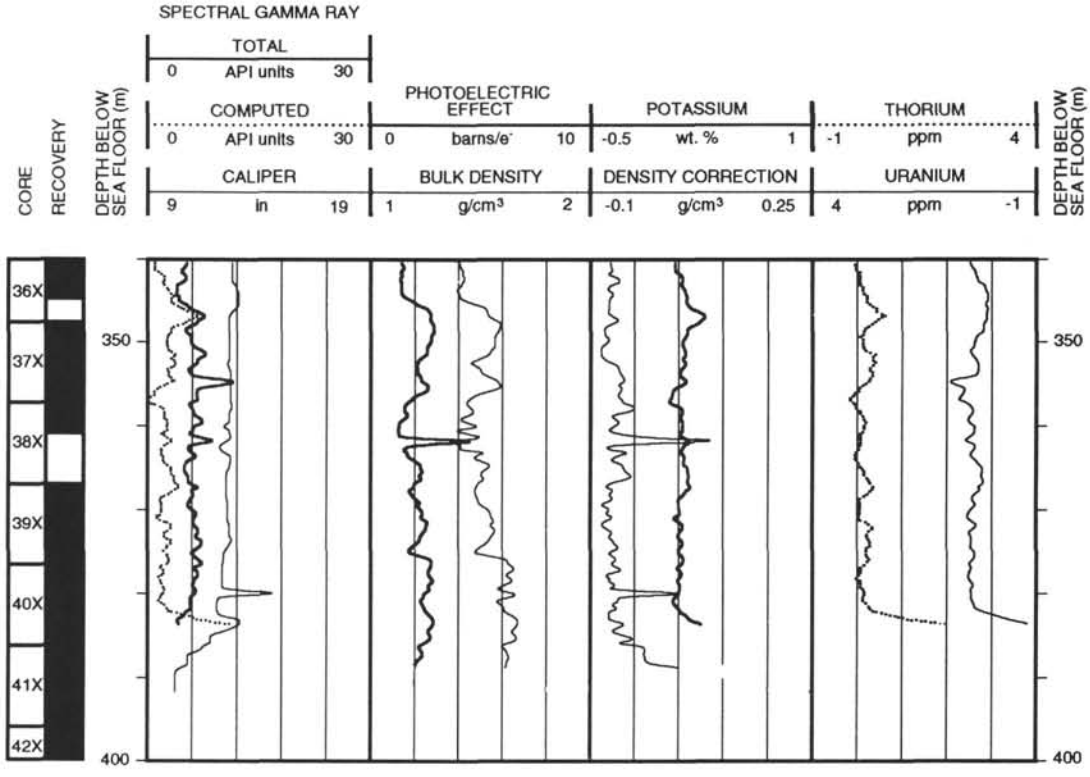

Hole 850B: Geochemical Log Summary

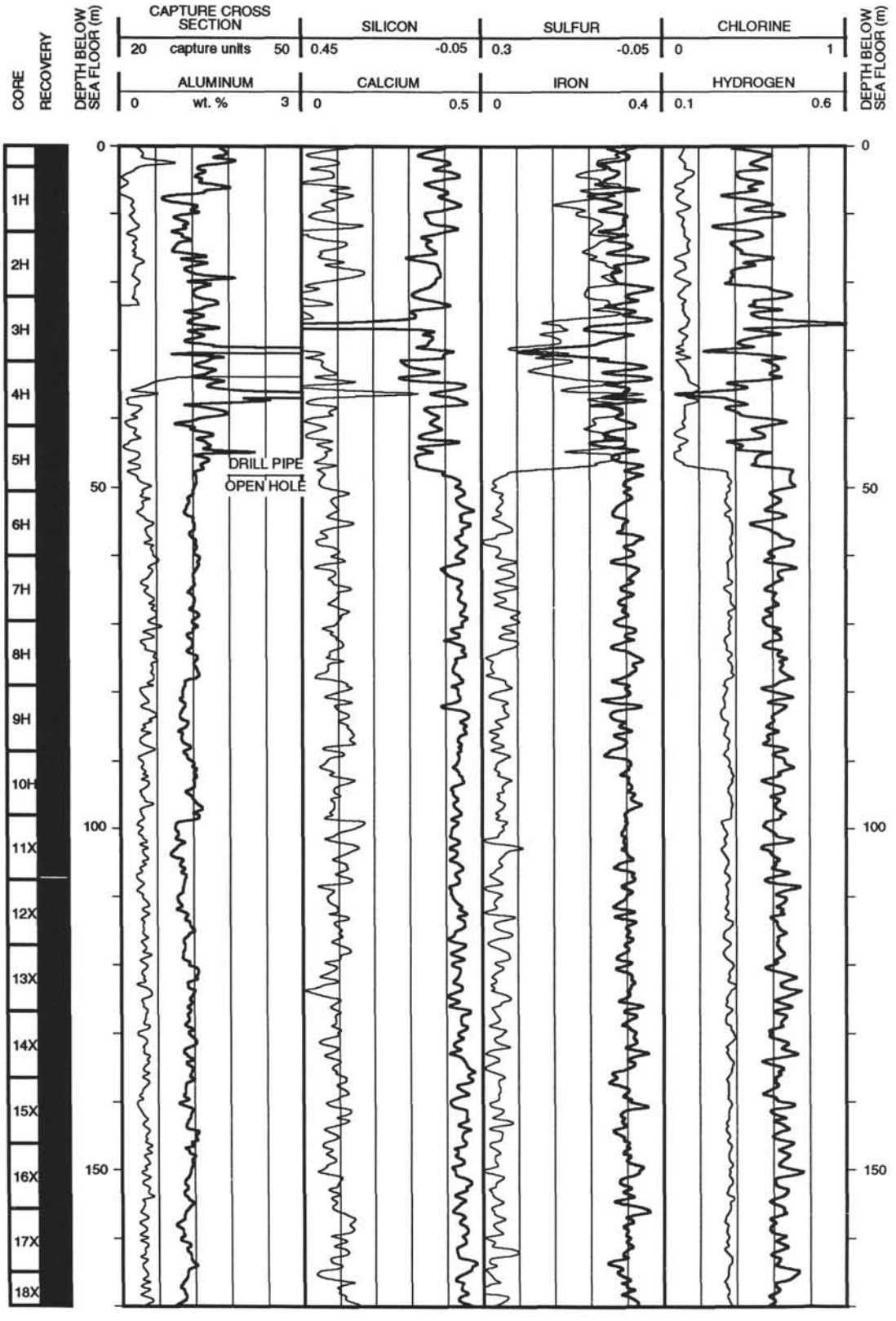

Hole 850B: Geochemical Log Summary (continued)

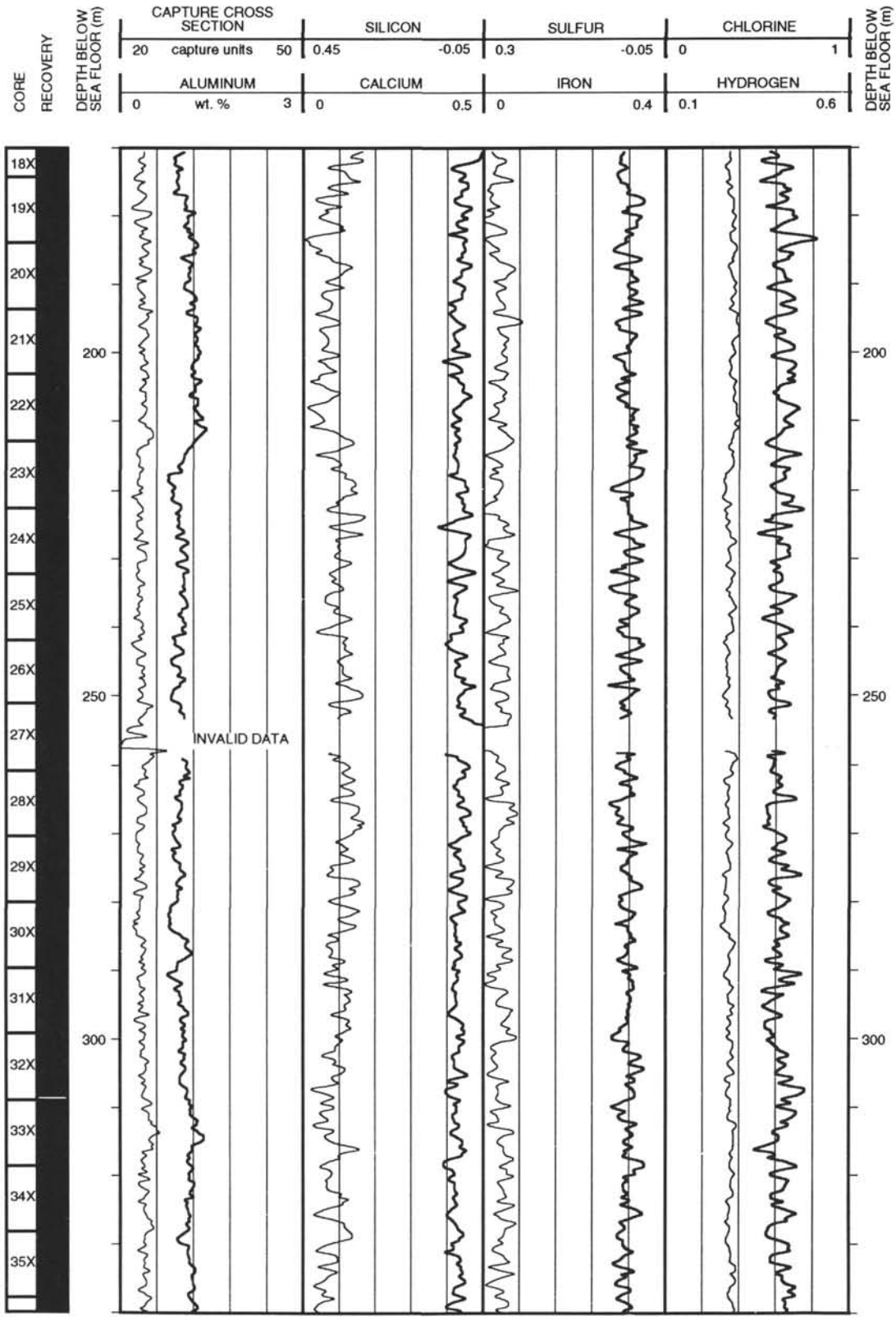

Hole 850B: Geochemical Log Summary (continued)